UNIVERSIDADE ESTADUAL DE GOIÁS

CAMPUS ANÁPOLIS DE CIÊNCIAS EXATAS E TECNOLÓGICAS

PROGRAMA DE PÓS-GRADUAÇÃO *STRICTO SENSU* EM CIÊNCIAS MOLECULARES

MARIANNA CARRILHO SILVA

ANÁLISE ESTRUTURAL E TOPOLÓGICA DOS FLAVONÓIDES EPICATEQUINA E CHALCONA TERPENÓIDE

Anápolis-GO

2021

MARIANNA CARRILHO SILVA

ANÁLISE ESTRUTURAL E TOPOLÓGICA DOS FLAVONÓIDES EPICATEQUINA E CHALCONA TERPENÓIDE

Dissertação apresentada ao programa de Pós-Graduação *Stricto Sensu* em Ciências Moleculares, da Universidade Estadual de Goiás, para obtenção do título de mestre em Ciências Moleculares.

Área: Físico-Química.

Orientador: Prof. Dr. Hamilton Barbosa Napolitano.

Anápolis-GO

2021

TERMO DE AUTORIZAÇÃO PARA PUBLICAÇÃO DE TESES E DISSERTAÇÕES NA BIBLIOTECA DIGITAL (BDTD)

Na qualidade de titular dos direitos de autor, autorizo a Universidade Estadual de Goiás a disponibilizar, gratuitamente, por meio da Biblioteca Digital de Teses e Dissertações (BDTD/UEG), regulamentada pela Resolução, **CsA n.1087/2019** sem ressarcimento dos direitos autorais, de acordo com a Lei nº 9610/98, o documento conforme permissões assinaladas abaixo, para fins de leitura, impressão e/ou *download*, a título de divulgação da produção científica brasileira, a partir desta data.

Dados do autor (a)

Nome Completo: Marianna Carrilho Silva

E-mail: silva.c.marianna@gmail.com

Dados do trabalho

Título: Análise estrutural e topológica dos flavonóides epicatequina e chalcona terpenóide

Data da Defesa 01/03/2021

Tipo

( ) Tese (X) Dissertação

Programa de Mestrado em Ciências Moleculares

Concorda com a liberação documento

[X] SIM

[ ] NÃO **Casos de impedimento:** Período de embargo por até um ano a partir da data de defesa. A extensão deste prazo necessita de justificativa junto à coordenação do curso.

- [ ] Solicitação de registro de patente;
- [ ] Submissão de artigo em revista científica;
- [ ] Publicação como capítulo de livro;
- [ ] Publicação da dissertação/tese em livro.

Anápolis, 11/março/2021
Local Data

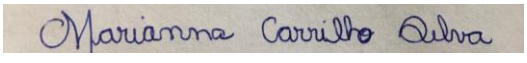

Assinatura do autor (a)

Assinatura do orientador (a)

Elaborada pelo Sistema de Geração Automática de Ficha Catalográfica da UEG
com os dados fornecidos pelo(a) autor(a).

CSI58 Carrilho Silva , Marianna
6a ANÁLISE ESTRUTURAL E TOPOLÓGICA DOS FLAVONÓIDES EPICATEQUINA E CHALCONA TERPENÓIDE / Marianna Carrilho Silva ; orientador Hamilton Barbosa Napolitano. -- Anápolis, 2021.
51 p.

Dissertação (Mestrado - Programa de Pós-Graduação Mestrado Acadêmico em Ciências Moleculares) -- Câmpus Central - Sede: Anápolis - CET, Universidade Estadual de Goiás, 2021.

1. flavonóides. 2. cristalografia. 3. análises topológicas . I. Barbosa Napolitano, Hamilton, orient. II. Título.

ANÁLISE ESTRUTURAL E TOPOLÓGICA DOS FLAVONÓIDES EPICATEQUINA E CHALCONA TERPENÓIDE

MARIANNA CARRILHO SILVA

Dissertação apresentada ao Programa de Mestrado em Ciências Moleculares do Campus Anápolis de Ciências Exatas e Tecnológicas Henrique Santillo, da Universidade Estadual de Goiás, apresentada como parte dos requisitos necessários para obtenção do título de Mestre em Ciências Moleculares.

Aprovada em 1°/03/2021 por:

_____

Prof. Dr. Hamilton Barbosa Napolitano (Orientador/UEG)

_____

Prof. Dr. Antônio Carlos Severo Menezes (UEG)

_____

Profa. Dra. Samantha Salomão Caramori (UEG)

ANÁPOLIS – GO

AGRADECIMENTOS

Inicialmente a Deus, por me guiar durante todo o caminho me concedendo sabedoria para tal tarefa.

Aos meus pais Silma Ferreira Silva e Eurides Antônio da Silva, minha eterna gratidão pelo apoio, carinho, e por sempre acreditar no meu melhor.

Ao meu orientador Prof. Dr. Hamilton Barbosa Napolitano, pelo incentivo e confiança, contribuindo amplamente para minha formação profissional e pessoal. Pela paciência, humildade e conhecimentos transmitidos, que sempre estarão em minha memória.

Ao meu namorado João Marcos Melo Beiriz por toda ajuda, apoio e encorajamento nos momentos de dificuldade.

À *International Union of Crystallography* (IUCr) pelo apoio concedido para a participação da *ACA Summer Course in Chemical Crystallography*, *Northwestern University* (EUA), e também ao Prof. Dr. Allen Grayson Oliver que me recebeu em seu laboratório na *University of Notre Dame* (EUA).

Aos meus colegas do laboratório de Química Teórica e Estrutural de Anápolis (QTEA), por toda ajuda acadêmica, bem como a todos os coautores dos artigos publicados durante esse período.

À Universidade Estadual de Goiás e ao Programa de Pós-Graduação em Ciências Moleculares, pela oportunidade oferecida.

À coordenação de Aperfeiçoamento de Pessoal e Nível Superior (CAPES), pelo suporte financeiro por meio da bolsa de estudos, possibilitando a realização deste trabalho.

RESUMO

A classe geral dos flavonóides vem sendo alvo de diversos estudos devido as suas ações farmacológicas, como anti-inflamatórias, anti-carcinogênicas, antiviral, antifúngica, bactericida, antimicrobiana e antioxidante, sendo utilizados também para tratamentos de doenças cardiovasculares, alergias, entre outras. Essas propriedades podem ser relacionadas pelas características estruturais de cada composto, como grupos funcionais, tipo de interações etc., demonstrando assim a importância da compreensão estrutural para a análise da relação estrutura-atividade. Partindo dessa premissa foram elucidados através da Difração de raios-X os flavonóides, epicatequina e chalcona terpenóide (o primeiro extraído da planta *Salacia crassifolia* e o segundo obtido através da síntese de condensação de Claisen-Schmidt), obtendo-se parâmetros geométricos, análises topológicas e cálculos teóricos com base na mecânica quântica. Desta maneira essa dissertação se torna importante devido a toda elucidação estrutural apresentada, permitindo estudos futuros como, a análise de relações estrutura-atividade dos compostos apresentados nesta dissertação, e de futuras estruturas homólogas obtidas através de sínteses.

Palavras-chave: *flavonóides, cristalografia, análise topológica*.

ABSTRACT

The general class of flavonoids has been the target of several studies due to their pharmacological actions, such as anti-inflammatory, anti-carcinogenic, antiviral, antifungal, antibacterial, antimicrobial and antioxidant, being used also for treatments of cardiovascular diseases, allergies, among others. These properties can be related to the structural characteristics of each compound, such as functional groups, type of interactions, etc., thus demonstrating the importance of structural understanding for the analysis of the Structure-Activity relationship. Based on this premise the flavonoids, epicatechin, and terpenoid-like chalcona (the first extracted from the *Salacia crassifolia* plant and the second obtained through the Claisen-Schmidt synthesis) were elucidated through X-ray diffraction, obtaining geometric parameters, topological analyzes, and theoretical calculations based on quantum mechanics. In this way, this dissertation becomes important due to all the structural elucidation presented, allowing future studies such as the analysis of Structure-Activity relationships of the compounds presented in this dissertation, and of future homologous structures obtained through syntheses.

Keywords: flavonoids, crystallography, topological analysis.

LISTA DE FIGURAS

LISTA DE TABELA

SUMÁRIO

1 INTRODUÇÃO

A elucidação estrutural de compostos possui um importante papel no trabalho científico, pois permite entender suas propriedades e a aplicabilidade de forma interdisciplinar, nas áreas da biologia molecular, química, física, farmacologia, geologia, ciências dos materiais, entre outras (KOVALCHUK, 2011; AITIPAMULA; VANGALA, 2017; BROOKS-BARTLETT; GARMAN, 2015). Dentre as diversas metodologias utilizadas para o conhecimento do arranjo estrutural, a difração de raios-X é a mais adequada, devido à alta resolução que permite descrever a densidade eletrônica mediante a obtenção indireta da correspondente imagem (WATKIN, 2010).

Desta maneira, a necessidade de moléculas com ações potencializadas de aplicação pode ser suprida a partir do seu conhecimento estrutural, através da cristalografia, como no caso dos flavonóides, que tem sido alvo de extensivos estudos devido as suas expressivas ações farmacológicas (WANG; LI; BI, 2018), tais como anti-inflamatórias, anti-carcinogênicas, antiviral, antifúngica, bactericida, antimicrobiana, antioxidante, sendo utilizados também para tratamentos de doenças cardiovasculares, alergias, entre outras (AGRAWAL, 2011; HARBORNE; WILLIAMS, 2000; HAVSTEEN, 1983; HAVSTEEN, 2002). Essas propriedades podem ser explicadas pela relação estrutura-atividade, como grau de co-planaridade, presença de diferentes grupos funcionais (que devem ter sua disposição tridimensional favorecendo uma maior complementariedade ao sítio de ligação biológico), tipo de interações (uma vez que as propriedades estão diretamente relacionadas as forças intermoleculares), etc. (ARROIO; HONÓRIO; SILVA, 2010). Um exemplo de flavonoide que tem sua atividade bactericida potencializada pela influência de um grupo funcional é a chalcona, quando existe um grupo hidroxila C-4, um substituinte oxigenado C-4’, ou uma cadeia lateral isoprenóide C-3’ (Figura 1b) (SARBU et al., 2019). Os flavonoides podem ser obtidos por extração vegetal, variando a composição de acordo com a disponibilidade de água, nutrientes e idade da planta, intensidade

de luz solar e tipo de solo (GÓRNIAK; BARTOSZEWSKI; KRÓLICZEWSKI, 2018), e também por meio de várias rotas sintéticas, sendo a mais simples a condensação de 2’-hidroxiacetofenonas em condições ácidas ou básicas. (SARBU et al., 2019).

A estrutura básica do flavonoide é constituída por dois anéis benzílicos, unidos por uma ponte de três carbonos que pode ou não ser fechada em um anel pirano (SHARMA; TULI; SHARMA, 2019), eles podem ser divididos partindo do anel C como referência, onde as isoflavonas têm o anel B ligado na posição 3, os neoflavonóides têm o anel B ligados na posição 4, enquanto os flavanos têm o anel B ligado na posição 2, como demonstrado na Figura 1a. Os flavanos podem ser subdivididos através de características estruturais do anel C, sendo eles, flavona, flavonol, flavonona, flavononóis, catequinas, antocianinas e chalconas, representados na Figura 1b (PANCHE; DIWAN; CHANDRA, 2016).

Figura 1.(a) Fórmula estrutural das classes flavonoides **(b)** Subclasse dos Flavanos.

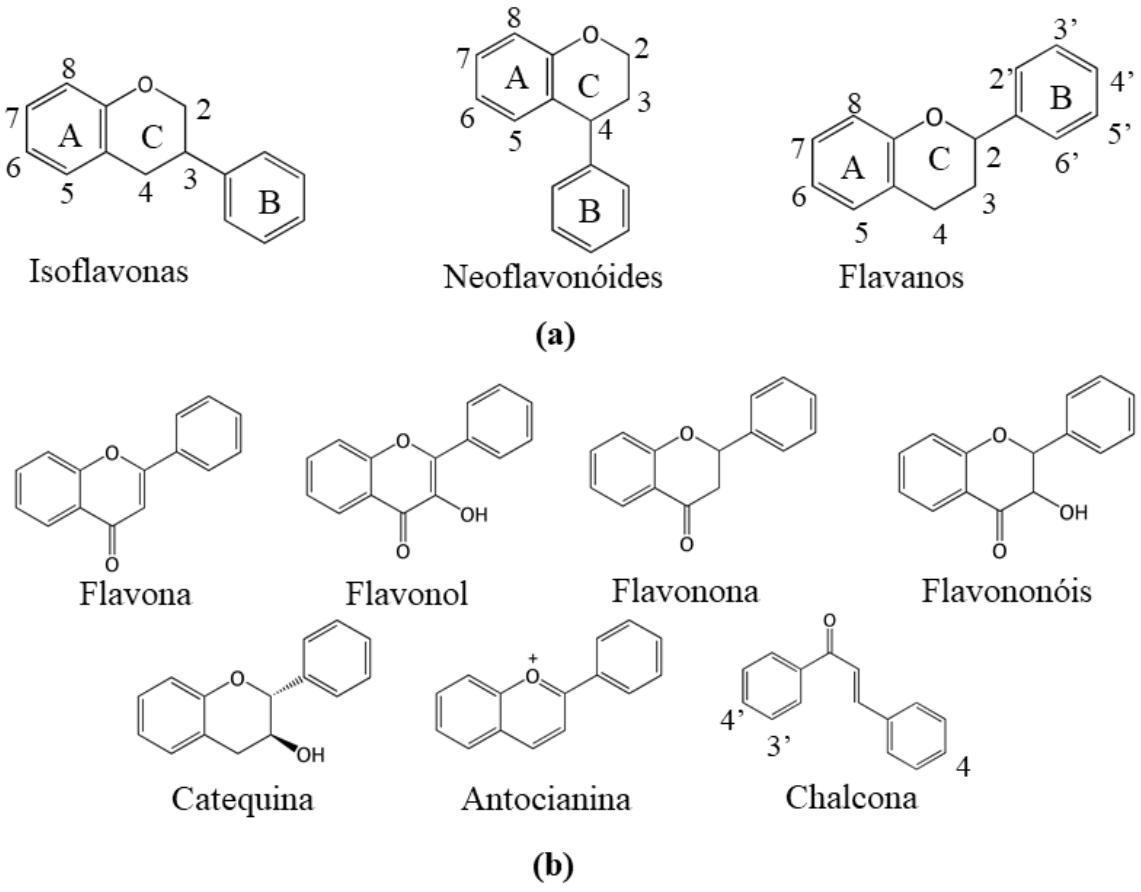

A epicatequina é um composto polifenólico pertencente a classe dos flavanos, sua estrutura básica é constituída de dois anéis aromáticos (A e B), ligados por uma cadeia de três carbonos, formando um heterocíclico oxigenado (anel C). Suas fontes naturais são amplamente comuns em sementes de uva, maçã, grãos de cacau, entre outros (FRAGA; OTEIZA; GALLEANO, 2018; BABA et al., 2002). A epicatequina possui resultados promissores contra doenças cardiovasculares (PRAKASH; BASAVARAJ; MURTHY, 2019; FRAGA; OTEIZA; GALLEANO, 2018; DOWER et al., 2015; SCHROETER et al., 2006), neurodegenerativas (Alzheimer) (SCHROETER et al., 2007; STRINGER et al., 2015) e neurológicas (ansiedade) (STRINGER et al., 2015), além disso apresenta propriedade antitumoral, anti-inflamatória, antimicrobiana (PRAKASH; BASAVARAJ; MURTHY, 2019), antioxidante (FRAGA; OTEIZA; GALLEANO, 2018; ENGLER et al., 2013) e bactericida (XIA et al., 2010). As chalconas são bioprecursoras dos flavonóides e isoflavonóides, seu núcleo é constituído de um sistema carbonílico α-β insaturado que une dois anéis aromáticos (RAMMOHAN et al., 2020). Apresentam considerável interesse devido a sua estrutura relativamente simples, e suas atividades biológicas como, anti-inflamatória (FUNAKOSHI-TAGO et al., 2015; HIRAI et al., 2007; NOWAKOWSKA, 2007), antioxidante (CIOFFI et al., 2003; DOAN; TRAN, 2011), anti-leishmania (HERMOSO et al., 2003; RASHID et al., 2016), antitubercular (GUANTAI et al., 2011), anticâncer (WU et al., 2013; BHALE et al., 2017; COSKUN et al., 2017), anti-HIV (RAMMOHAN et al., 2020; GAONKAR; VIGNESH, 2017), bactericida (GO; WU; LIU, 2005), antimalárica, antituberculose, antiúlcera, antidiabética e antiprotozoária (ROZMER; PERJÉSI, 2016; RAMMOHAN et al., 2020; GAONKAR; VIGNESH, 2017).

Considerando tal contexto a presente dissertação aborda a análise estrutural dos flavonóides, epicatequina e chalcona terpenóide, o primeiro extraído da planta *Salacia crassifolia* (Celastraceae), e o segundo obtido sinteticamente pela condensação de Claisen-Schmidt em meio básico. O trabalho teve como objetivo

a análise estrutural de ambos compostos, bem como as interações moleculares através da topologia, e adicionalmente as propriedades dos átomos ou regiões específicas de cada molécula através de cálculos teóricos baseados na mecânica quântica, proporcionando assim futuros estudos de relação estrutura-atividade destes flavonóides e análogos sintéticos.

2 TÓPICOS EM CRISTALOGRAFIA

O estado sólido é encontrado na natureza em duas disposições: amorfa e cristalina. Para o estado amorfo não existe um arranjo interno ordenado dos átomos (STOCK et al., 2001; BORCHARDT-OTT, 2011), enquanto o estado cristalino da matéria apresenta um padrão regular e periódico da disposição dos átomos e moléculas (ATINKS; JONES, 2012). A elucidação estrutural de um composto é resultado da interação da radiação com sua matéria constituinte, sendo a resposta dessa interação dependente da distribuição espacial dos elétrons presentes. Assim, para entender como isso é possível, serão apresentados os conceitos de simetria cristalográfica, difração de raios-X, densidade eletrônica, problema da fase, e superfície de Hirshfeld.

2.1 Simetria cristalográfica

O entendimento da existência da regularidade e periodicidade da natureza dos cristais se dá pela simetria, que pode ser dividida em: translacional e pontual. A simetria translacional se dá ao fato das moléculas estarem em um padrão periódico de comprimento, área e volume no espaço por translação, o que possibilita o fenômeno da difração de raios-X, em contraponto a simetria pontual descreve como a unidade assimétrica se acomoda na cela unitária. A simetria translacional ocorre para a totalidade do cristal, podendo definir o mesmo como uma repetição tridimensional por translação da cela unitária, que é a menor unidade de volume do cristal, a qual carrega todas informações contidas na estrutura cristalina. A cela unitária tem sua forma determinada por seis

parâmetros: três vetores não coplanares, denominados eixos cristalográficos (a, b, c), que são escolhidos de modo que quando sequenciados formam um sistema axial que segue a regra da mão direita, e três angulares (α, β, γ). Os ângulos formados entre os vetores axiais são designados por α (entre b e c), β (entre a e c) e γ (entre a e b) (STOUT; JENSEN, 1989; GLUSKER; TRUEBLOOD, 2010; TILLEY, 2014). Da comutação desses parâmetros advém os sete sistemas cristalinos[1], conforme indica a Tabela 1.

Tabela 1. Sete sistemas cristalinos com seus parâmetros de cela

Sistema cristalino	**Valores axiais**	**Valores angulares**
Triclínico	$a \neq b \neq c$	$\alpha \neq \beta \neq \gamma \neq 90°$
Monoclínico	$a \neq b \neq c$	$\alpha = \gamma = 90° \neq \beta$
Ortorrômbico	$a \neq b \neq c$	$\alpha = \beta = \gamma = 90°$
Trigonal (ou romboédrico)	$a = b = c$	$\alpha = \beta = \gamma \neq 90°$
Tetragonal	$a = b \neq c$	$\alpha = \beta = \gamma = 90°$
Hexagonal	$a = b \neq c$	$\alpha = \beta = 90°, \gamma = 120°$
Cúbico	$a = b = c$	$\alpha = \beta = \gamma = 90°$

A repetição periódica e tridimensional da cela unitária é definida como rede cristalina, e é representada por um padrão infinito de pontos em que cada ponto tem as mesmas vizinhanças e a mesma orientação, sendo, portanto, uma construção matemática de magnitudes *u*, *v*, *w* nas direções dos vetores $\vec{a}$, $\vec{b}$ e $\vec{c}$, como demonstrado na Equação 1.

$$L(\vec{r}) = \sum \delta[\vec{r} - (u\vec{a} + v\vec{b} + w\vec{c})] \qquad \text{Equação 1}$$

[1] Os sete sistemas cristalinos são demonstrados em relação a sua métrica na Figura 2, onde estão representadas as redes de Bravais.

Onde, δ é a função delta de Dirac[2] e L($\vec{r}$) é a rede de difração (CLEGG et al., 2009; GIACOVAZZO et al., 2011). Desse modo existem apenas cinco retículos cristalinos bidimensionais e 14 retículos tridimensionais, que são as redes de Bravais (TILLEY, 2014). As redes de Bravais podem ser classificadas em celas primitivas e não primitivas, as primitivas possuem pontos somente nos vértices, e pode ser representada por P para todos os sistemas cristalinos, exceto para o trigonal o qual se usa especialmente R. As celas não primitivas possuem pontos adicionais no interior ou nas faces, e são representadas pelos símbolos A, B e C, que caracterizam centragem nas faces A, B ou C, respectivamente, enquanto o símbolo F designa a rede em que todas as faces são centradas, e o símbolo I identifica a rede de corpo centrado(BORCHARDT-OTT, 2011).

Figura 2. Representação das 14 Redes de Bravais

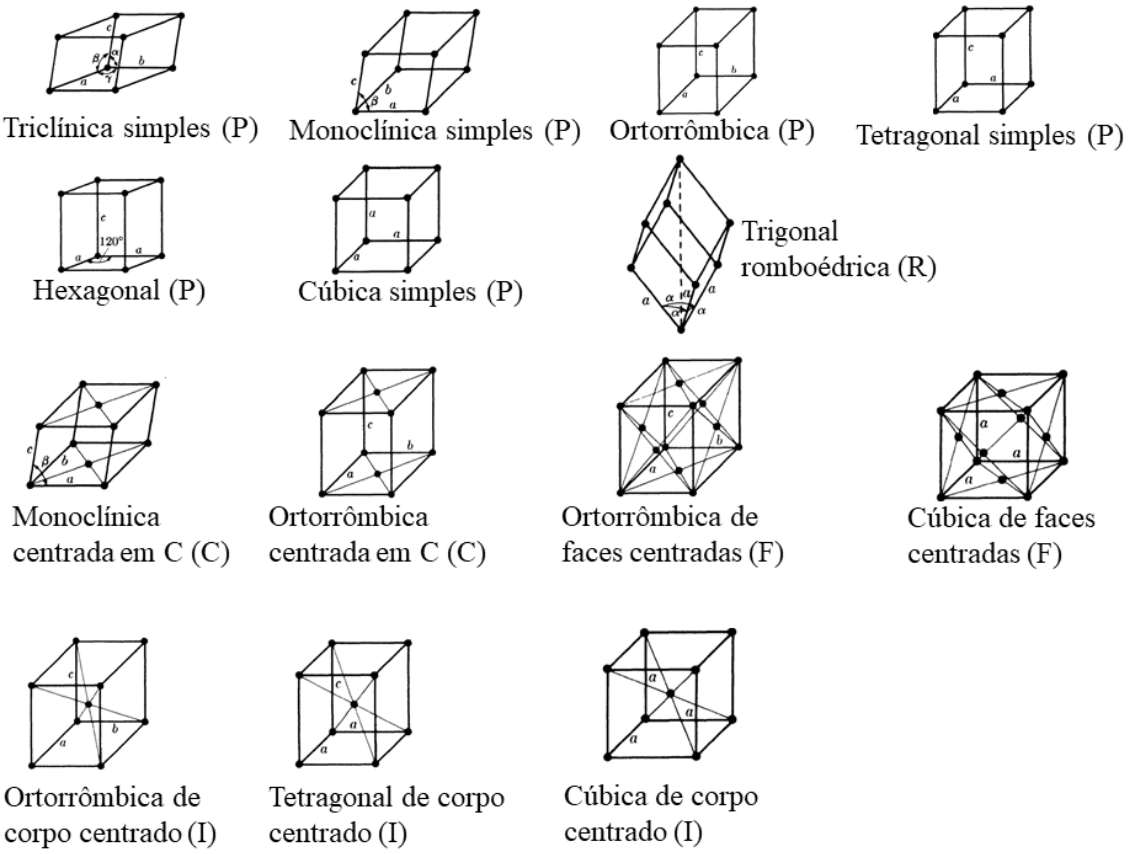

[2] A função delta de Dirac ou função δ é um funcional (ou distribuição) na reta real, sendo infinita no ponto zero e nula no restante dessa reta.

A simetria pontual é aquela que tem seu estudo fundamentado no interior da cela unitária, por operações matemáticas, as quais são conhecidas como operações de simetria, e podem ser divididas em próprias e impróprias. As operações de simetria próprias são representadas por $360/\theta = n$, onde Θ é o ângulo mínimo de rotação e n é conhecido como ordem do eixo de rotação, podendo ser 1, 2, 3, 4, 6. Eixos de rotação de ordem 5 ou acima de 6 são incapazes de atingir completamente um plano da cela unitária, sendo que essa inexistência pode ser explicada pelo teorema de restrição cristalográfica (CHATTERJEE, 2008). As operações de simetria impróprias são aquelas que provocam a modificação da conectividade da estrutura, ela é constituída pelo centro de inversão (/) e espelhos (m), um corpo tem um centro de inversão se seus pontos correspondentes são localizados a distâncias iguais a partir do centro de uma linha traçada entre tais pontos, tendo assim sua configuração invertida, já o espelho converte o objeto em sua imagem especular (GLUSKER; LEWIS; ROSSI, 1994; STOUT; JENSEN, 1989). É importante destacar que duas operações de simetria geram uma terceira operação de simetria, por exemplo se um objeto apresenta dois eixos de rotação própria, será gerado um eixo de rotação impróprio, se apresenta dois eixos de rotação impróprios, será gerado um eixo de rotação própria, se um eixo de rotação próprio intercepta um eixo de rotação de rotação impróprio, será gerado um eixo de rotação impróprio, formando 32 grupos pontuais (SACZEWSKI et al., 2008). Qualquer simetria no empacotamento de objetos é relacionada a simetria do seu padrão de difração, podendo ser usado para indicar a simetria cristalina, a fim de obtenção do grupo espacial. Sendo assim combinada com a Lei de Friedel[3], que impõe um padrão de difração centrossimétrico a toda estrutura analisada, independente do cristal possuir ou não centro de simetria, dá-se origem aos 11 grupos de Laue, destacados na Tabela 2.

[3] A única exceção encontrada para a Lei de Friedel é se os átomos espalharem a radiação de forma anômala.

Tabela 2. Os 32 grupos pontuais (em destaque os 11 grupos de Laue)

Sistema cristalino	**Valores axiais**
Triclínico	$1;\ \mathbf{\bar{1}}$
Monoclínico	$2;\ m;\ \mathbf{2/m}$
Ortorrômbico	$222;\ mm2;\ \mathbf{mmm}$
Trigonal (ou romboédrico)	$3; \mathbf{\bar{3}}; 32; 3m;\ \mathbf{\bar{3}m}$
Tetragonal	$4;\ \bar{4};\ \mathbf{4/m};\ 422;\ 4mm;\ \bar{4}2m;\ \mathbf{4/mmm}$
Hexagonal	$6;\ \bar{6};\ \mathbf{6/m};\ 622;\ 6mm;\ \bar{6}m\bar{2};\ \mathbf{6/mmm}$
Cúbico	$23;\ \mathbf{m\bar{3}};\ 432;\ \bar{4}3m;\ \mathbf{m3m}$

Através da combinação das 14 Redes de Bravais com os 32 grupos pontuais, originam-se os 73 grupos espaciais que quando combinados com os 157 grupos originados pelos eixos helicoidais e planos de deslizamentos, obtém-se os 230 grupos espaciais[4] que toda matéria cristalina pode ser classificada (GIACOVAZZO et al., 2011).

2.2 Difração de raios-X

Os átomos dos cristais se ordenam em planos cristalinos separados entre si por distâncias de ordem equivalente a distância interatômica (0,1 até 100 Å) de comprimento de onda dos raios-X, possibilitando assim a elucidação estrutural sem nenhum conhecimento a *priori*, sendo necessário apenas que o feixe de raios-X (colimado e monocromático) para incidir na amostra cristalina (ALBERS et al., 2002). Ao interagir com a matéria o raio-X produz três fenômenos: absorção,

[4] A representação de todos os 230 grupos espaciais pode ser encontrada na *International Tables of Crystallography* Volume A.

emissão e espalhamento. A absorção ocorre quando um elétron interage com o campo elétrico absorvendo o fóton, passando do estado fundamental para o estado de maior energia. A emissão ocorre quando o elétron está em um estado ativado e volta para um estado de menor energia, ou seu estado fundamental. O espalhamento é a radiação emitida pelas cargas aceleradas, provindas dos raios-X incidentes, que quando combinado com o fenômeno de interferência origina-se um fenômeno secundário chamado difração.

O fenômeno de interferência gera maiores deslocamentos nos pontos em que os máximos e mínimos coincidem, assim as regiões de interferência construtiva ou destrutiva exibem alternadamente, intensidades reforçadas ou reduzidas, respectivamente (SACZEWSKI et al., 2008). A cristalografia se restringe apenas ao espalhamento construtivo, também chamado de espalhamento coerente, que segundo Thomson, se caracteriza com a deflexão dos fótons na amostra, sem perdas de energia, sendo assim o comprimento de radiação incidente e espalhada possuem o mesmo valor (GIACOVAZZO et al., 2011).

Desta maneira o cristal em que a radiação incidente é espalhada é chamada espaço direto e é definido pelo vetor $\vec{r} = x\vec{a} + y\vec{b} + z\vec{c}$, sendo o espaço direto constituído pela rede cristalina e os eixos cristalográficos a, b, e c, produzindo consequentemente um feixe espalhado no espaço recíproco com a localização fornecida pelo vetor $\vec{S} = h\overrightarrow{a^*} + k\overrightarrow{b^*} + l\overrightarrow{c^*}$, desta maneira os feixes de Bragg difratados podem ser descritos no espaço recíproco, sendo constituídos pelos eixos *a**, *b** e *c**, onde *h, k, l* são índices de *Miller* (STOUT; JENSEN, 1989; STOCK et al., 2001). Estabelecendo dois espalhamentos 1 e 2 distantes um do outro pelo vetor $\vec{r}$, e considerando um raio-X com comprimento de onda λ, a interferência construtiva entre ondas dispersas por 1 e 2, será observada apenas se estiverem em fases, como demonstrado na Figura 3. A diferença de caminho óptico é definida por $\vec{r}.\vec{S}$, onde $\vec{S} = (\vec{s} - \overrightarrow{s_o})/\lambda$ onde, $\overrightarrow{s_o}$ representa o feixe

incidido e $\vec{s}$ o feixe difratado, sendo $|\overrightarrow{s_o}| = |\vec{s}| = 1/\lambda$. A diferença de fase das duas ondas é dada por $\theta = 2\pi\vec{S}.\vec{r}$.

Figura 3. Representação da condição de difração para dois planos distantes, como proposto por Bragg. As ondas espalhadas são representadas pelos números 1 e 2.

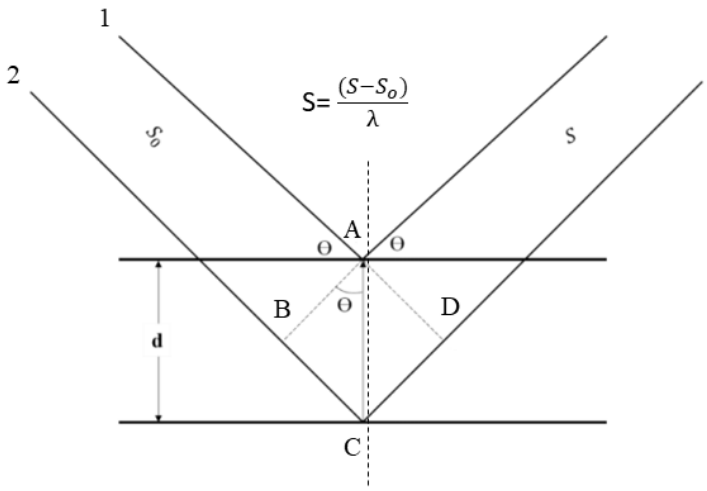

Para a análise do espalhamento atômico é necessária uma relação trigonométrica, em que a diferença de caminho percorrido entre os planos é $\overline{BC} + \overline{CD} = \delta$, em seguida relacionando os triângulos ABC e ACD, temos a Equação 2.

$$\sin\theta = \frac{\overline{BC}}{d_{(hkl)}} = \frac{\overline{CD}}{d_{(hkl)}} \qquad \text{Equação 2}$$

Reescrevendo a diferença de caminho óptico temos $\delta = 2d_{(hkl)}\sin\theta$, a condição para que a diferença de caminho óptico seja construtiva, é o comprimento de onda de um feixe incidente seja um múltiplo inteiro, sobre essas condições obtém-se a Lei de Bragg (BRAGG; BRAGG, 1913) que é representada na Equação 3.

$$2d_{(hkl)}\sin\theta = n\lambda \qquad \text{Equação 3}$$

Como a densidade eletrônica na cela unitária de um cristal não está distribuída em planos, mas sim tridimensionalmente por toda a cela, a lei de Bragg não retrata a realidade dentro do cristal. Entretanto sua contribuição para o desenvolvimento da ideia de espaço recíproco e para a elucidação de raios-X não pode ser ignorada.

2.3 Densidade eletrônica e o problema da fase

A caracterização estrutural do trabalho cristalográfico parte da construção da densidade eletrônica dos átomos a partir da amplitude e das fases e do fator de estrutura conhecido como $F(hkl)$, esse fator pode ser descrito em termos da somatória das contribuições individuais do espalhamento atômico f, que influencia sua função f_j (WOOLFSON, 1997), o espalhamento do átomo em relação a origem da cela unitária, é dado pela Equação 4.

$$f_j = f_j \,.\, e^{2\pi r j.s} \qquad \text{Equação 4}$$

O fator de estrutura é constituído pela contribuição do espalhamento atômico[5] para todas as direções hkl, conforme demonstra a Equação 5, onde f_j descreve o espalhamento atômico e x_j, y_j, z_j , representam as coordenadas fracionárias do átomo j na cela unitária.

$$F_{(hkl)} = \sum_{j=1}^{n} f_j \, e^{(2\pi i h x_j + 2\pi i h y_j + 2\pi i h z_j)} \qquad \text{Equação 5}$$

Essa operação matemática é de extrema importância dentro da cristalografia, pois relaciona a imagem de difração coletada com a posição dos

[5] Probabilidade de encontrarmos os elétrons de um determinado átomo em um determinado volume pode ser relacionado com a densidade eletrônica, dado por: $\rho_a = |\psi_j|^2$, cuja transformada de Fourier é chamado de fator de espalhamento atômico.

átomos dentro da estrutura cristalina. Aplicando a transformada de Fourier, que é a transformada integral onde qualquer função pode ser expandida em uma série harmônica de base de senoidal e cossenoidal, permite a relação da imagem de difração coletada com a posição de cada átomo presente na estrutura. A densidade eletrônica pode ser determinada em qualquer ponto xyz da cela unitária através da "transformada de Fourrier inversa", que demonstra a maneira que os átomos estão distribuídos em um volume específico (Equação 6).

$$\rho(r) = \frac{1}{V} \sum_{hkl} |F(hkl)|\, e^{2\pi i[hx+kj+lz+\phi(hkl)]} \qquad \text{Equação 6}$$

Sendo assim através da densidade eletrônica é possível descrever a posição de cada átomo presente na estrutura (WOOLFSON, 1997; GIACOVAZZO et al., 2011). Ao observar a Equação 5 é possível identificar o problema da fase que ocorre durante a síntese de Fourier para a caracterização da densidade eletrônica. Cada comprimento de onda espalhado é apresentado uma amplitude e fase, a amplitude possui uma relação com os fótons que podem ser mensurados, correspondendo a uma intensidade, já as fases dos fatores de estrutura não possuem informações, quando é medido o padrão de difração é fornecido apenas a intensidade (que pode ser transformada em amplitude), surgindo assim o problema da fase ϕ, sendo elas mais importantes que as amplitudes, para a determinação da densidade eletrônica $\rho(r)$ (GIACOVAZZO et al., 2011; USÓN; SHELDRICK, 1999). Surge então métodos estatísticos para a resolução do problema da fase, tendo em destaque os métodos diretos pra resolução de pequenas moléculas, e o método de Patterson para a resolução de moléculas com átomos pesados (PATTERSON, 1934; HAUPRMAN, 1986).

2.4 Superfície de Hirshfeld

A superfície de Hirshfeld é a análise e compreensão das interações intermoleculares realizadas através da distância e curvatura molecular, tem sua base no sistema particionado molecular da densidade eletrônica e uma função peso, a fim de definir o espaço ocupado por uma molécula em um cristal, que é definida na equação 7 (SPACKMAN; JAYATILAKA, 2009).

$$w_a\,(r) = \rho_a^{at}(r) \Big/ \sum_{i\epsilon\, molecula} \rho_i^{at}(r) \qquad \text{Equação 7}$$

onde, $\rho_i^{at}(r)$ são médias das densidades eletrônicas dos vários átomos. As funções de distâncias são definidas por *di* e *de*, sendo que *di* analisa a distância entre os núcleos dos átomos internos até a superfície e *de* analisa a distância de um núcleo externo até a Superfície de Hirshfeld. Assim no mapa de potencial eletrostático, cores quentes representam locais onde as distâncias são menores, e cores frias onde as distâncias são maiores. Consequentemente as regiões vermelhas em *di* demonstram locais em que a molécula de comporta como doadoras de contatos intermoleculares mais fortes, e regiões vermelhas em *de* demonstram locais em que a molécula se comporta como receptora de contatos de intermoleculares de maneira mais eficiente. A combinação de *di* e *de*, gera o mapeamento normalizado *dnorm*, em função do raio de van der Waals (Equação 8), onde nas regiões que apresentam coloração vermelha os contatos são menores que os raios de van der Waals, as regiões de coloração branca apresentam contatos com valores próximos da soma do raio de van der Waals, as regiões com coloração azul representam valores com contatos maiores que a soma do raio de van der Waals (MCKINNON; SPACKMAN; MITCHELL, 2004).

$$d_{norm} = \frac{(di - r_i^{vdw})}{r_i^{vdw}} + \frac{(de - r_e^{vdw})}{r_e^{vdw}} \qquad \text{Equação 8}$$

O mapeamento da forma indexada identifica interações hidrofóbicas do tipo π···π, e C-H··· π, indicadas por regiões vermelhas côncavas acima do anel aromático e regiões azuis de curvatura convexa acima das regiões C-H. O *fingerprint* é a representação bidimensional, em que *di* se encontra na abscissa e *de* na ordenada, com informações quantitativas das interações intermoleculares que contribuem para o empacotamento cristalino (SPACKMAN; MCKINNON, 2002).

3 RESULTADOS

3.1 Caracterização do estado sólido da EPC

A EPC foi obtida por extração e cristalização a partir de diclorometano/metanol, e possui hábito prismático laranja claro, com peso molecular de 290,26 g.mol-1. O composto foi cristalizado em sistema ortorrômbico e grupo espacial não centrosimétrico P212121, com parâmetros celulares a = 6,71050 Å, b = 13,2880 Å, c = 14,2615 Å, α = β = γ = 90° e quatro moléculas independentes por cela unitária (Z = 4) (Figura 4).

Figura 4. Representações ORTEP com 50% de probabilidade, e esquema de numeração atômica para EPC. Os átomos de hidrogênio são representados com raios arbitrários.

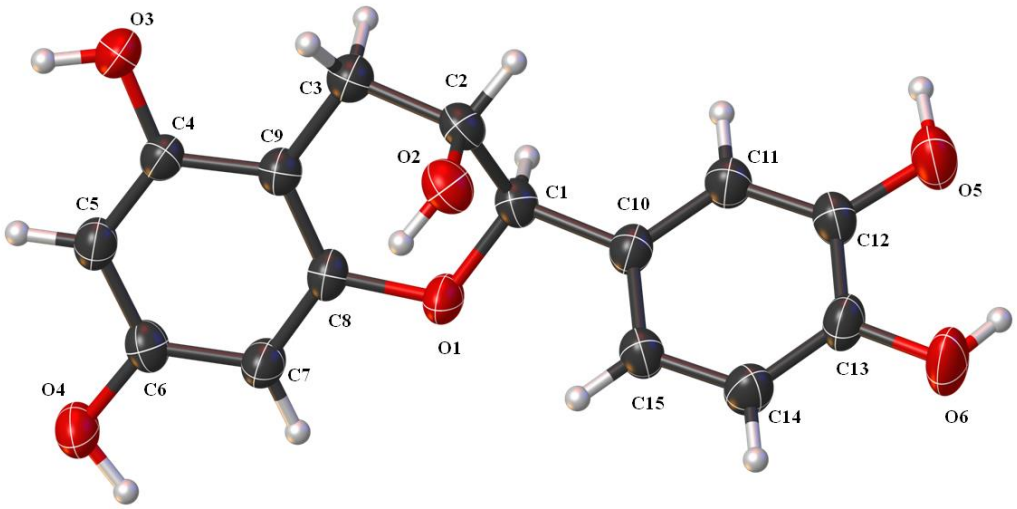

O empacotamento cristalino é estabilizado por interações clássicas tipo O–H…O e não clássicas do tipo C–H…O. As interações e os parâmetros geométricos estão representados na Tabela 3. Um tetrâmero intermolecular envolvendo O6–H6…O4, O4–H4…O3, O3–H3…O2, O2–H2…O6 é observado, crescendo nas direções dos eixos *a* e *b*, que pode ser descrito pelo anel $R_4^4(8)$ (Figura 5a). Outras interações intermoleculares observadas são O5–H5…O1 e C7–H7…O3, que contribuem para um *zigzag* de repetição na direção do eixo *a*, formando uma cadeia infinita em $C_1^1(7)$, e a interação intramolecular que é composta por átomos O6– H6…O5, localizados na direção do eixo *b* (Figura 5b). Além disso, o

composto possui interações intermoleculares bifurcadas C5–H5A…O5 e C3–H3B…O5, na direção do eixo *b* em cadeira infinita, descritas como $C_2^1(7)$, (Figura 5c).

Tabela 3. Distâncias das ligações de hidrogênio (Å) e ângulos (°) para EPC.

D – H···A	D – H	H···A	D···A	D – H···A	Symmetry code
O6–H6···O4	0.84	2.07	2.761	140	x, -1+y, z
O5– H5···O1	1.00	2.25	3.157	151	1/2+x,3/2-y,1-z
O2–H2···O6	0.89	2.01	2.807	149	-x,1/2+y,3/2-z
O3–H3···O2	0.87	1.83	2.694	176	1-x,1/2+y,3/2-z
O4–H4···O3	0.90	2.28	2.963	132	-1+x, y, z
O6–H6···O5	0.84	2.30	2.727	112	x, y, z
C5–H5A···O5	1.01	2.68	3.551	143	x, -1+y, z
C3–H3B···O5	0.98	2.63	3.584	162	1/2 + x,1.5-y,1-z
C7–H7···O3	0.98	2.82	3.291	110	1+x, y, z

Figura 5. Interações intermoleculares e intramoleculares da EPC **(a)** O6–H6…O4, O4–H4…O3, O3–H3…O2 e O2–H2…O6; **(b)** O5–H5…O1, C7–H7…O3 e O6–H6…O5; **(c)** C5–H5A…O5 e C3–H3B…O5.

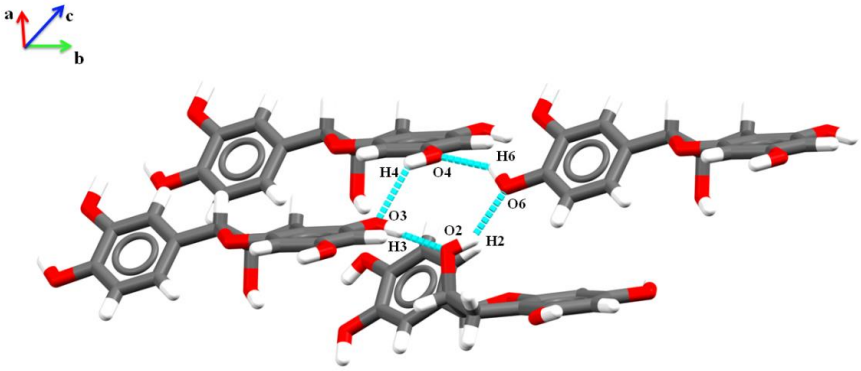

(a)

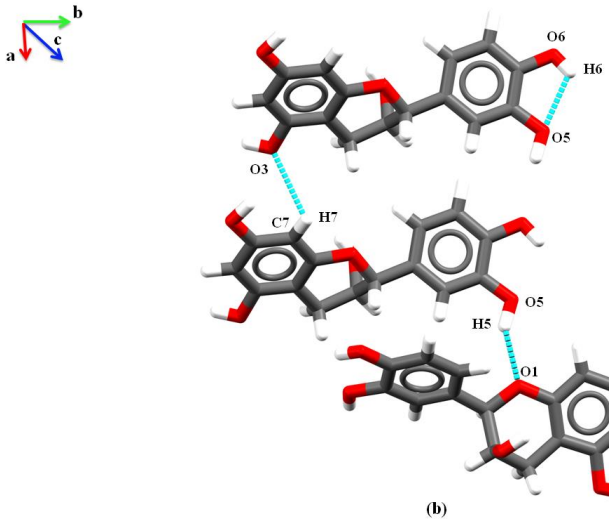

(b)

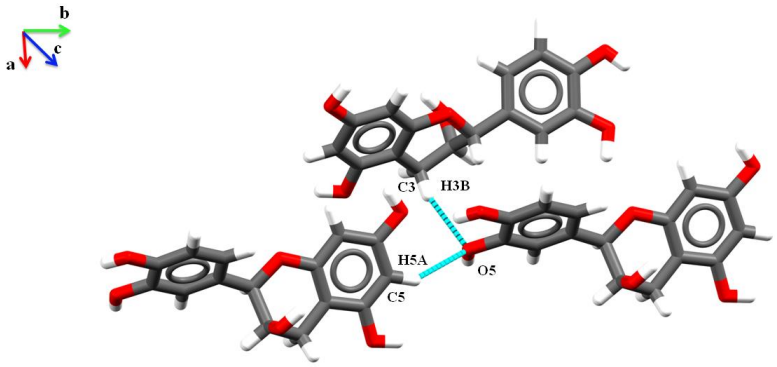

(c)

O HS é utilizado para confirmar as interações intermoleculares no empacotamento cristalino por análise topológica, através do raio de Van der Waals. A dnorm HS (variando de -0,511 a 1,470 Å) é mostrada na Figura 6. Os pontos vermelhos (1), (3), (5) e (10) correspondem aos contatos *de*, indicando onde as moléculas atuam como aceitadoras de O2–H2…O6, O3–H3…O2, O5–H5…O1, e O4–H4…O3 respectivamente. Os pontos vermelhos (2), (4), (6) e (9) referem-se a contatos *di*, indicando onde as moléculas atuam como doadoras de O2–H2…O6, O3–H3…O4, O5–H5…O1, e O6–H6…O4 respectivamente. Os pontos claros (7), (8) e (11) indicam interações fracas (devido à grande distância entre doador e aceitador) e atuam como aceitadores para C7–H7…O3, C5–

H5A…O5 e C3–H3B… O5, respectivamente. Esta análise auxilia na descrição das interações que são as mais dominantes entre as moléculas.

Figura 6. A superfície de Hirshfeld indica interações intermoleculares de EPC. As interações são representadas por linhas pretas pontilhadas.

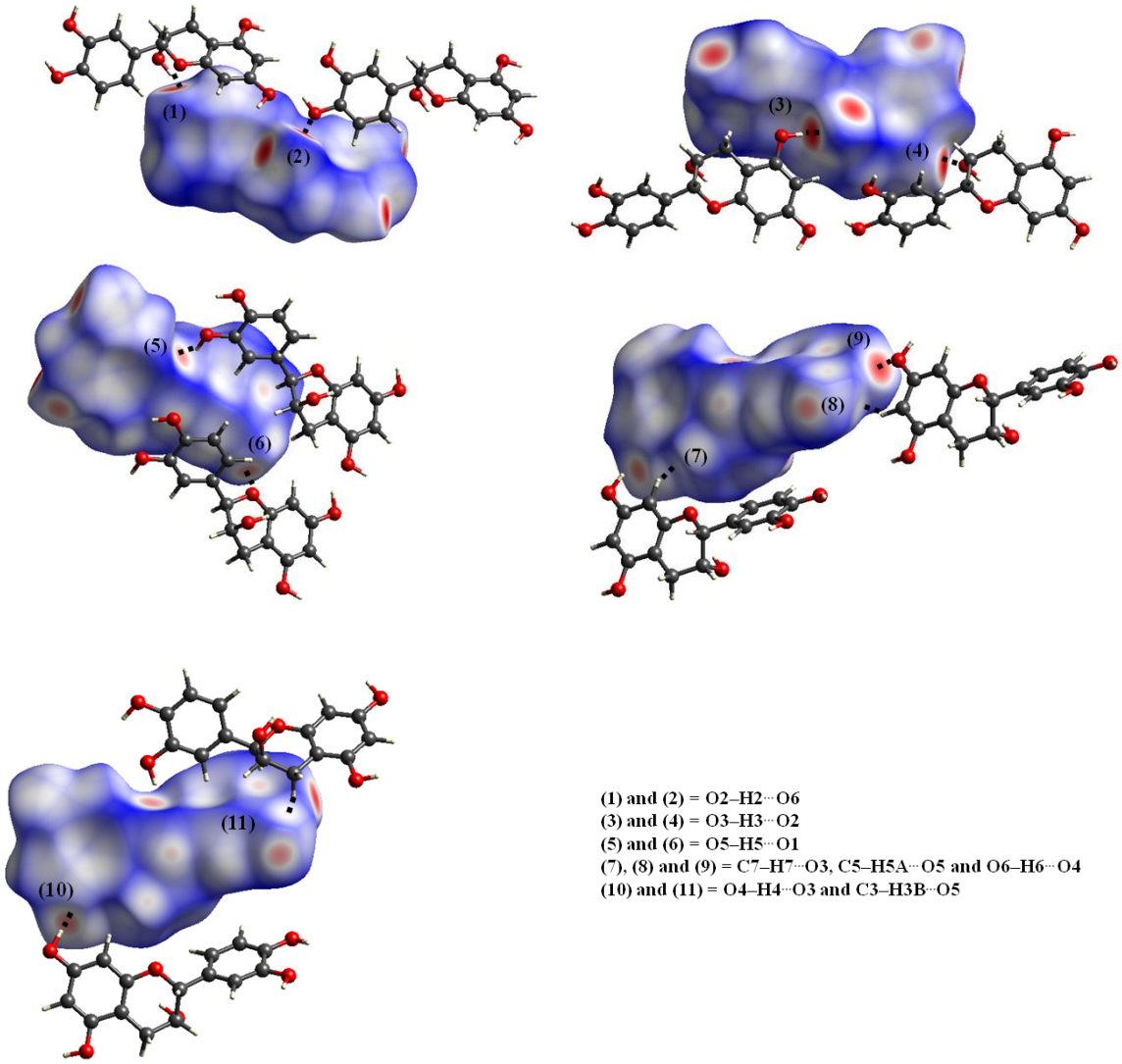

A impressão digital é o gráfico de *di* e *de* plotado bidimensionalmente, obtendo-se os mapas completos de contatos presentes nas moléculas com suas respectivas porcentagens. A impressão digital do EPC é mostrada na Figura 7. Por ser uma molécula orgânica, possui maior porcentagem de contatos H–H (35,90%), com as coordenadas *di*=*de*= 1,4. O contato O–H tem uma porcentagem de 33,30%

do total presente na molécula, indicando interações C–H…O e O–H…O. Além disso, o contato C–H (25,3%) também representa a interação C–H… π.

Figura 7. Quantificação de diferentes tipos de contatos e a impressão digital do EPC estabelecido.

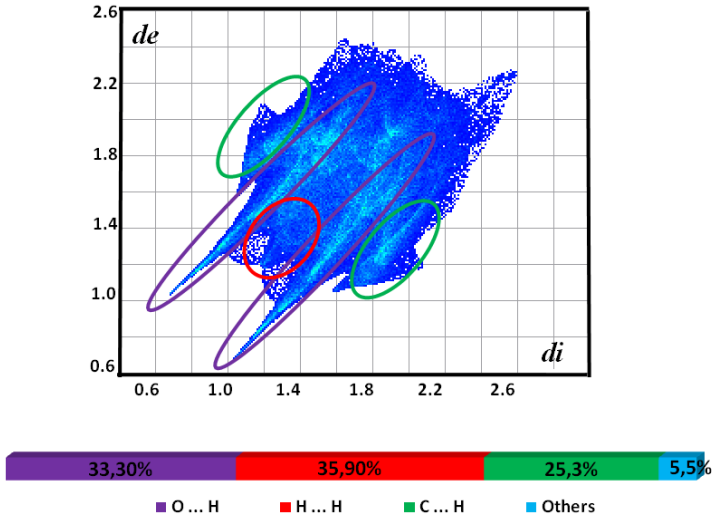

3.2 Cálculos teóricos da EPC

A teoria quântica de átomos em moléculas (QTAIM) é uma abordagem para analisar diferentes interações intra e intermoleculares com base na densidade eletrônica do sistema molecular(GRABOWSKI, 2011). A ligação de hidrogênio é caracterizada por ter um papel importante nos processos químicos, físicos e bioquímicos. Essas interações podem ser descritas e visualizadas com a ajuda de um gráfico molecular, que mostra o caminho de ligação crucial que liga os átomos receptores de prótons, conforme mostrado na Figura 8. As interações de ligações de hidrogênio baseadas em energia (ROZAS; ALKORTA; ELGUERO, 2000) são fracas, médias e fortes quando as ligações de hidrogênio têm |EHb| < 12 kcal mol^{-1}, 12 kcal mol^{-1} < |EHb| < 24 kcal mol^{-1} e |EHb| > 24 kcal mol^{-1}, respectivamente. Três interações homonucleares de hidrogênio clássicas (O2–H2…O6, O3–H3…O2 e O6–H6…O5) foram classificadas como fortes. As interações intermoleculares O6–H6…O4 e O5–H5…O1 foram classificadas como de força média, embora as demais sejam classificadas como de força fraca. O arranjo supramolecular é estabilizado por ligações clássicas de hidrogênio O–H…O e

ligações não clássicas de hidrogênio C–H…O. Além disso, a interação hidrofóbica C–H…π contribui para essa estabilidade estrutural. O maior valor de EHB para O3–H3…O2 é atribuído à distância próxima 2,694 Å doador-aceptor e à direção 176° para esta interação. Em contraste, o caráter mais fraco de C7–H7…O3 é devido a este compartilhamento de elétrons pelo O3 e a nenhuma direção (110°).

Figura 8. Os gráficos moleculares mostrando os BCPs como pontos amarelos.

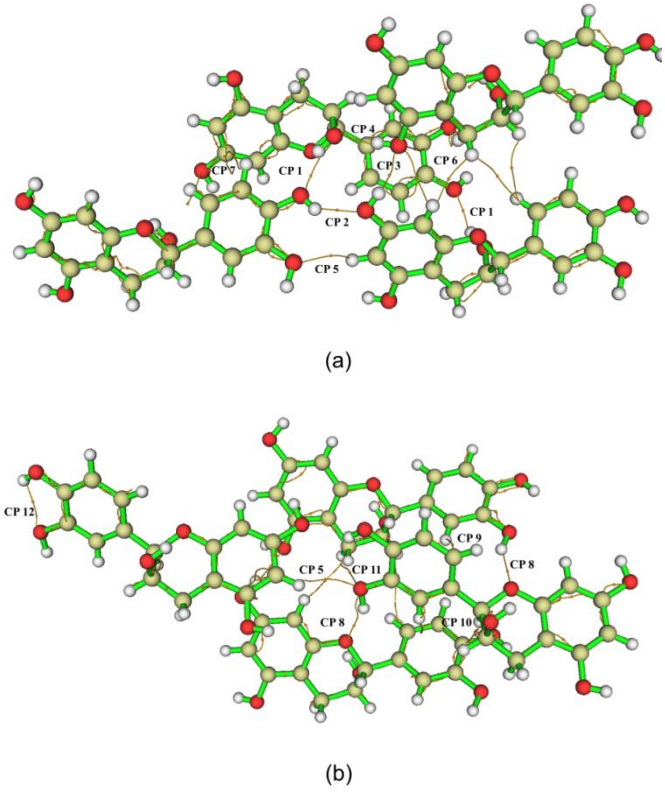

As interações ligação-antiligação da análise do orbital de ligação natural (NBO) são levadas em consideração pela base de Lewis preenchida (doadora) e ácido de Lewis vazio (aceitador). O HOMO como o elétron doador está localizado na ligação p, que é característica da região nucleofílica. O resultado HOMO é negativo (-180,85 kcal/mol) e aparece como um orbital de ligação p. O orbital LUMO é um orbital antiligante p localizado no C11=C12 próximo ao grupo

hidroxila (O5-H5). O LUMO para EPC é positivo (29,81 kcal/mol). Esta análise orbital indica que esta molécula é quimicamente estável (Figura 9).

Figura 9. Orbitais moleculares de fronteira para EPC **(a)** o orbital de ligação HOMO e **(b)** o orbital antiligante LUMO derivado da análise NBO no nível de teoria M06-2X/6-311+ +G(d,p) com o valor iso de 0,05 unidades atômicas.

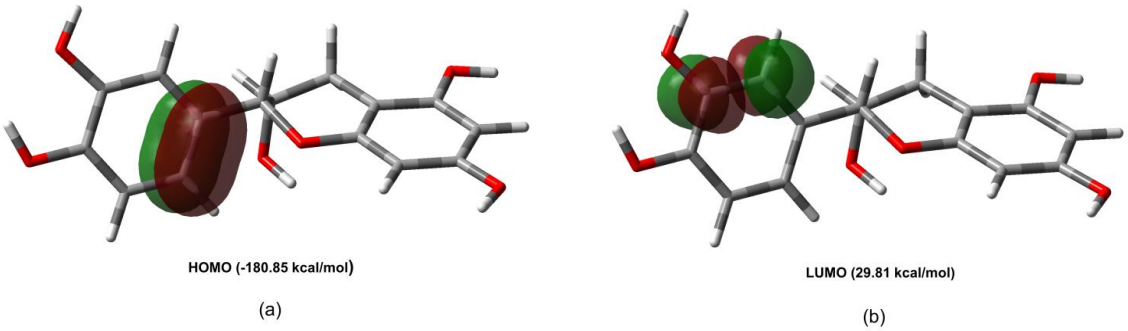

O mapa potencial eletroestático (MEP) é uma importante ferramenta físico-química que dá informações sobre a reatividade química da molécula. Para entender o MPE feito para EPC usamos a representação tridimensional MEP (Figura 10), onde amarelo-laranja especifica a região mais negativa (atração moderada) e está localizada no átomo de oxigênio (O2) do grupo hidroxila de heterocíclico, com valor de cerca de 45,80 kcal/mol. Por outro lado, a região azul especificada o potencial mais positivo (repulsão mais forte) e o energia potencial isovalor de cerca de 32,63 kcal/mol está em torno do átomo de hidrogênio (H5). Nesta região, o grupo hidroxila na posição para com o anel aromático é responsável pelo efeito de retirada de elétrons.

Figura 10. A superfície de potencial eletrostático molecular mapeada para EPC **(a)** a região de cor amarelo-laranja é rica em elétrons, **(b)** e a região de cor azul é deficiente em elétrons.

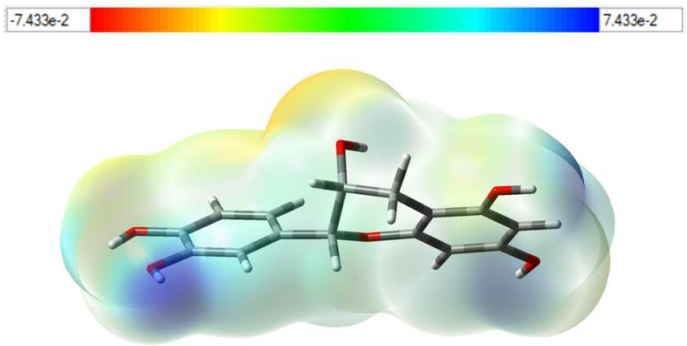

3.3 Caracterização do estado sólido da CHL-o

A Figura 1 mostra o esquema de numeração usado para CHL-o, que cristaliza no grupo espacial ortorrômbico, centrossimétrico *Pbca*. O Anel A (trimetilciclohexeno) é desordenado com dois sítios independentes para os átomos C14, C15 (67,4%) e C14', C15' (32,6%). O anel B (nitrobenzeno) tem um grupo p-nitro (Figura 11).

Figura 11. Representação Ortep do cristal CHL-o com elipsóides de 50% de probabilidade. Desordem em C14' e C15' omitido para maior clareza.

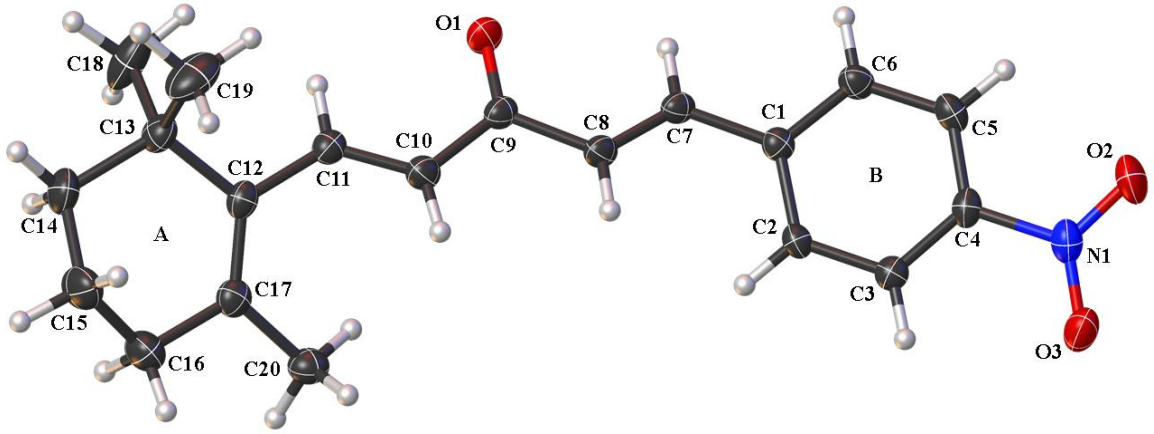

O arranjo supramolecular de CHL-o tem uma interação C5–H5…O3 [D…A = 3,449 Å; código de simetria: 3/2-x, -1/2+y, z] envolvendo o grupo nitro que contribui para uma repetição cruzada em zig-zag na direção do eixo *b* (Figura 12a), e a interação C8–H8…O1 [D…A = 3,305 Å; código de simetria: 1/2-x, 1/2+y, z] envolvendo o grupo carbonila em uma repetição ao longo da direção do eixo *b* (Figura 12b).

Figura 12. Interações de CHL-o formadas por C5–H5…O3 **(a)**, e C8–H8…O1 **(b)**. Os átomos de H não envolvidos nas interações foram omitidos.

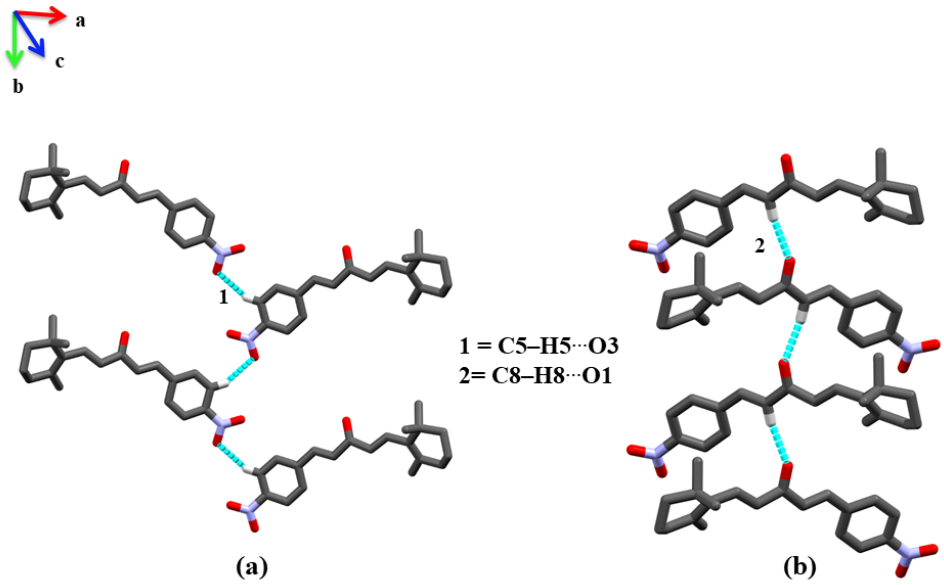

Os contatos C8–H8…O1 e C5–H5…O3 são observados através da análise topológica HS por mapeamento *dnorm* convencional (variando de -0,511 a 1,470 Å) (Figura 13a e Figura 13b) e podem ser descritos a partir da intensidade do *di* e *de* contatos. Os pontos vermelhos (1d) e (2d) correspondem aos contatos *di*, indicando que atuam como doadores para as interações C8–H8…O1 e C5–H5…O3, respectivamente, e os pontos vermelhos (1r) e (2r) correspondem aos contatos *de*, indicando as regiões aceitadoras das interações C8 – H8… O1 e C5 – H5…O3, respectivamente.

Figura 13. HS dnorm mapeado para CHL-o indica contatos intermoleculares. As linhas pretas pontilhadas representam ligações de hidrogênio.

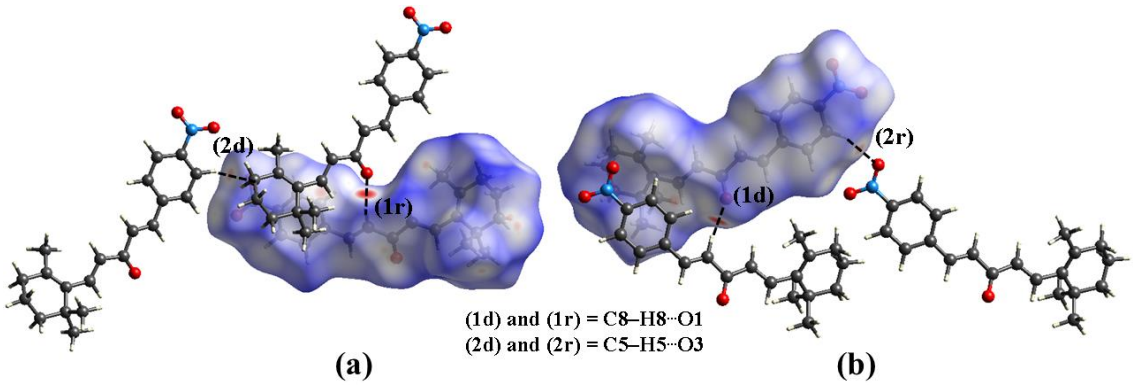

Além disso, os contatos foram analisados a partir de impressões digitais (Figura 14) com base no componente de desordem principal da molécula através de um gráfico 2D com *di* e *de*. Os contatos H...H têm uma porcentagem maior (50,10%), os contatos O...H têm 25,90% e os contatos C...H têm 18,60%. A ausência de interações C...C indica que o arranjo não é estabilizado por interações π...π.

Figura 14. Impressão digital e quantificação de interações totais em CHL-o.

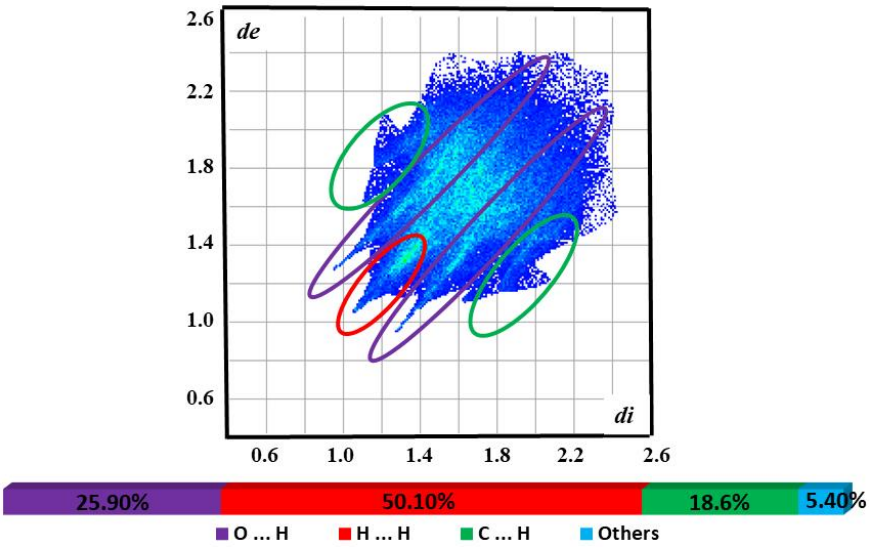

3.4 Comparativo dos polimorfos CHL-o, CHL-m_1 e CHL-m_2

Polimorfos de sistemas cristalinos monoclínicos foram obtidos através do banco de dados CCDC [code: 1029766 (CHL-m_1) and 818053 (CHL-m_2)] e comparados através do Gap de energia. O orbital ligante e o orbital antiligante são caracterizados pelos níveis eletrônicos HOMO e LUMO, respectivamente (GRANT; RICHARDS, 1996), e a diferença entre os orbitais de energias é chamada de energia GAP (ELUMO – EHOMO = EGAP). O GAP para CHL-o é 531,8 kJ/mol, para CHL-m1 é 581,3 kJ/mol enquanto para CHL-m2 é 520,7 kJ/mol.

A energia GAP tem sido utilizada como um simples indicador de estabilidade cinética(SANTOS et al., 2014), esta estabilidade cinética pode ser entendida como estabilidade relacionada ao complexo ativado de qualquer outra reação química (MANOLOPOULOS; MAY; DOWN, 1991). Devido ao imenso número de reações químicas, é muito complicado estimar o grau de estabilidade cinética. Nesse sentido, o composto CHL-m_1 é o mais estável entre os três (581,3 kJ/mol) quando comparado ao CHL-o e CHL-m_2 (em relação aos valores da fase gasosa). Ao comparar as estruturas CHL-o e CHL-m_2, o valor GAP de CHL-o (531,8 kJ/mol) indica que esta estrutura é mais estável que CHL-m_2 (520,7 kJ/mol). Resumindo, temos uma ordem de estabilidade na fase gasosa de CHL-m_1 > CHL-o > CHL-m_2 (Figura 15).

Figura 15. Distribuições orbitais moleculares (HOMO-LUMO) para CHL-o, CHL-m_1 e CHL-m*2*.

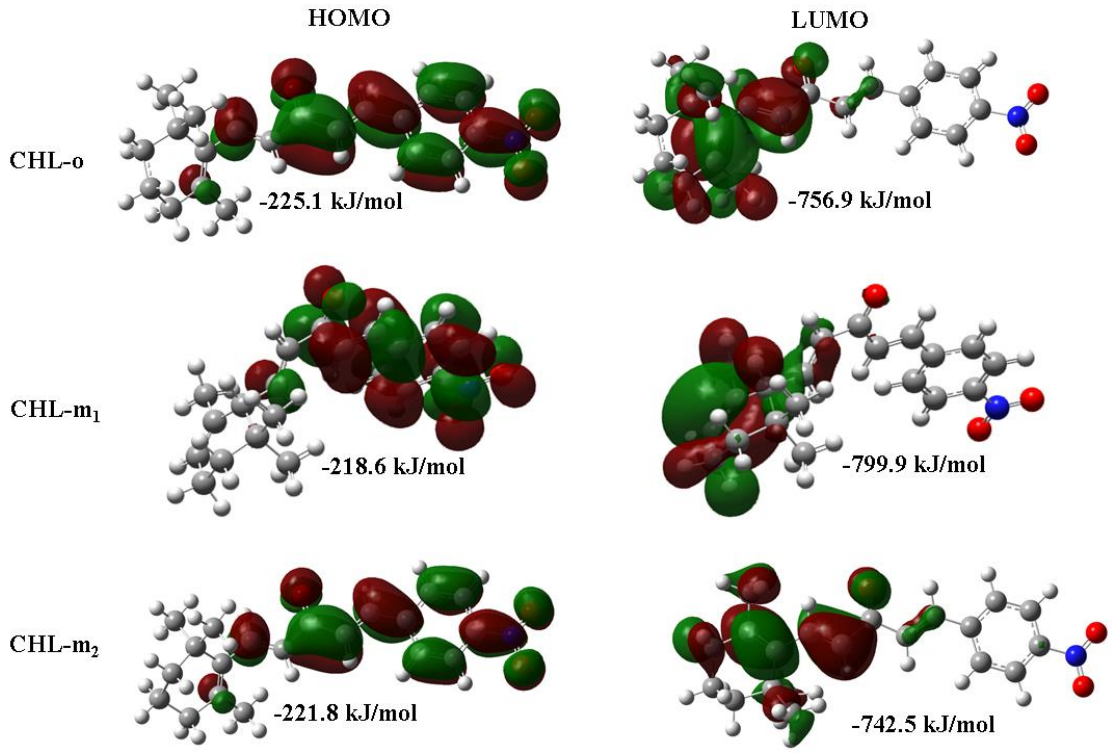

4 CONSIDERAÇÕES FINAIS

O presente trabalho dedicou-se à caracterização estrutural de duas moléculas da classe dos flavonóides, sendo a *epicatequina* obtida pela extração da planta *Salacia crassifólia,* e a chalcona terpenóide obtida através da síntese de Claisen-Schimdt. Os compostos foram estruturalmente elucidados cristalograficamente, através da difração de raios-X por monocristais, gerando os seguintes depósitos no CCDC 1948660 (*epicatequina*) e 2023065 (chalcona terpenóide). As interações intermoleculares, as análises topológicas e os cálculos teóricos obtidos (que tiveram por objetivo confirmar os resultados obtidos experimentalmente) indicam a planaridade conformacional de ambos compostos.

A epicatequina tem arranjo supramolecular dominado por interações intermoleculares clássicas e uma interação intramolecular, interações semi-clássicas, e hidrofóbicas – todas confirmadas por meio de análises topológicas. A análise de QTAIM observou a topologia através do ponto crítico de ligação (BCP), associada a interação inter e intramolecular, que são consistentes com o arranjo supramolecular cristalino. Cálculos teóricos como FMO e HOMO/LUMO demonstraram a estabilidade química da molécula, tendo os valores de HOMO, -180,85 kcal/mol no orbital de ligação π, e LUMO, 29,81 kcal/mol no orbital anti-ligante π. O MEP informou onde a molécula interage intermolecularmente identificando os locais de ataque nucleofílicos e eletrofílicos, onde o átomo denominado O2 apresentou moderada atração, enquanto o átomo H5 apresentou uma forte repulsão. O artigo na íntegra pode ser encontrado no Anexo I.

A chalcona terpenóide cristalizou-se no grupo espacial ortorrômbico com arranjo supramolecular estabilizado por interações C–H···O e C–H···π. A comparação do Gap de energia teórico desta conformação com dois outros polimorfos disponíveis no CCDC indicou que esta conformação observada não de menor energia. A análise estrutural da chalcona terpenóide (assim como da epicatequina) permitem futuros estudos de relação estrutura-atividade visando

aprimorar os modelos moleculares observados. O artigo na íntegra pode ser encontrado no Anexo II.

5 REFERÊNCIAS

AGRAWAL, A. D. Pharmacological Activities of Flavonoids : A Review. **International Journal of Pharmaceutical Sciences and Nanotechnology**, v. 4, n. 2, p. 1394–1398, 2011.

AITIPAMULA, S.; VANGALA, V. R. X-Ray Crystallography and its Role in Understanding the Physicochemical Properties of Pharmaceutical Cocrystals. **Journal of the Indian Institute of Science**, v. 97, n. 2, p. 227–243, 2017.

ALBERS, A. P. F. et al. Um método simples de caracterização de argilominerais por difração de raios X (A simple method for the characterization of clay minerals by X-ray diffraction). **Cerâmica**, v. 48, n. 305, p. 34–37, 2002.

ARROIO, A.; HONÓRIO, K. M.; SILVA, A. B. F. DA. Propriedades químico-quânticas empregadas em estudos das relações estrutura-atividade. **Química Nova**, v. 33, n. 3, p. 694–699, 2010.

ATINKS, P.; JONES, L. **Princípios de química: questionando a vida moderna e o meio ambiente.** 5 ed. ed. Porto Alegre: Bookman, 2012.

BABA, S. et al. ABSORPTION AND URINARY EXCRETION OF PROCYANIDIN B2 [EPICATECHIN-(4β-8)-EPICATECHIN] IN RATS. **Free Radical Biology and Medicine**, v. 33, n. 1, p. 142–148, 2002.

BHALE, P. S. et al. Synthesis of extended conjugated indolyl chalcones as potent anti-breast cancer, anti-inflammatory and antioxidant agents. **Bioorganic and Medicinal Chemistry Letters**, v. 27, n. 7, p. 1502–1507, 2017.

BORCHARDT-OTT, W. **Crystallography, An Introduction**. 3rd ed. ed. New York: Springer-Verlag Berlin Heidelberg, 2011.

BRAGG, W. H.; BRAGG, W. L. Reflection of X-rays by crystals. **Proceedings of the royal society**, v. 27, p. 428–438, 1913.

BROOKS-BARTLETT, J. C.; GARMAN, E. F. The nobel science: One Hundred Years of Crystallography. **Interdisciplinary Science Reviews**, v. 40, n. 3, p. 244–264, 2015.

CHATTERJEE, S. K. **Crystallography and the World of Symmetry**. 1 ed ed. Berlim: Springer-Verlag Berlin Heidelberg, 2008.

CIOFFI, G. et al. Antioxidant chalcone glycosides and flavanones from Maclura (Chlorophora) tinctoria. **Journal of Natural Products**, v. 66, n. 8, p. 1061–1064, 2003.

CLEGG, W. et al. **Crystal Structure Analysis: Principles and Practice**. 2nd ed. ed. New York: Oxford University Press, 2009.

COSKUN, D. et al. Novel 1-(7-ethoxy-1-benzofuran-2-yl) substituted chalcone derivatives: Synthesis, characterization and anticancer activity. **European Journal of Medicinal Chemistry**, v. 136, p. 212–222, 2017.

DOAN, T. N.; TRAN, D. T. Synthesis, Antioxidant and Antimicrobial Activities of a Novel Series of Chalcones, Pyrazolic Chalcones, and Allylic Chalcones. **Pharmacology & Pharmacy**, v. 02, n. 04, p. 282–288, 2011.

DOWER, J. I. et al. Effects of the pure flavonoids epicatechin and quercetin on vascular function and cardiometabolic health : a randomized , double-blind , placebo-controlled, crossover trial. **The American Journal of Clinical Nutrition**, v. 101, n. 5, p. 914–921, 2015.

ENGLER, M. B. et al. Journal of the American College of Nutrition Flavonoid-Rich Dark Chocolate Improves Endothelial Function and Increases Plasma Epicatechin Concentrations in Healthy Adults Flavonoid-Rich Dark Chocolate Improves Endothelial Function and Increases Plasma Epi. n. November, p. 37–41, 2013.

FRAGA, C. G.; OTEIZA, P. I.; GALLEANO, M. Plant bioactives and redox signaling : (-)-Epicatechin as a paradigm. **Molecular Aspects of Medicine 61**, v. 61, p. 31–40, 2018.

FUNAKOSHI-TAGO, M. et al. Anti-inflammatory activity of flavonoids in Nepalese propolis is attributed to inhibition of the IL-33 signaling pathway. **International Immunopharmacology**, v. 25, n. 1, p. 189–198, 2015.

GAONKAR, S. L.; VIGNESH, U. N. Synthesis and pharmacological properties of chalcones: a review. **Research on Chemical Intermediates**, v. 43, n. 11, p. 6043–6077, 2017.

GIACOVAZZO, C. et al. **Fundamentals of Crystallography**. 3rd ed. ed. New York: Oxford: IUCR - Oxford University Press, 2011.

GLUSKER, J. P.; LEWIS, M.; ROSSI, M. **Crystal Structure Analysis for Chemists and Biologists**. 1 ed. ed. New York: WILEY-VCH, 1994.

GLUSKER, J. P.; TRUEBLOOD, K. N. **Crystal Structure Analysis**. 3rd ed. ed. New York: Oxford University Press, 2010.

GO, M.; WU, X.; LIU, X. Chalcones: An Update on Cytotoxic and Chemoprotective Properties. **Current Medicinal Chemistry**, v. 12, n. 4, p. 483–499, 2005.

GÓRNIAK, I.; BARTOSZEWSKI, R.; KRÓLICZEWSKI, J. Comprehensive review of antimicrobial activities of plant flavonoids. **Phytochemistry Reviews**, v. 18, n. 2, p. 241–272, 2018.

GRABOWSKI, S. J. What Is the Covalency of Hydrogen Bonding? **Chemical Reviews**, v. 111, n. 4, p. 2597–2625, 2011.

GRANT, G. H.; RICHARDS, W. G. **Computational Chemistry**. Oxford: Oxford Science Publications, 1996.

GUANTAI, E. M. et al. Enone- and chalcone-chloroquinoline hybrid analogues: In silico guided design, synthesis, antiplasmodial activity, in vitro metabolism, and mechanistic studies. **Journal of Medicinal Chemistry**, v. 54, n. 10, p. 3637–3649, 2011.

HARBORNE, J. B.; WILLIAMS, C. A. Advances in flavonoid research since 1992. **Phytochemistry**, v. 55, n. 6, p. 481–504, 2000.

HAUPRMAN, H. Direct Methods of X-ray Crystallography. **Science**, v. 233, n. 4760, p. 178–183, 1986.

HAVSTEEN, B. H. Flavonoides, a class of natural products of high pharmacological potency. **Biochemical pharmacology**, v. 32, n. 7, p. 1141–1148, 1983.

HAVSTEEN, B. H. The biochemistry and medical significance of the flavonoids. **Pharmacology & Therapeutics**, v. 96, n. 2–3, p. 67–202, 2002.

HERMOSO, A. et al. Antileishmanial activities of dihydrochalcones from piper elongatum and synthetic related compounds. Structural requirements for activity. **Bioorganic and Medicinal Chemistry**, v. 11, n. 18, p. 3975–3980, 2003.

HIRAI, S. et al. Inhibitory effect of naringenin chalcone on inflammatory changes in the interaction between adipocytes and macrophages. **Life Sciences**, v. 81, n. 16, p. 1272–1279, 2007.

KOVALCHUK, M. V. Crystallography as a Methodology for Scientific Development in the 21st Century: A Review. **Crystallography Reports**, v. 56, n. 4, p. 539–552, 2011.

MANOLOPOULOS, D. E.; MAY, J. C.; DOWN, S. E. Theoretical studies of the fullerenes: C34 to C70. **Chemical Physics Letters**, v. 181, n. 2–3, p. 105–111, jun. 1991.

MCKINNON, J. J.; SPACKMAN, M. A.; MITCHELL, A. S. Novel tools for visualizing and exploring intermolecular interactions in molecular crystals.

Acta Crystallographica Section B: Structural Science, Crystal Engineering and Materials, v. B60, p. 627–668, 2004.

NOWAKOWSKA, Z. A review of anti-infective and anti-inflammatory chalcones. **European Journal of Medicinal Chemistry**, v. 42, n. 2, p. 125–137, 2007.

PANCHE, A. N.; DIWAN, A. D.; CHANDRA, S. R. Flavonoids: an overview. **Journal of Nutritional Science**, v. 5, n. 47, p. 1–15, 2016.

PATTERSON, A. L. A Fourier Series Method for the Determination of the Components of Interatomic Distances in Crystals. **Physical Review**, v. 46, n. 1929, p. 372–376, 1934.

PRAKASH, M.; BASAVARAJ, B. V; MURTHY, K. N. C. Biological functions of epicatechin : Plant cell to human cell health. v. 52, n. August 2018, p. 14–24, 2019.

RAMMOHAN, A. et al. Chalcone synthesis, properties and medicinal applications: a review. **Environmental Chemistry Letters**, v. 18, p. 433–458, 2020.

RASHID, U. et al. Structure based medicinal chemistry-driven strategy to design substituted dihydropyrimidines as potential antileishmanial agents. **European Journal of Medicinal Chemistry**, v. 115, p. 230–244, 2016.

ROZAS, I.; ALKORTA, I.; ELGUERO, J. Behavior of ylides containing N, O, and C atoms as hydrogen bond acceptors. **Journal of the American Chemical Society**, v. 122, n. 45, p. 11154–11161, 2000.

ROZMER, Z.; PERJÉSI, P. Naturally occurring chalcones and their biological activities. **Phytochemistry Reviews**, v. 15, n. 1, p. 87–120, 2016.

SACZEWSKI, F. et al. Carbonic anhydrase inhibitors: Inhibition of human cytosolic isozymes I and II and tumor-associated isozymes IX and XII with S-substituted 4-chloro-2-mercapto-5-methyl-benzenesulfonamides. **Bioorganic and Medicinal Chemistry**, v. 16, n. 7, p. 3933–3940, 2008.

SANTOS, C. B. R. et al. Application of Hartree-Fock Method for Modeling of Bioactive Molecules Using SAR and QSPR. **Computational Molecular Bioscience**, v. 04, n. 01, p. 1–24, 2014.

SARBU, L. G. et al. Synthetic flavonoids with antimicrobial activity : a review. **Journal of Applied Microbiology**, v. 127, n. 5, p. 1282–1290, 2019.

SCHROETER, H. et al. (-)-Epicatechin mediates beneficial effects of

flavanol-rich cocoa on vascular function in humans. **Proceedings of the National Academy of Sciences**, v. 103, n. 4, p. 1024–1029, 2006.

SCHROETER, H. et al. (-)Epicatechin stimulates ERK-dependent cyclic AMP response element activity and up-regulates GluR2 in cortical neurons. **Journal of Neurochemistry**, v. 101, n. 6, p. 1596–1606, 2007.

SHARMA, A.; TULI, H. S.; SHARMA, A. K. Chemistry and Synthetic Overview of Flavonoids. In: **Current Aspects of Flavonoids: Their Role in Cancer Treatment**. Singapore: Springer, 2019. p. 23–38.

SPACKMAN, M. A.; JAYATILAKA, D. Hirshfeld surface analysis. **CrystEngComm**, v. 11, n. 1, p. 19–32, 2009.

SPACKMAN, M. A.; MCKINNON, J. J. Fingerprinting intermolecular interactions in molecular crystals. **CrystEngComm**, v. 4, n. 66, p. 378–392, 2002.

STOCK, S. R. et al. **Elements of X-Ray Diffraction:** 3rd ed. ed. New York: Prentice-Hall, 2001.

STOUT, G. H.; JENSEN, L. H. **X-Ray Structure Determination: A Practical Guide**. 2nd ed. ed. New Jersey: Wiley-Interscience, 1989.

STRINGER, T. P. et al. Plant-derived fl avanol (−) epicatechin mitigates anxiety in association with elevated hippocampal monoamine and BDNF levels , but does not in fl uence pattern separation in mice. v. 5, n. 1, p. e493-9, 2015.

TILLEY, R. J. D. **Cristalografia: cristais e estruturas cristalinas**. 1. ed. São Paulo: Oficina de Textos, 2014.

USÓN, I.; SHELDRICK, G. M. Advances in direct methods for protein crystallography. **Process Safety and Environmental Protection**, v. 9, n. 5, p. 643–648, 1999.

WANG, T.; LI, Q.; BI, K. Bioactive flavonoids in medicinal plants : Structure , activity and biological fate. **Asian Journal of Pharmaceutical Sciences**, v. 13, n. 1, p. 12–23, 2018.

WATKIN, D. J. Chemical crystallography – science , technology or a black art. **Crystallography Reviews**, v. 16, n. 3, p. 197–230, 2010.

WOOLFSON, M. M. **An introduction to X-ray crystallography**. Second ed. New York: Cambridge University Press, 1997.

WU, W. et al. Millepachine, a novel chalcone, induces G2/M arrest by inhibiting CDK1 activity and causing apoptosis via ROS-mitochondrial apoptotic

pathway in human hepatocarcinoma cells in vitro and in vivo. **Carcinogenesis**, v. 34, n. 7, p. 1636–1643, 2013.

XIA, E. et al. Biological Activities of Polyphenols from Grapes. **International Journal of Molecular Sciences**, v. 11, n. 2, p. 622–646, 2010.

Anexo I

Artigo científico publicado no ***Chemistry Select*** (2019), 4, 14012– 14020.

DOI: 10.1002/slct.20190330

JOHN WILEY AND SONS LICENSE
TERMS AND CONDITIONS

Jan 23, 2022

This Agreement between Mrs. Marianna Silva ("You") and John Wiley and Sons ("John Wiley and Sons") consists of your license details and the terms and conditions provided by John Wiley and Sons and Copyright Clearance Center.

License Number	5234950830934
License date	Jan 23, 2022
Licensed Content Publisher	John Wiley and Sons
Licensed Content Publication	ChemistrySelect
Licensed Content Title	A Comprehensive Topological Analysis of a Novel Flavonoid Extracted from Brazilian Cerrado Plants
Licensed Content Author	Hamilton B. Napolitano, Ademir J. Camargo, Antônio C. S. Menezes, et al
Licensed Content Date	Dec 18, 2019
Licensed Content Volume	4
Licensed Content Issue	47
Licensed Content Pages	9
Type of use	Dissertation/Thesis
Requestor type	Author of this Wiley article

Format	Print and electronic
Portion	Full article
Will you be translating?	No
Title	A Comprehensive Topological Analysis of a Novel Flavonoid Extracted from Brazilian Cerrado Plants
Institution name	Universidade Estadual de Goiás
Expected presentation date	Jan 2022
Requestor Location	Mrs. Marianna Silva Rua João da Cunha Rodovalho, Esquina com Anapolis, GO 75123460 Brazil Attn: Universidade Evangélica de Goi
Publisher Tax ID	EU826007151
Customer VAT ID	BR62992718754
Total	0.00 USD

Terms and Conditions

TERMS AND CONDITIONS

This copyrighted material is owned by or exclusively licensed to John Wiley & Sons, Inc. or one of its group companies (each a"Wiley Company") or handled on behalf of a society with which a Wiley Company has exclusive publishing rights in relation to a particular work (collectively "WILEY"). By clicking "accept" in connection with completing this licensing transaction, you agree that the following terms and conditions apply to this transaction (along with the billing and payment terms and conditions established by the Copyright Clearance Center Inc., ("CCC's Billing and Payment terms and conditions"), at the time that you opened your RightsLink account (these are available at any time at http://myaccount.copyright.com).

Terms and Conditions

- The materials you have requested permission to reproduce or reuse (the "Wiley Materials") are protected by copyright.

- You are hereby granted a personal, non-exclusive, non-sub licensable (on a stand-alone basis), non-transferable, worldwide, limited license to reproduce the Wiley Materials for the purpose specified in the licensing process. This license, **and any CONTENT (PDF or image file) purchased as part of your order,** is for a one-time use only and limited to any maximum distribution number specified in the license. The first instance of republication or reuse granted by this license must be completed within two years of the date of the grant of this license (although copies prepared before the end date may be distributed thereafter). The Wiley Materials shall not be used in any other manner or for any other purpose, beyond what is granted in the license. Permission is granted subject to an appropriate acknowledgement given to the author, title of the material/book/journal and the publisher. You shall also duplicate the copyright notice that appears in the Wiley publication in your use of the Wiley Material. Permission is also granted on the understanding that nowhere in the text is a previously published source acknowledged for all or part of this Wiley Material. Any third party content is expressly excluded from this permission.

- With respect to the Wiley Materials, all rights are reserved. Except as expressly granted by the terms of the license, no part of the Wiley Materials may be copied, modified, adapted (except for minor reformatting required by the new Publication), translated, reproduced, transferred or distributed, in any form or by any means, and no derivative works may be made based on the Wiley Materials without the prior permission of the respective copyright owner.**For STM Signatory Publishers clearing permission under the terms of the STM Permissions Guidelines only, the terms of the license are extended to include subsequent editions and for editions in other languages, provided such editions are for the work as a whole in situ and does not involve the separate exploitation of the permitted figures or extracts,** You may not alter, remove or suppress in any manner any copyright, trademark or other notices displayed by the Wiley Materials. You may not license, rent, sell, loan, lease, pledge, offer as security, transfer or assign the Wiley Materials on a stand-alone basis, or any of the rights granted to you hereunder to any other person.

- The Wiley Materials and all of the intellectual property rights therein shall at all times remain the exclusive property of John Wiley & Sons Inc, the Wiley Companies, or their respective licensors, and your interest therein is only that of having possession of and the right to reproduce the Wiley Materials pursuant to Section 2 herein during the continuance of this Agreement. You agree that you own no right, title or interest in or to the Wiley Materials or any of the intellectual property rights therein. You shall have no rights hereunder other than the license as provided for above in Section 2. No right, license or interest to any trademark, trade name, service mark or other branding ("Marks") of WILEY or its licensors is granted hereunder, and you agree that you shall not assert any such right, license or interest with respect thereto

- NEITHER WILEY NOR ITS LICENSORS MAKES ANY WARRANTY OR REPRESENTATION OF ANY KIND TO YOU OR ANY THIRD PARTY, EXPRESS, IMPLIED OR STATUTORY, WITH RESPECT TO THE MATERIALS OR THE ACCURACY OF ANY INFORMATION CONTAINED IN THE MATERIALS, INCLUDING, WITHOUT LIMITATION, ANY IMPLIED WARRANTY OF MERCHANTABILITY, ACCURACY, SATISFACTORY QUALITY, FITNESS FOR A PARTICULAR PURPOSE, USABILITY, INTEGRATION OR NON-INFRINGEMENT AND ALL SUCH WARRANTIES ARE HEREBY EXCLUDED BY WILEY AND ITS LICENSORS AND WAIVED BY YOU.

- WILEY shall have the right to terminate this Agreement immediately upon breach of this Agreement by you.

- You shall indemnify, defend and hold harmless WILEY, its Licensors and their respective directors, officers, agents and employees, from and against any actual or threatened claims, demands, causes of action or proceedings arising from any breach of this Agreement by you.

- IN NO EVENT SHALL WILEY OR ITS LICENSORS BE LIABLE TO YOU OR ANY OTHER PARTY OR ANY OTHER PERSON OR ENTITY FOR ANY SPECIAL, CONSEQUENTIAL, INCIDENTAL, INDIRECT, EXEMPLARY OR PUNITIVE DAMAGES, HOWEVER CAUSED, ARISING OUT OF OR IN CONNECTION WITH THE DOWNLOADING, PROVISIONING, VIEWING OR USE OF THE MATERIALS REGARDLESS OF THE FORM OF ACTION, WHETHER FOR BREACH OF CONTRACT, BREACH OF WARRANTY, TORT, NEGLIGENCE, INFRINGEMENT OR OTHERWISE (INCLUDING, WITHOUT LIMITATION, DAMAGES BASED ON LOSS OF PROFITS, DATA, FILES, USE, BUSINESS OPPORTUNITY OR CLAIMS OF THIRD PARTIES), AND WHETHER OR NOT THE PARTY HAS BEEN ADVISED OF THE POSSIBILITY OF SUCH DAMAGES. THIS LIMITATION SHALL APPLY NOTWITHSTANDING ANY FAILURE OF ESSENTIAL PURPOSE OF ANY LIMITED REMEDY PROVIDED HEREIN.

- Should any provision of this Agreement be held by a court of competent jurisdiction to be illegal, invalid, or unenforceable, that provision shall be deemed amended to achieve as nearly as possible the same economic effect as the original provision, and the legality, validity and enforceability of the remaining provisions of this Agreement shall not be affected or impaired thereby.

- The failure of either party to enforce any term or condition of this Agreement shall not constitute a waiver of either party's right to enforce each and every term and condition of this Agreement. No breach under this agreement shall be deemed waived or excused by either party unless such waiver or consent is in writing signed by the party granting such waiver or consent. The waiver by or consent of a party to a breach of any provision of this Agreement shall not operate or be construed as a waiver of or consent to any other or subsequent breach by such other party.

- This Agreement may not be assigned (including by operation of law or otherwise) by you without WILEY's prior written consent.

- Any fee required for this permission shall be non-refundable after thirty (30) days from receipt by the CCC.

- These terms and conditions together with CCC's Billing and Payment terms and conditions (which are incorporated herein) form the entire agreement between you and WILEY concerning this licensing transaction and (in the absence of fraud) supersedes all prior agreements and representations of the parties, oral or written. This Agreement may not be amended except in writing signed by both parties. This Agreement shall be binding upon and inure to the benefit of the parties' successors, legal representatives, and authorized assigns.

- In the event of any conflict between your obligations established by these terms and conditions and those established by CCC's Billing and Payment terms and conditions, these terms and conditions shall prevail.

- WILEY expressly reserves all rights not specifically granted in the combination of (i) the license details provided by you and accepted in the course of this licensing transaction, (ii) these terms and conditions and (iii) CCC's Billing and Payment terms and conditions.

- This Agreement will be void if the Type of Use, Format, Circulation, or Requestor Type was misrepresented during the licensing process.

- This Agreement shall be governed by and construed in accordance with the laws of the State of New York, USA, without regards to such state's conflict of law rules. Any legal action, suit or proceeding arising out of or relating to these Terms and Conditions or the breach thereof shall be instituted in a court of competent jurisdiction in New York County in the State of New York in the United States of America and each party hereby consents and submits to the personal jurisdiction of such court, waives any objection to venue in such court and consents to service of process by registered or certified mail, return receipt requested, at the last known address of such party.

WILEY OPEN ACCESS TERMS AND CONDITIONS

Wiley Publishes Open Access Articles in fully Open Access Journals and in Subscription journals offering Online Open. Although most of the fully Open Access journals publish open access articles under the terms of the Creative Commons Attribution (CC BY) License only, the subscription journals and a few of the Open Access Journals offer a choice of Creative Commons Licenses. The license type is clearly identified on the article.

The Creative Commons Attribution License

The Creative Commons Attribution License (CC-BY) allows users to copy, distribute and transmit an article, adapt the article and make commercial use of the article. The CC-BY license permits commercial and non-

Creative Commons Attribution Non-Commercial License

The Creative Commons Attribution Non-Commercial (CC-BY-NC)License permits use, distribution and reproduction in any medium, provided the original work is properly cited and is not used for commercial purposes.(see below)

Creative Commons Attribution-Non-Commercial-NoDerivs License

The Creative Commons Attribution Non-Commercial-NoDerivs License (CC-BY-NC-ND) permits use, distribution and reproduction in any medium, provided the original work is properly cited, is not used for commercial purposes and no modifications or adaptations are made. (see below)

Use by commercial "for-profit" organizations

Use of Wiley Open Access articles for commercial, promotional, or marketing purposes requires further explicit permission from Wiley and will be subject to a fee.

Further details can be found on Wiley Online Library
http://olabout.wiley.com/WileyCDA/Section/id-410895.html

Other Terms and Conditions:

v1.10 Last updated September 2015

Questions? customercare@copyright.com or +1-855-239-3415 (toll free in the US) or

+1-978-646-2777.

ChemPubSoc Europe

DOI: 10.1002/slct.201903308

Chemistry SELECT Full Papers

Energy Technology & Environmental Science

A Comprehensive Topological Analysis of a Novel Flavonoid Extracted from Brazilian Cerrado Plants

Marianna C. Silva,* Lóide O. Sallum, Antônio C. S. Menezes, Ademir J. Camargo, and Hamilton B. Napolitano*[a]

Epicatechin is a bioactive compound that has several biological functions, and can be found in a number of Brazilian Cerrado plants. The compound (2R,3R)-2-(3,4-dihydroxyphenyl)-3,4-dihydro-2H-1-benzopyran-3,5,7-triol (EPC) was extracted from Salacia crassifolia and its molecular architecture and supramolecular arrangement were characterized by X-ray diffraction and Hirshfeld Surface. Theoretical calculations such as QTAIM, frontier molecular orbital, MEP and infrared spectra assignments were calculated at M06-2X/6-311++G(d,p) basis set. MEP revealed most positive region around hydrogen atoms of the hydroxyl group. X-ray diffraction and QTAIM results showed that EPC forms a tetramer linked by classical hydrogen bonds O–H···O due to the number of hydroxyl groups available. The crystalline packing and supramolecular arrangement are stabilized by non-classical hydrogen C–H···O and C–H···π interactions.

Introduction

Brazilian flora has great molecular biodiversity, which comes from secondary metabolites found in a number of species present in the six biomes,[1,2] namely the Amazon rainforest, Cerrado, Caatinga, Atlantic forest, Pantanal and Pampas.[3] The cerrado is notable for its extension, as the second largest biome of South America,[4,5] with more than 13,000 species of plants,[1] and because of this diversity various compounds extracted from natural products have strong potential for application.[2] For example, *Salacia crassifolia* has been found in the Cerrado, presenting a number of chemical compounds such as polyphenols.[2] The polyphenolic compounds include various substances, such as epicatechin, which belongs to the flavonoid group.[6] The polyphenols formed in the Cerrado can be explained by the tropical seasonal climatic conditions, with long periods of rain and drought in the region.[2,7] They are present in foods like dark chocolate, apple, orange, and grape,[6,8] and can also be found in several parts of plants, such as the stem of *Metroxylon sagus*, from which isolates have been reported.[8]

The contribution of epicatechin to human health has been studied and reported through *in vitro* and *in vivo* assay,[8] in which positive and promising results against cardiovascular,[8],[9],[10][11] neurodegenerative (Alzheimer's),[6,12] and neurological (anxiety)[12] diseases have been discovered. Furthermore, antitumor,[8] anti-inflammatory,[8] antimicrobial,[8] antioxidant,[9,13] and antibacterial activities[14] have been reported. Biological activities can be influenced by structural conformation and the presence of functional groups; consequently, understanding these structural aspects is important for analyzing the structure–activity relationship in order to support the study of future applications.[15,16]

Considering that the activities of epicatechin may be influenced by the number of hydroxyls and functional groups linked to this molecular structure, this work aims to study the supramolecular architectures and topological studies of (2R,3R)-2-(3,4-dihydroxyphenyl)-3,4-dihydro-2H-1-benzopyran-3,5,7-triol (EPC) by single crystal X-ray diffraction, Hirshfeld surface (HS) analysis and theoretical study at M06-2X/6-311++G(d,p) level of theory. This paper also show frontier molecular orbital (FMO), molecular electrostatic potential (MEP), vibrational assignments and quantum theory of atoms in molecules (QTAIM) for EPC with the purpose of investigating its molecular properties.

Results and discussion

Solid state characterization

The Ortep diagram is shown in Figure 1. The EPC crystal was obtained by extraction and crystallization from dichloromethane/methanol, and it has a pale orange prismatic habit, with molecular weight of 290.26 g.mol^{-1}. The compound was crystallized unto orthorhombic crystal system and non-centrosymmetric space group $P2_12_12_1$ with cell parameters a = 6.71050 Å, b = 13.2880 Å, c = 14.2615 Å, $\alpha=\beta=\gamma=90°$, and four independent molecules per unit cell (Z = 4).

The molecule has an twisted heterocyclic ring (C1–O1 and C8–O1 with bond distances 1.44 Å and 1.38 Å, respectively) due to conjugation effect on C8 atom, regarding eletronic relocation region.[17] The heterocyclic conformation of half-chair is evidenced by the dihedral angles O1–C1–C2–O2 and C9–C3–

[a] Dr. M. C. Silva, Dr. L. O. Sallum, Dr. A. C. S. Menezes, Dr. A. J. Camargo, Dr. H. B. Napolitano
Grupo de Química Teórica e Estrutural de Anápolis, Universidade Estadual de Goiás, Anápolis, GO, Brazil
Tel.: +55 (62) 3328–1192
E-mail: silva.c.marianna@gmail.com
hbnapolitano@gmail.com

Supporting information for this article is available on the WWW under https://doi.org/10.1002/slct.201903308

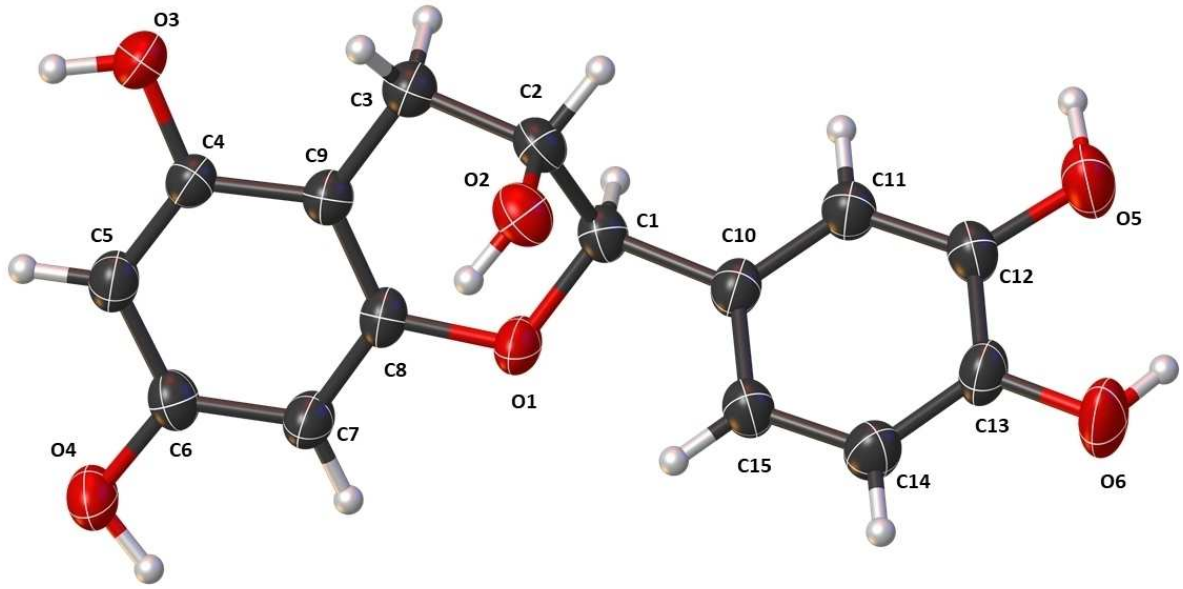

Figure 1. ORTEP representations at 50% probability level with the atomic numbering scheme for EPC. The hydrogen atoms are represented with arbitrary radii.

C2–O2 (62.9° and −77.6°, respectively) as shown in Table 1. Also, the dihedral angle O1–C8–C9–C3 is almost coplanar, and atoms C1 and C2 are out of the mean plane.[18] The molecular structure of EPC has two chiral centers with configuration C1R and C2R, with C1 bonded in an equatorial position and C2 bonded to the hydroxy group at axial position. The atoms C10–C11–C12–C13–C14–C15 and O1–C1–C2–C3–C9–C8 define two independent planes (Figure 2) with torsional angle of 48.74°. Table 1 shows experimental and theoretical selected geometric parameters in good agreement. The observed differences are due to theoretical methods taken into gas phase and not accounting for molecular interactions.

The crystal packing is stabilized by classical interactions type O–H···O and non-classical type C–H···O. The interactions and geometric parameters are represented in Table 2. An intermolecular tetramer involving O6–H6···O4, O4–H4···O3, O3–H3···O2, O2–H2···O6 is observed, increasing in the a and b axis directions, which can be described by the ring $R_4^4(8)$ (Figure 3a). Other intermolecular interactions observed are O5–H5···O1 and C7–H7···O3, which contribute to a repetition zigzag in the a axis direction, forming an infinite chain in $C_1^1(7)$, and intramolecular interaction is composed of atoms O6–H6···O5, which are in the direction of the b axis (Figure 3b). In addition, the compound has intermolecular bifurcated C5–H5A···O5 and C3–H3B···O5 interactions, in the direction of the b axis in infinite chair, described as $C_2^1(7)$ (Figure 3c).

Table 2. Hydrogen bond distances (Å) and angles (°) for EPC.

D – H···A	D – H	H···A	D···A	D – H···A	Symmetry code
O6–H6···O4	0.84	2.07	2.761	140	x, −1 + y, z
O5– H5···O1	1.00	2.25	3.157	151	1/2 + x,3/2-y,1-z
O2–H2···O6	0.89	2.01	2.807	149	-x,1/2 + y,3/2-z
O3–H3···O2	0.87	1.83	2.694	176	1-x,1/2 + y,3/2-z
O4–H4···O3	0.90	2.28	2.963	132	-1 + x, y, z
O6–H6···O5	0.84	2.30	2.727	112	x, y, z
C5–H5 A···O5	1.01	2.68	3.551	143	x, −1 + y, z
C3–H3B···O5	0.98	2.63	3.584	162	1/2 + x,1.5-y,1-z
C7–H7···O3	0.98	2.82	3.291	110	1 + x, y, z

In order to compare the structure of EPC with other flavonoids, mainly with regard to the intramolecular interactions on site O6–H6…O5, three structures were selected from CCDC: 2-(3,4-dihydroxyphenyl)-7-hydroxy-8-methoxy-2,3-dihydro-4H-chromen-4-one (FVD I, code 935091),[19] 4-((2-(3,4-dihydroxyphenyl)-5,7-dihydroxy-4-oxo-3,4-dihydro-2H-chromen-3-yl)oxy)-4-oxobutanoic acid (FVD II, code 1487557),[20] and 2-(3,4-dihydroxyphenyl)-5-hydroxy-7-methoxy-2,3-dihydro-4H-chromen-4-one (FVD III, code 778613).[21] From the common flavonoid moiety, search in CCDC database used unsolvated

Table 1. Relevant experimental and theoretical geometric parameter for EPC. Bond distances (Å), angles (°) and torsion angles (°).

	Experimental	Theoretical		Experimental	Theoretical
O1–C1	1.445 (4)	1.428	O1–C1–C2–O2	62.9 (3)	58.2
C1–C2	1.527 (5)	1.538	C8–O1–C1–C2	44.5 (3)	51.2
C7–C6	1.385 (4)	1.385	C9–C3–C2–C1	46.5 (3)	45.7
C3–C2–C1	109.9 (3)	108.5	C15–C10–C1–C2	91.0 (3)	91.8
C14–C13–C12	120.1 (3)	119.2	O1–C1–C2–C3	-61.5 (3)	-65.3
C9–C3–C2–O2	-77.6 (3)	-76.9	C9–C4–O3–H3	-163 (3)	-177.8

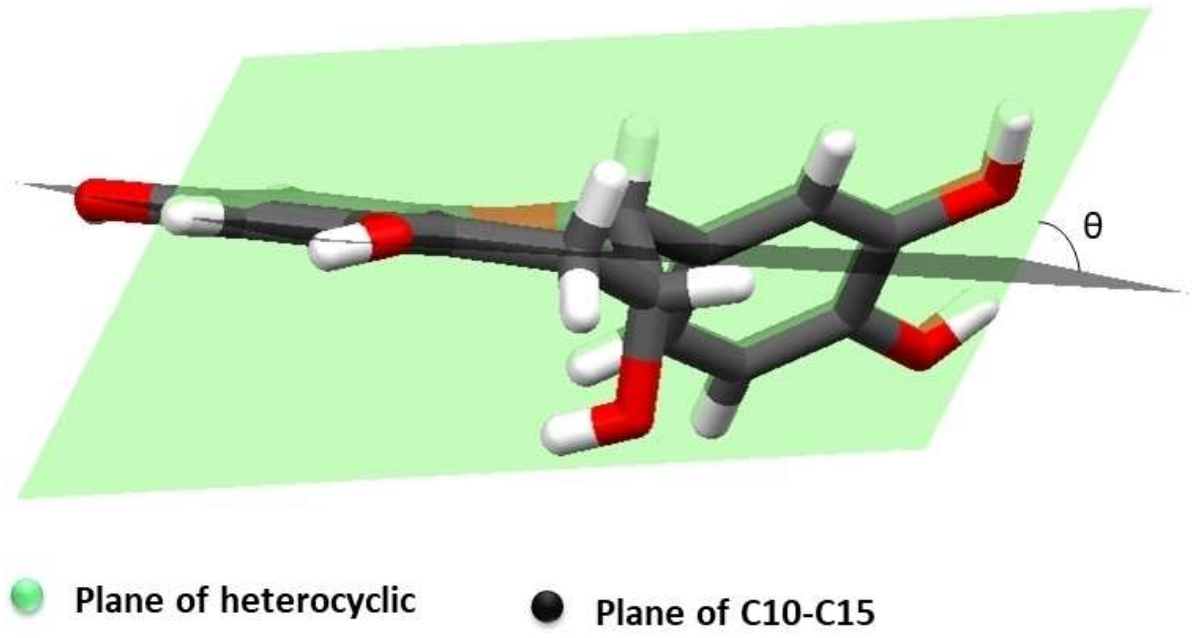

Figure 2. Representation of dihedral angles formed by planes of aromatic rings: $\theta = 48.74°$

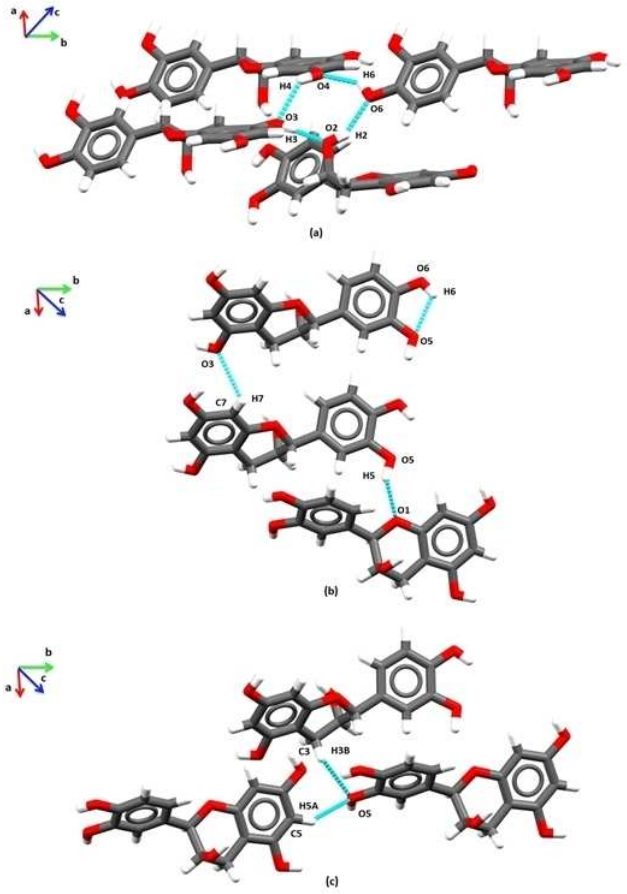

Figure 3. Intermolecular and intramolecular interactions of EPC hydrogen bond (a) O6–H6···O4, O4–H4···O3, O3–H3···O2 and O2–H2···O6; (b) O5–H5···O1, C7–H7···O3 and O6–H6···O5; (c) C5–H5 A···O5 and C3–H3B···O5.

structures. Flavonoids molecular skeleton consists of fifteen carbon atoms formed by the union three rings, with two benzene rings connected by a pyran ring.[16] They have a great structural diversity explained by hydroxylation, methoxylation, glycosylation, sulphation and acylation patterns of ring substitutions.[16] Compound FVD I is almost planar (2.49° difference between planes) and has the intramolecular interaction on site O6–H6···O5 [D···A = 2.673 Å; D–H···A = 115°] which is in the direction of the b axis. Structure FDV II has an angle of 85.80° from one plane to the other and shows intramolecular interactions on site O6–H6···O5 [D···A = 2.668 Å; D–H···A = 114°] in the direction of b axis. Structure FDV III has two independent molecules in the asymmetric unit, with only one conformer displaying an intramolecular interaction on site O6–H6···O5 [D···A = 2.684 Å; D – H···A = 112°] in a zigzag at a axis direction.

Topological analysis

The HS is used to confirm the intermolecular interactions in crystal packing by topological analysis, through the Van der Waals radius. The *dnorm* HS (ranging from −0.511 to 1.470 Å) is shown in Figure 4. Different levels of color intensity in HS indicate the different intensity of interactions, where blue indicates weak interactions, and red indicates strong interactions. The red dots (1), (3), (5) and (10) correspond to *de* contacts, indicating where the molecules act as acceptors of O2–H2···O6, O3–H3···O2, O5–H5···O1, and O4–H4···O3 respectively. The red dots (2), (4), (6) and (9) refer to *di* contacts, indicating where the molecules act as donors of O2–H2···O6, O3–H3···O4, O5–H5···O1, and O6–H6···O4 respectively. The pale red dots (7), (8) and (11) indicate weak interactions (due to the large distance between donor and acceptor) and act as

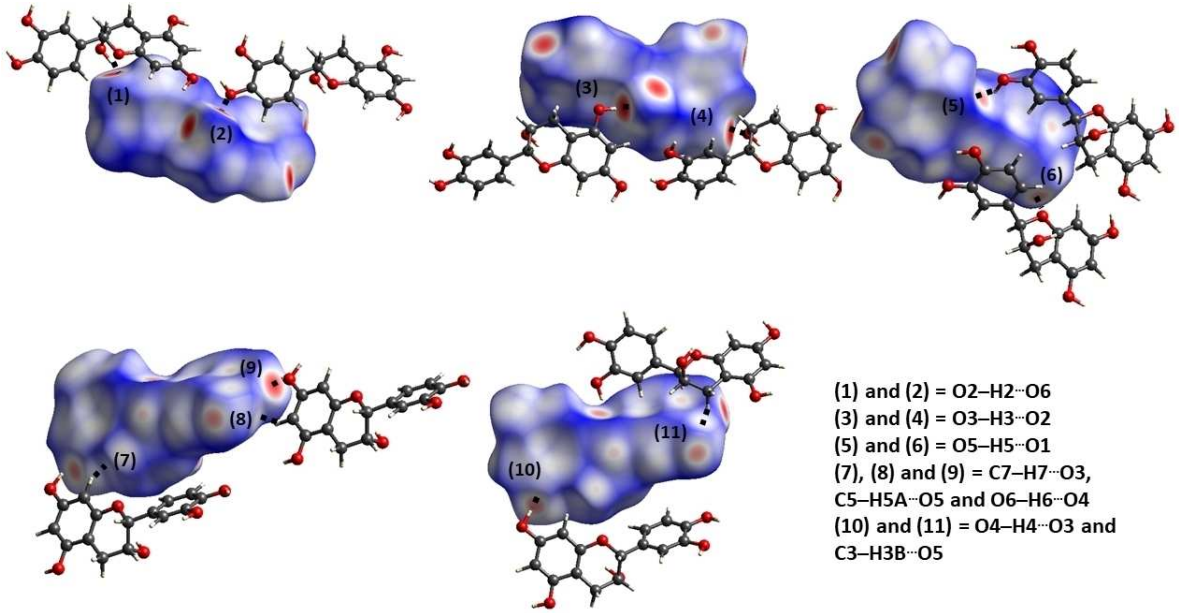

Figure 4. Hirshfeld surface indicates intermolecular interactions of EPC. Interactions are represented by dotted black lines.

acceptors for C7–H7···O3, C5–H5 A···O5 and C3–H3B···O5, respectively. This analysis assists in the description of the interactions which are the most dominant among molecules.

The hydrophobic interactions (C–H···π and π ···π) can be described throughout shape index, which is used to identify complementary (red) and bumps (blue) on final analysis of the intermolecular contacts (Figure 5). The interactions are indicated by significant depressions on the aromatic ring and red regions of the concave. EPC has additional stability through C–H···π interactions, involving Cg1 (gravity center of the aromatic ring, formed by atoms C10, C11, C12, C13, C14, C15), with C1–H1···Cg1 interactions (H1···Cg1 = 3.286 Å, D–H···A = 146.41) and C11–H11···Cg1 (H11···Cg1 = 2.837 Å, D–H···A = 147.70) as shown in Figure 5a and 5b respectively, and also by C –H···π interaction, involving Cg2 (gravity center of the aromatic ring, formed by atoms C4, C5, C6, C7, C8, C9) with C14–H14···Cg2 interaction (H14···Cg2 = 2.651 Å, D–H···A = 128.57), shown in Figure 5c.

The fingerprint is the graph of di and de plotted two-dimensionally, obtaining the complete maps of contacts present in molecules with their respective percentages. The fingerprint of EPC is shown in Figure 6. As it is an organic molecule, it has a higher percentage of H–H contacts (35.90%), with the coordinates di = de = 1.4. The O–H contact has a percentage of 33.30% of the total present in the molecule, indicating C–H···O and O–H···O interactions. In addition, the C–H contact (25.3%) also represents the C–H··· π interaction.

The QTAIM is an approach to analyze different intra and intermolecular interactions based on the electron density of molecule system.[22] The wavefunction was obtained at M06-2X/6-311 + + G(d,p) level of theory using the G09 program. The hydrogen bond is characterized by having an important role in the chemical, physical and biochemical processes. The Multiwfn program (version 3.7)[23] was used for the QTAIM analysis. These interactions can be described and visualized with the help of a molecular graph, which appears the crucial bond path linking the proton-acceptor atoms, as shown in Figure 7 and Table 3.

The EPC is formed by eleven intermolecular interactions and one intramolecular O_6–H_6···O_5 interaction. The stationary point between these hydrogen donors atoms and the acceptors atoms is described by bond critical point (BCP)[24] as a confirmation of the existence of hydrogen bonding interactions. The positive Laplacian and the negative total energy density E(r) for O_2–H_2···O_6, O_6–H_6···O_4, O_4–H_4···O_3, O_3–H_3···O_2, O_5–H_5···O_1, O_6–H_6···O_5, C_5–H_{5A}···O_5, C_{14}–H_{14}···π, C_{11}–H_{11}···π, C_1–H_1···π and C_3–H_{3B}···O_5 are observed for partially covalent interactions,[22] while the positive Laplacian and the total energy density E(r) positive for C_7–H_7···O_3 is observed for closed-shell systems (the depletion of electron charge within the atom-atom region) like hydrophobic and hydrogen bonds.

The hydrogen bond energy (E_{HB}) is the energy obtained from the interaction energy. According to Espinosa-Mollins-Lecomte[25] the electron density at the BCP permits the correlation of E_{HB} to the potential energy of the electrons V (r_{bcp}), as shown in Equation 1:

$$E_{HB} = \frac{1}{2} V(r_{bcp}) \quad (1)$$

The hydrogen-bonding interactions based on energy[26] is weak, medium and strong when hydrogen bonds have |EHb| < 12 kcal mol^{-1}, 12 kcal mol $^{-1}$ < |EHb| < 24 kcal mol^{-1} and |EHb| > 24 kcal mol^{-1}, respectively. Three classical hydrogen homonuclear interactions (O_2–H_2···O_6, O_3–H_3···O_2 and O_6–H_6···O_5) were classified as strong in strength. The O_6–H_6···O_4 and O_5–H_5···O_1 intermolecular interactions were classified as medium in

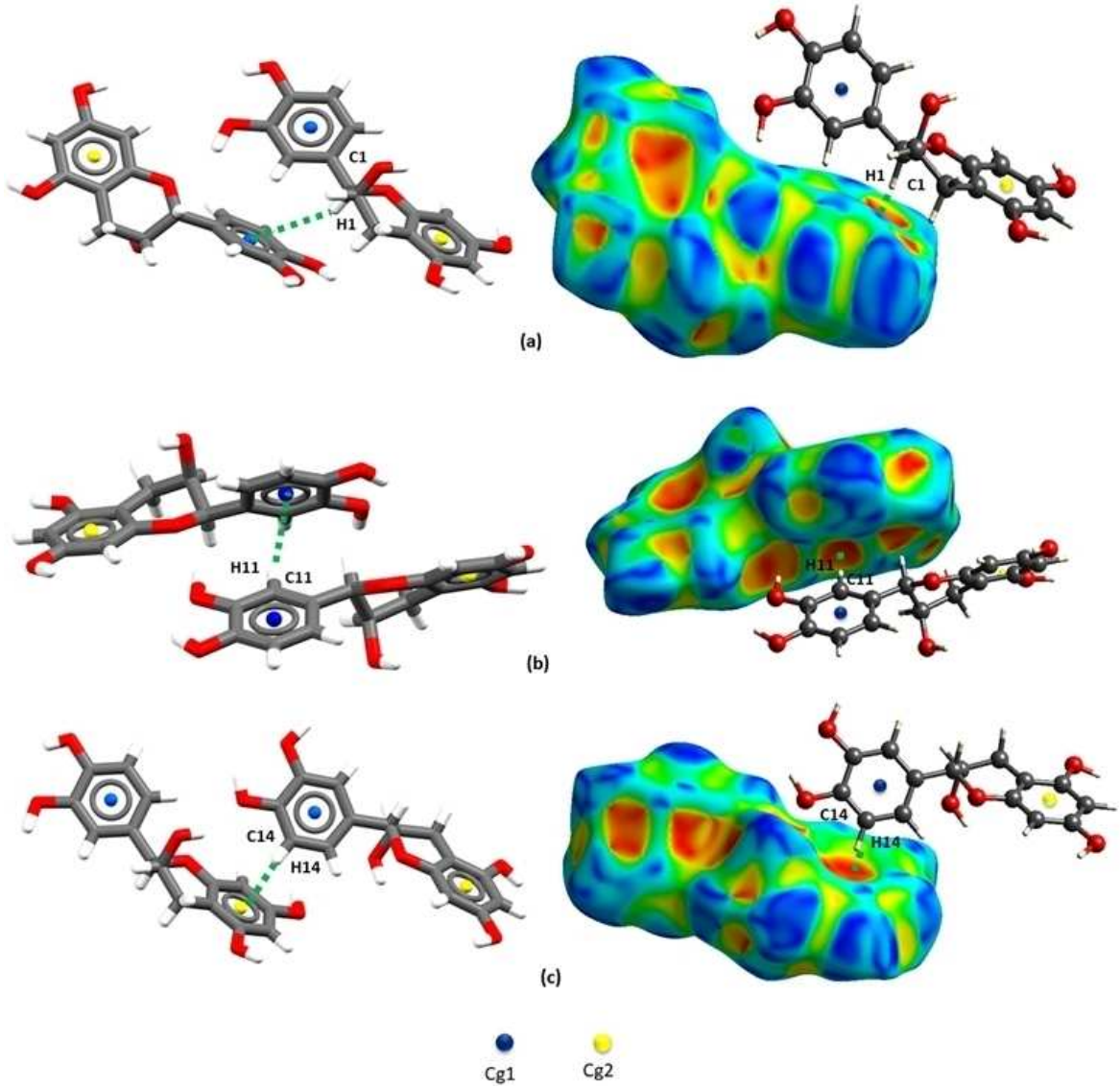

Figure 5. Hirshfeld surface shape index of EPC evidencing C–H···π interactions, corresponding to (a) C1–H1···Cg1, (b) C11–H11···Cg1 and (c) C14–H14···Cg2.

Table 3. Topological parameters of EPC describing intermolecular interactions (electron density at BCP (ρ(r)), Laplacian ($\nabla^2\rho(r)$), the potential electron energy density (V(r)), the kinetic electron energy density (G(r)), the total electron energy density (E(r)), and bond energy (E_{HB}).

BCP	Interaction	ρ(**r**)[a]	$\nabla^2\rho(\mathbf{r})$[a]	V(**r**)[a]	G(**r**)[a]	E(**r**)[a]	E_{Hb}[b]
1	O2–H2···O6	0.07771	0.29396	-0.08635	0.07992	-0.00643	-27.092
2	O6–H6···O4	0.07592	0.11424	-0.07325	0.05090	-0.02234	-22.982
3	O4–H4···O3	0.04511	0.05143	-0.02840	0.02063	-0.00777	-8.9106
4	O3–H3···O2	0.11163	0.51278	-0.16811	0.14815	-0.01995	-52.745
5	C5–H5 A···O5	0.02926	0.03241	-0.01423	0.01116	-0.00306	-4.4647
6	C7–H7···O3	0.04062	0.08257	-0.01798	0.01931	0.00133	-5.6413
7	C14–H14···π	0.04356	0.04663	-0.02008	0.01587	-0.04213	-6.3001
8	O5–H5···O1	0.08566	0.10839	-0.06334	0.04522	-0.01825	-19.873
9	C11–H11···π	0.04425	0.04838	-0.01617	0.01413	-0.00203	-5.0734
10	C1–H1···π	0.05463	0.06336	-0.02603	0.02093	-0.00509	-8.1670
11	C3–H3B···O5	0.03380	0.04877	-0.01353	0.01286	-0.00066	-4.2450
12[c]	O6–H6···O5	0.10638	0.21080	-0.09308	0.07289	-0.02019	-29.204

(a) = atomic units; (b) = kcal/mol; (c) = intramolecular interaction.

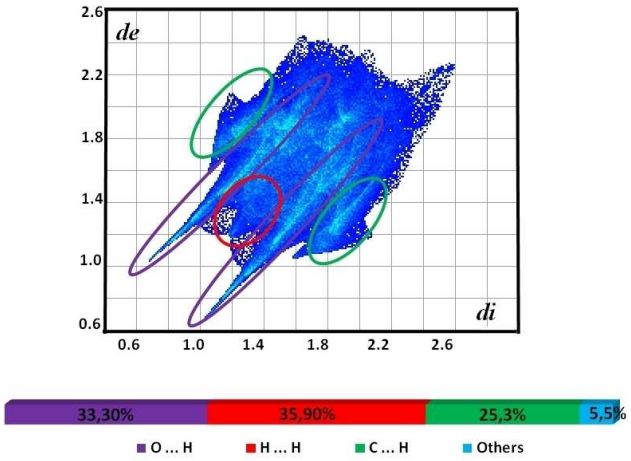

Figure 6. Quantification of different types of contacts and the fingerprint of EPC established.

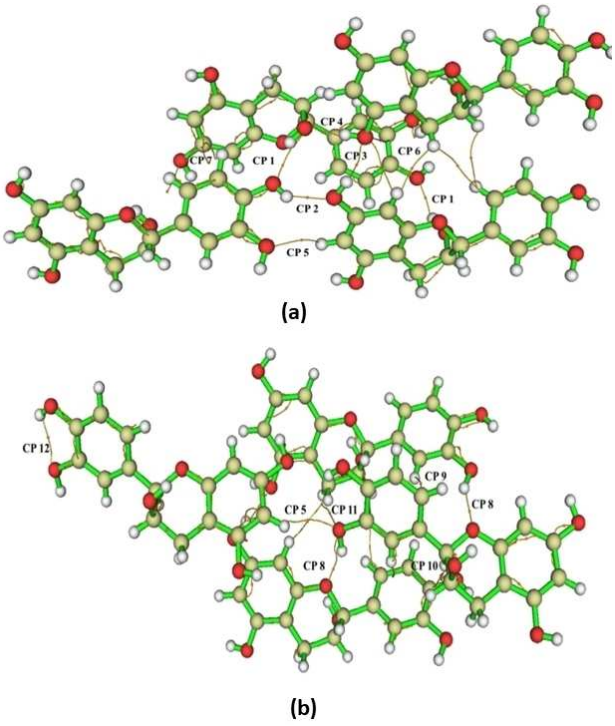

Figure 7. The molecular graphs showing the BCPs as yellow points.

strength, although the others are classified as weak in strength. The supramolecular arrangement is stabilized by hydrogen classical bonds O–H···O and hydrogen non-classical bonds C–H···O. In addition, the hydrophobic interaction C–H···π contributes for this structural stability. The highest E_{HB} value for O_3–H_3···O_2 is attributed to the close distance 2.694 Å donor-acceptor and to the direction 176° for this interaction. In contrast, the weaker character of C_7–H_7···O_3 is due to this electron sharing by the O3 and to no direction (110°).

Frontier molecular orbitals

The root of the mean squared (RMS) value, predicted using Mercury, which compared calculated and experimental geometries by structural overlapping, was 0.00934 for EPC as shown in Figure 8. The overlay shows a good agreement of geometric parameters. The aromatic ring (Cg2) exhibits an experimental dihedral twist C9–C4–O3–H3 of −163.0° that differ by theoretical dihedral angles, which value is −177.8° (Table 1).

The FMO, shown in Figure 9, obtained from NBO analysis for EPC were carried out at M06-2X/6-311++G(d,p) level of theory. The canonical orbitals resulting from the electronic structure are transformed into the most localized orbitals from one-center (lone pair) and two-centers (bonds). At first, canonical orbitals are transformed into natural atomic orbitals (NAOs). The NAOs are then transformed into hybrid natural orbitals (NHOs) and then into natural bond orbitals (NBOs). The advantage of NBO orbitals is that they closely resemble the structures of Lewis, which correspond very much to the chemists' intuition. The NBO analysis bond-antibond interactions are taken into consideration by filled (donor) Lewis base and empty (acceptor) Lewis acid. The HOMO as the electron donor is localized on the π bonding, which is characteristic of the nucleophilic region. The HOMO result is negative (-180.85 kcal/mol) and appears as a π bonding orbital. The LUMO orbital is a π antibonding orbital localized on the C11=C12 nearby the hydroxyl group (O5-H5). The LUMO for EPC is positive (29.81 kcal/mol). This orbital analysis indicates that this molecule is chemically stable.

The NBO analysis was performed at the M06-2X/6-311+G(d,p) (the non-hydrogen atoms were taken from the crystallographic data while the hydrogens atoms were optimized) level of theory. The hyperconjugative interaction energy can be estimated from the second-order perturbation,[27] as described in Equation 2:

$$E(2) = -n_\sigma \frac{\langle \sigma | F | \sigma \rangle^2}{\varepsilon_\sigma^* - \varepsilon_\sigma} = -n_\sigma \frac{F_{ij}^2}{\Delta E'} \quad (2)$$

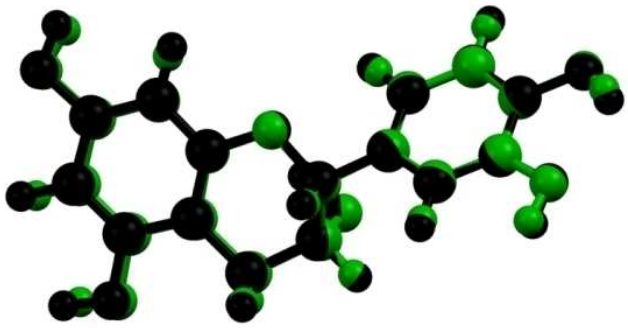

Figure 8. Overlapping of M06-2X/6-311++G(d,p) level of theory (black) and X-ray (green) structures from EPC.

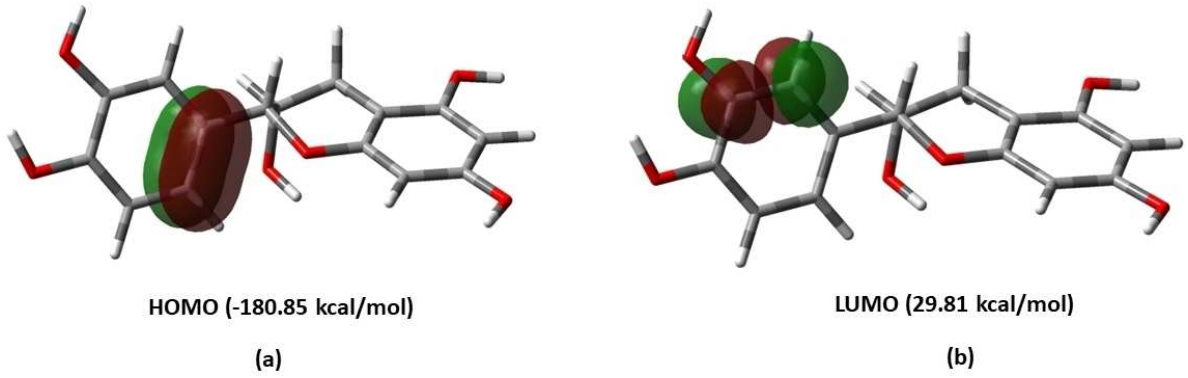

Figure 9. Frontier molecular orbitals for EPC (a) the HOMO bonding orbital and (b) the LUMO antibonding orbital derived from NBO analysis at M06-2X/6-311++G(d,p) level of theory with the isovalue of 0.05 atomic units.

where $\langle\sigma|F|\sigma\rangle^2$ is the Fock matrix element between the i and j NBO orbitals. ε_{σ}^{*} and ε_{σ} are the energies of σ and σ^{*} NBO's and n_{σ} is the population of the donor σ orbital. NBO analysis provides a method for studying hyperconjugative interaction in molecular system. The increase the $E(2)$ value, more intensive is the interaction between electrons donor and acceptor, respectively. The results of intramolecular interactions are presented in Table 4.

The intramolecular hyperconjugative interaction of C–C to the anti C–C bond of the aromatic rings suggest to stabilization of parts of the rings. The intramolecular interactions energy, related to the resonance in the molecule, is electron donating from the LP (2) O1, LP (2) O4, LP (2) O3, LP (2) O6 and LP (2) O5 to the antibonding acceptor BD*(2) C8 – C9, BD*(2) C7 – C6, BD*(2) C5 – C4, BD*(2) C14 – C13 and BD*(2) C11 – C12. The most interaction energy, related to the aromatic ring, is electron donating from the BD*(2) C11 – C12, BD*(2) C11 – C12 and BD*(2) C14 – C13 to the acceptor BD*(2) C10 – C15, BD*(2) C14 – C13 and BD*(2) C10 – C15 leading to high stabilization energy.

Table 4. The major intramolecular interactions NBO analysis using DFT wavefunctions for EPC.

Donor (i)	Acceptor (j)	E(2)[a]	E(j) – E(i)[b,c]	F(i,j)[b,d]
BD (2) C7 – C6	BD*(2) C8 – C9	34.85	0.36	0.103
BD (2) C10 – C15	BD*(2) C11 – C12	28.54	0.34	0.089
BD (2) C10 – C15	BD*(2) C14 – C13	27.44	0.35	0.088
BD (2) C8 – C9	BD*(2) C5 – C4	35.19	0.36	0.102
BD (2) C14 – C13	BD*(2) C10 – C15	29.25	0.37	0.093
BD (2) C14 – C13	BD*(2) C11 – C12	28.95	0.35	0.091
BD (2) C5 – C4	BD*(2) C7 – C6	35.67	0.36	0.104
LP[e] (2) O1	BD*(2) C8 – C9	30.47	0.46	0.113
LP (2) O4	BD*(2) C7 – C6	33.26	0.46	0.119
LP (2) O3	BD*(2) C5 – C4	33.24	0.46	0.119
LP (2) O6	BD*(2) C14 – C13	31.46	0.45	0.114
LP (2) O5	BD*(2) C11 – C12	27.23	0.47	0.109
BD*[f](2) C11 – C12	BD*(2) C10 – C15	181.82	0.02	0.096
BD*(2) C11 – C12	BD*(2) C14 – C13	363.09	0.01	0.096
BD*(2) C14 – C13	BD*(2) C10 – C15	352.14	0.01	0.096

(a) kcal/mol; (b) atomic units; (c) Energy difference between donor and acceptor i and j NBO orbitals; (d) F(i,j) is the Fock matrix element between i and j NBO orbitals; (e) LP(n)A is a valence lone pair orbital (n) on A atom; (f) (*) denotes antibonding.

Electrostatic potential surface

The MEP is an important physicochemical tool that gives information about chemical reactivity of the molecular systems.[28–30] The electrostatic potential can be calculated through Equation 3, as follows:

$$V(r)=\sum_{\alpha}\frac{Z_{\alpha}}{|r-R_{\alpha}|}-\int\frac{\rho(r')}{|r-r'|}dr' \quad (3)$$

where $V(r)$ is the potential energy by a positive unit charge at **r**; Z_{α} is the nuclear charge α located at $\mathbf{R}_{\alpha}$, and $\rho(r')$ is the electron density at point r'. To understand the MEP done for EPC we used the tridimensional MEP representation (Figure 10), where yellow-orange specifies the most negative region (moderate attraction) and is localized on the oxygen atom (O2) of the hydroxyl group of heterocyclic, with value about −45.80 kcal/mol. On the other hand, the blue region specified the most positive potential (strongest repulsion) and the isovalue potential energy of about 32.63 kcal/mol is around the

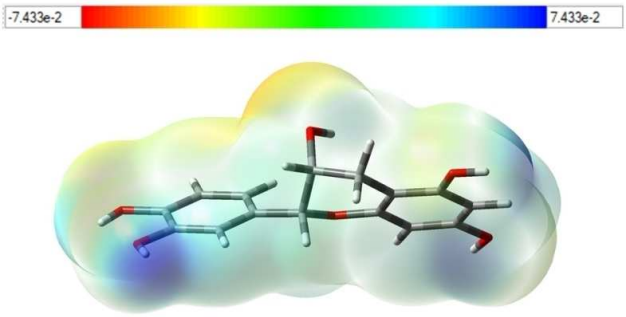

Figure 10. The molecular electrostatic potential surface mapped for EPC (a) the yellow-orange colored region is rich in electron, and (b) the blue-colored region is electron depleted. The density isovalue of 4.0 x 10^{-4} electrons/bohr^3 was used to generate the molecular electrostatic potential surfaces.

hydrogen atom (H5). In this region, the hydroxyl group at the para position with the aromatic ring is responsible for the electron withdrawing effect. These results inform where EPC interacts intermolecularly and identify the electrophilic and nucleophilic attacks.

Vibrational assignments

The principal IR absorptions bands are in Table 5 and the experimental and calculated IR-FT spectra are shown in Figure 11. These values in vibrational frequencies were scaled by 0.943[31] for the results obtained at M06-2X/6-311++G(d,p) level of theory. Thus, the theoretical measurements obtained in the gas phase, the hydroxyl group absorb in the 3706–3647 cm^{-1}, while the experimental measurements, in which the decrease of the vibration frequency value occurs due to the molecular hydrogen interaction, absorbs in 3508–3277 cm^{-1}.[32] Experimentally, the aromatic appears in 1516 cm^{-1} and 1463 cm^{-1}, while for the theoretical measurements it appears in 1601 cm^{-1}, 1500 cm^{-1} and 1480 cm^{-1}. The C–O (ether) stretch appears at 1258 cm^{-1} and 1050 cm^{-1} for experimental measurements, while the theoretical measurements appear at 1264 cm^{-1} and 1051 cm^{-1}. The vibrational band of stretching mode C-H_{Het}, which is related to heterocyclic ring, has value of 2852 cm^{-1}, while in DFT, this band is 2863 cm^{-1}. The IR spectra stretching mode of the CH_2 group is in the range of 2920–2888 cm^{-1}, while the computed wavenumbers are in the range of 2935–2873 cm^{-1}. The experimental wavenumbers of stretching vibration C-H_{Ar} appears at the range of 2954–2927 cm^{-1}, while the computed wavenumbers are in the range of 3011–2966 cm^{-1}.

Table 5. Theoretical and experimental vibrational assignments for EPC.

Vibrational mode	Exp. Freq[a].	Scaled Freq[a,b].
ν OH	3508-3277	3706-3647
ν C=C_{Ar}[c]	1516;1463	1601; 1500; 1480
ν C-O	1258; 1050	1264;1051
ν_{sym} C-H_{Het}[d]	2852	2863
ν_{sym} CH_2	2920-2888	2935-2873
ν_{sym} C-H_{Ar}[c]	2954-2927	3011-2966

ν = stretching; a) cm^{-1}; b) Scale factor 0.943; c) Ar = aromatic ring; d) Het = heterocyclic

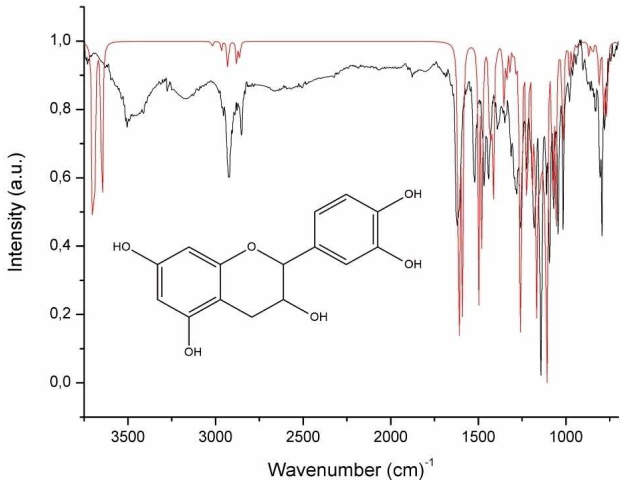

Figure 11. The experimental (black) and theoretical (red) overlapped IR-FT spectrum of EPC.

Conclusions

In this paper, the extraction route, crystallization and comprehensive characterization of the compound $C_{15}H_{14}O_6$ from *Salacia crassifolia* were described. The planarity of the molecule and the formation of a half chair in one of the rings were observed on molecule architecture. The tetrameric supramolecular arrangement occurs through the classical O–H···O and non-classical C–H···O and C–H···π interactions, which were all confirmed through topological analysis. Additionally, theoretical calculation (FMO, HOMO and LUMO) confirmed chemical stability and observed experimental molecular structure. MEP is consistent with the susceptible nucleophilic attack around hydrogen atoms of hydroxyl groups. The theoretical IR absorptions bands are consistent with the experimental IR-FT bands. Finally, QTAIM successfully analyzed the observed topology through BCP associated with inter and intramolecular interaction, which are consistent with the crystalline supramolecular arrangement. A comprehensive topological analysis of a novel EPC from Brazilian Cerrado constitutes a new insight to understand the biodiversity of polyphenols from Cerrado Bioma.

Supporting Information Summary

The details of experimental and computational procedures, including crystal data and structure refinement are provided in the Supporting Information.

Acknowledgements

The authors are grateful to the Coordenação de Aperfeiçoamento de Pessoal de Nível Superior (CAPES, Finance Code 001) and the Fundação de Amparo à Pesquisa do Estado de Goiás (FAPEG) for financial support. Also, the authors are grateful to the High-Performance Computing Center of the Universidade Estadual de Goiás (UEG).

Conflict of Interest

The authors declare no conflict of interest.

Keywords: Epicatechin · Quantum Chemistry · X-ray diffraction

[1] L. M. O. R. Antiqueira, *J. Plant Sci.* **2013**, *1*, 1–5.
[2] E. F. L. C. Bailão, I. A. Devilla, E. C. da Conceição, L. L. Borges, *Int. J. Mol. Sci.* **2015**, *16*, 23760–23783.
[3] M. Valli, H. M. Russo, V. da S. Bolzani, *An. Acad. Bras. Cienc.* **2018**, *90*, 763–778.
[4] L. M. Coutinho, *Acta Botânica Bras.* **2006**, *20*, 13–23.

[5] E. E. Sano, R. Rosa, J. L. S. Brito, L. G. Ferreira, *Environ. Monit. Assess.* **2010**, *166*, 113–124.
[6] H. Schroeter, P. Bahia, J. P. E. Spencer, O. Sheppard, M. Rattray, E. Cadenas, C. Rice-Evans, R. J. Williams, *J. Neurochem.* **2007**, *101*, 1596–1606.
[7] S. M. Fank-de-Carvalho, N. S. Somavilla, Báo, M. S. Marchioretto, S. Nair, *Biodivers. Ecosyst. - Link. Struct. Funct.* **2015**, p. 407, DOI 10.5772/59066.
[8] M. Prakash, B. V. Basavaraj, K. N. C. Murthy, *J. Funct. Foods.* **2019**, *52*, 14–24.
[9] C. G. Fraga, P. I. Oteiza, M. Galleano, *Mol. Aspects Med.* **2018**, *61*, 31–40.
[10] J. I. Dower, J. M. Geleijnse, L. Gijsbers, P. L. Zock, D. Kromhout, P. C. Hollman, *Am. J. Clin. Nutr.* **2015**, 914–921.
[11] H. Schroeter, C. Heiss, J. Balzer, P. Kleinbongard, C. L. Keen, N. K. Hollenberg, H. Sies, C. Kwik-Uribe, H. H. Schmitz, M. Kelm, *Proc. Mont. Acad. Sci.* **2006**, *103*, 1024–1029.
[12] T. P. Stringer, D. Guerrieri, C. Vivar, H. Van Praag, *Trans. Mo. Acad. Sci.* **2015**, *5*, e493-9.
[13] M. B. Engler, M. M. Engler, C. Y. Chen, M. J. Malloy, A. Browne, E. Y. Chiu, H. Kwak, P. Milbury, S. M. Paul, J. Blumberg, M. L. Mietus-Snyder, *J. Am. Coll. Nutr.* **2004**, *23*, 197–204.
[14] E. Xia, G. Deng, Y. Guo, H. Li, *Int. J. Mol. Sci.* **2010**, *11*, 622–646.
[15] S. Gao, *Sci. J.* **2013**, *2013*, 1–20.
[16] J. de C. Peixoto, B. J. Neves, F. G. Vasconcelos, H. B. Napolitano, M. G. da S. Barbalho, S. D. e Silva, L. P. Rosseto, *Molecules* **2019**, *24*, 2891.
[17] A. L. Spek, B. Kojic-Prodic, R. P. Labadie, *Acta Crystallogr.* **1984**, *40*, 2068–2071.
[18] F. R. Fronczek, G. Gannuch, W. L. Mattice, F. L. Tobiason, J. L. Broeker, R. W. Hemingway, *J. Chem. Soc. Perkin Trans. 2*, **1984**, *10*, 1611–1616.
[19] Y. Okada, M. Okita, Y. Murai, Y. Okano, M. Nomura, *Nat. Prod. Res.* **2014**, *28*, 201–204.
[20] N. V. Mamontova, E. I. Chernyak, E. V. Amosov, Y. V. Gatilov, V. I. Vinogradova, S. F. Aripova, S. V. Morozov, I. A. Grigor'ev, *Chem. Nat. Compd.* **2017**, *53*, 1045–1051.
[21] S. A. Liebman, P. F. Donovan, S. D. Koch, *J. Org. Chem.* **1962**, *27*, 4636–4638.
[22] S. J. Grabowski, *Chem. Rev.* **2011**, *111*, 2597–2625.
[23] T. Lu, F. Chen, *J. Comput. Chem.* **2012**, *33*, 580–592.
[24] C. F. Matta, R. J. Boyd, *The Quantum Theory of Atoms in Molecules: From Solid State to DNA and Drug Design*, **2007**. Axel Becke Foreword. Weinheim: Wiley-VCH, p. 453.
[25] E. Espinosa, E. Molins, C. Lecomte, *Chem. Phys. Lett.* **1998**, *285*, 170–173.
[26] I. Rozas, I. Alkorta, J. Elguero, *J. Am. Chem. Soc.* **2000**, *122*, 11154–11161.
[27] S. A. Siddiqui, A. Dwivedi, N. Misra, N. Sundaraganesan, *J. Mol. Struct.* **2007**, *847*, 101–102.
[28] P. Politzer, D. G. Truhlar. *Chemical Applications of Atomic and Molecular Electrostatic Potentials Reactivity, Structure, Scattering, and Energetics of Organic, Inorganic, and Biological Systems.* **1981**. First Edition. ed. LLC Springer Science + Business Media. New York, p. 7.
[29] Shweta, E. Khan, P. Tandon, R. Maurya, P. Kumar, *J. Mol. Struct.* **2019**, *1183*, 100–106.
[30] Shweta, E. Khan, P. Prajapati, P. Tandon, P. Bharti, P. Kumar, R. Maurya, *J. Mol. Struct.* **2019**, *1175*, 28–38.
[31] H. Yin, X. Kong, *J. Am. Soc. Mass Spectrom.* **2015**, *26*, 1455–1461.
[32] D. L. Pavia, G. M. Lampman, G. S. Kriz, J. A. Vyvyan. *Introduction to Spectroscopy.* **2015**. 5th Edition. Mason, Ohio: Cengage Learning, p. 14.

Submitted: September 3, 2019
Accepted: December 4, 2019

Anexo II

Artigo científico publicado no ***Journal of Molecular Structure*** (2021), 129743.

DOI: https://doi.org/10.1016/j.molstruc.2020.129743

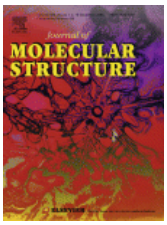

Comparative Conformational Study of a New Terpenoid-like Chalcone

Author:
Marianna C. Silva,Vitor S. Duarte,Jean M.F. Custodio,Jaqueline E. Queiroz,Gilberto L.B. de Aquino,Allen G. Oliver,Hamilton B. Napolitano

Publication: Journal of Molecular Structure

Publisher: Elsevier

Date: 15 March 2021

Journal Author Rights

Please note that, as the author of this Elsevier article, you retain the right to include it in a thesis or dissertation, provided it is not published commercially. Permission is not required, but please ensure that you reference the journal as the original source. For more information on this and on your other retained rights, please visit: https://www.elsevier.com/about/our-business/policies/copyright#Author-rights

BACK CLOSE WINDOW

Journal of Molecular Structure 1228 (2021) 129743

Contents lists available at ScienceDirect

Journal of Molecular Structure

journal homepage: www.elsevier.com/locate/molstr

Comparative Conformational Study of a New Terpenoid-like Chalcone

Marianna C. Silva[a,*], Vitor S. Duarte[a,b], Jean M.F. Custodio[c], Jaqueline E. Queiroz[a], Gilberto L.B. de Aquino[a], Allen G. Oliver[c], Hamilton B. Napolitano[a,*]

[a] Grupo de Química Teórica e Estrutural de Anápolis, Universidade Estadual de Goiás, Anápolis, GO, Brazil
[b] Centro de Pesquisa e Eficiência Energética, CAOA Montadora de Veículos LTDA, Anápolis, GO, Brazil
[c] Department of Chemistry and Biochemistry, University of Notre Dame, Notre Dame, IN, USA

ARTICLE INFO

Article history:
Received 15 September 2020
Revised 3 December 2020
Accepted 7 December 2020
Available online 10 December 2020

Keywords:
X-ray diffraction
Hirshfeld surfaces, **f**rontier molecular orbital

ABSTRACT

Chalcones constitute an important class of flavonoids, which are naturally or synthetically obtained with relevant biological activities such as anti-inflammatory, antioxidant, antileishmanial, antitubercular, anticancer, anti-HIV, antibacterial, antimalarial, antituberculosis, and antiulcer. Conformational differences in these compounds influence their physical-chemistry properties, and the comparative structural analysis is relevant to describe changes in their properties. In this way, we aim to evaluate the conformational changes of three (1E,4E)-1-(4-nitrophenyl)-5-(2,6,6-trimethylcyclohex-2-en-1-yl)penta-1,4-dien-3-one (CHL) crystal structure polymorphs. In addition, Hirshfeld surfaces and theoretical calculations were used to analyze intermolecular interactions responsible for the supramolecular arrangement and molecular stability. The molecular packing of these terpenoid-like chalcones is stabilized by semi-classical C–H···O interactions, and hydrophobic C–H•••π interactions. The HOMO-LUMO gap confirmed the order of kinetic stability in the gas phase CHL-m_1 > CHL-o > CHL-m_2 showing the difference that polymorphism can cause; these differences can affect the properties of the compound and thus influence its applications.

1. Introduction

Chalcones belong to the flavonoid class of compounds and are composed of an aromatic ketone. They are bio-precursor agents of flavonoids and isoflavonoids. Its basic structure, 1,3-diphenyl-2-propen-1-one, consists of a conjugated three-carbon α,β-unsaturated carbonyl system (which makes the compound biologically active) linking two aromatic rings [1,2]. They can be obtained through the isolation of natural products, found in greater abundance in plants of the Asteraceae, Moraceae, Fabaceaee, and Aristolochiaceae families [1,3,4], and by synthetic routes, such as the Aldol condensation reaction, the Suzuki reaction, the Heck reaction, and the Claisen-Schmidt reaction (the most classic, being performed in high-alkaline medium or using a Lewis acid) [2,5].

Chalcones and their derivatives have several biological activities such as anti-inflammatory [6–8], antioxidant [9,10], antileishmanial [11,12], antitubercular [13], anticancer [14–16], anti-HIV [2,5], antibacterial [17–19], antimalarial, antituberculosis, antiulcer, antidiabetic, antiprotozoal [1,2,5] and nonlinear optical (NLO) properties. β-ionone (4- [2,6,6-trimethyl-1-cyclohexen-1-yl]-3-buten-2-one) is the basic nucleus structure of retinoic acid, retinol, β-carotene, and vitamin A. Similar to chalcones, this phytochemical compound is found in many fruits and vegetables and its analogs have several biological properties, such as anti-carcinogenic and antitumor activities [20,21]. Among these analogs, we can mention the terpenoid-like chalcone, which is formed by the condensation of the β-ionone nucleus with an aromatic aldehyde. This class of chalcones has some activities described in the literature, such as antiandrogens, antimicrobial, and antiproliferative agents [20,22–24].

Bis-chalcones are α, β unsaturated ketones capable of absorbing UV-VIS light due to extensive conjugation. Its chromophore can be fine-tuned through intramolecular charge-transfer processes. These phenomena are characteristic of a highly delocalized π electron system and the absorption maximum (λ_{max}) is usually shifted to longer wavelengths as the amount of delocalization increased [25]. This phenomenon is dependent on aromatic ring type and substitution pattern, leading to a small energy gap between the highest occupied molecular orbital (HOMO) and lowest unoccupied molecular orbital (LUMO) [25,26].

It is known that changing the crystal packing affects the chemical, physical, material science, and biological properties of the compound [27]. In this sense, analyzing polymorphs (com-

* Corresponding authors at: Grupo de Química Teórica e Estrutural de Anápolis, Universidade Estadual de Goiás, Anápolis, GO, Brazil.
E-mail addresses: silva.c.marianna@gmail.com (M.C. Silva), hbnapolitano@gmail.com (H.B. Napolitano).

https://doi.org/10.1016/j.molstruc.2020.129743
0022-2860/

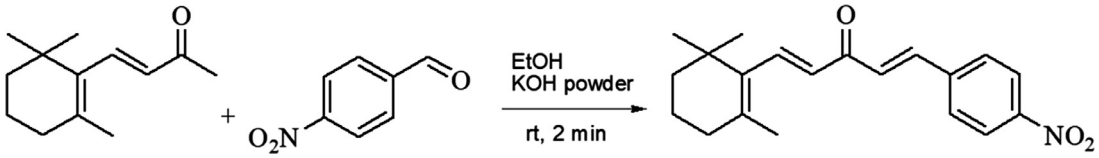

Scheme 1. Synthesis of (1*E*,4*E*)-1-(4-nitrophenyl)-5-(2,6,6-trimethylcyclohex-2-en-1-yl)penta-1,4-dien-3-one.

pounds with the same molecular structure but different crystalline phases and lattice energy) is important when considering different physicochemical and/or biological properties [28]. In this article, conformational polymorphs (with molecular twists associated with long-range ordering) [28] of three polymorphs of chalcone (1*E*,4*E*)-1-(4-nitrophenyl)-5-(2,6,6-trimethylcyclohex-2-en-1-yl)penta-1,4-dien-3-one (CHL) were analyzed. Structural elucidation analysis was performed in terms of molecular geometry and intermolecular interactions. The supramolecular arrangement of all structures was characterized by the Hirshfeld surface (HS) [29–31] while the electronic study was carried out using density functional theory (DFT) to generate the frontier molecular orbitals (FMO) [32].

2. Experimental and computational procedures

2.1. Synthesis and crystallization

Chemicals and solvents required for orthorhombic CHL (CHL-o) synthesis were obtained from commercial sources and used without further purification. 1 mmol (192.3 mg) of (3*E*)-4-(2,6,6-trimethylcyclohex-1-enyl) but-3-en-2-one (β-ionone, $C_{13}H_{20}O$) and 1 mmol (151.1 mg) of 4-nitrobenzaldehyde ($C_7H_5NO_3$) were added in ethanol (1 mL). Then, pulverized KOH (1 mmol; 56.1 mg) was added to the reaction mixture and manually shaken for 2 min. at 298.15 K. The reaction's progress was monitored by TLC (Silica gel 60 UV254) plate using a mixture of solvent (ethyl acetate/hexane 3:7) as eluent (Scheme 1). Finally, a yellow precipitate was obtained and collected by vacuum filtration followed by a crystallization process using ethanol as solvent. (1*E*,4*E*)-1-(2,6,6-trimethylcyclohex-1-enyl)-5-(4-nitrophenyl)penta-1,4-dien-3-one was obtained in 92% yield (0.92 mmol; 299.36 mg), fusion range 399,15-401,15 K. From the analysis of the GC chromatogram, a single peak is observed at 11.78 min, whose mass spectrum is characteristic for CHL-o fragments (m/z 44, 102, 130, 176, 207, 268, 310 and 325).

Crystals of CHL-o were obtained from a dichloromethane solution of the chalcone in a conical flask with the mixture kept at 298.15 - 303.15 K for slow evaporation for 72 h until the crystals formed. A Bruker Avance 500 MHZ nuclear magnetic resonance (NMR) spectrometer was used to obtain ^{1}H- and ^{13}C-NMR spectra (Figures S1 and S2) with TMS as internal standard and $CDCl_3$ as solvent. The corresponding shifts reveal the purity and structural conformation of the compound. The infrared (IR) spectra (Figure S3) were recorded using a Perkin Elmer 8400S FT-IR spectrometer. The chalcone was analyzed by the Fourier transform infrared (FTIR) transmission technique as KBr pellets and the spectra were collected in the middle infrared spectral range (4000–400 cm^{-1}). ^{1}H NMR (500 MHz, $CDCl_3$) δ 8.28 (d, J = 8.9 Hz, 2H), 7.76 (d, J = 8.9 Hz, 2H), 7.70 (d, J = 15.9 Hz, 1H), 7.59 (dd, J = 16.0, 6.3 Hz, 1H), 7.13 (d, J = 15.9 Hz, 1H), 6.50 (d, J = 16.0 Hz, 1H), 2.16 – 2.11 (m, 2H), 1.87 (s, 3H), 1.71 – 1.62 (m, 2H), 1.55-1.51 (m, 2H), 1.15 (s, 6H).; ^{13}C NMR (126 MHz, $CDCl_3$) δ 188.33, 148.39, 144.29, 141.23, 139.47, 138.33, 136.46, 129.17, 129.13, 128.82, 124.21, 39.86, 34.21, 33.90, 28.90, 22.00, 18.83.

2.2. Gas chromatography-mass spectrometry

The gas chromatogram (Figure S4) and mass spectrum (GC-MS) (Figure S5) of the synthesized compound were recorded in a Shimadzu QP2010 Ultra equipped with capillary column CBP-5 ($30 \times 0.25 \times 0.25$), with an injection volume of 1.0 μL, in Split Mode and Helium as drag gas with 1.0 mL.min^{-1} flow. The analysis was carried out with injector temperature at 553.15 K and the detector at 583.15 K. The initial oven temperature was 373.15 K (held for 2 min), followed by a heating ramp of 303.15 K .min^{-1} till 573.15 K (held for 10 min).

2.3. Crystallographic characterization

The single crystal CHL-o data were obtained from X-ray diffraction on a Bruker APEX-II CCD diffractometer, with graphite-monochrome Mo$K\alpha$ radiation (λ = 0.71073 Å), at 120 K. The molecular structure was solved by direct methods using ShelXS [33], and refined by full-matrix least-squares method on F^2 using ShelXL [34] software, incorporated into Olex2 [35]. Free anisotropic parameters were adopted for non-hydrogen atoms, and fixed isotropic parameters for hydrogen atoms [U_{iso} (H) = 1.2 U_{eq} (methylene group) or 1.5 U_{eq} (methyl group)]. Hydrogen atoms were constrained to 0.93 Å (C_{sp}^2 –H), 0.96 Å (C_{sp}^3 –H in CH_3 groups), 0.97 Å (C_{sp}^3 –H in CH_2 groups) and 0.98 Å (C_{sp}^3 –H in CH groups) according to the riding model. The programs Ortep [36] and Mercury [37] were used for interpreting molecular and supramolecular arrangements. Potential hydrogen-bond interactions were verified through Platon [38] software. The crystallographic information file (CIF) was deposited at Cambridge Crystallographic Data Centre (CCDC) [39] under deposition code 2023065. The CIF of the other two monoclinic polymorphs, [code: 1029766 (CHL-m_1) [22] and 818053 (CHL-m_2) [40]], were extracted from the CCDC database.

HS can be understood as crystal partition space with regions where there is electron distribution of a sum of spherical atoms [41]· [42], constructed through Equation 1:

$$\boldsymbol{W}(\boldsymbol{r}) = \sum_{\boldsymbol{a}\in\boldsymbol{molecule}} \boldsymbol{p_a}(\boldsymbol{r}) \; / \sum_{\boldsymbol{a}\in\boldsymbol{crystal}} \boldsymbol{p_a}\;(\boldsymbol{r}) \tag{1}$$

where $W(r)$, is a weight function with $W(r) \geq 0.5$, the numerator is the *promolecule* (summed over the atoms in the molecule of interest), the denominator is from the *procrystal* (summed over the atoms in the crystal of interest) [42] [29]. The electron density of the atomic fragment p_a (r) is defined in Equation 2:

$$\boldsymbol{p_a}\;(\boldsymbol{r}) = \boldsymbol{W_a}\;(\boldsymbol{r})\boldsymbol{p^{mol}}(\boldsymbol{r}) \tag{2}$$

where, $p^{mol}(r)$ indicates molecular electron density [43]. The normalized contact distances (*dnorm*) (Equation 3) are defined from *di* (indicates a donor region of intermolecular contacts and distance between the nucleus of an internal atom to the surface) and *de* (indicates an acceptor region of intermolecular contacts and distance between an external nucleus to the surface) [29].

$$\boldsymbol{d_{norm}} = \left(\boldsymbol{d_i} - \boldsymbol{r_i^{vdw}}\right)/\boldsymbol{r_i^{vdw}} + \left(\boldsymbol{d_e} - \boldsymbol{r_e^{vdw}}\right)/\boldsymbol{r_e^{vdw}} \tag{3}$$

where, $\boldsymbol{r}^{vdw}$ is the van der Waal (vdW) radius. The red and blue colors are associated with shorter and longer distances greater than the van der Waals intermolecular contact, respectively [29].

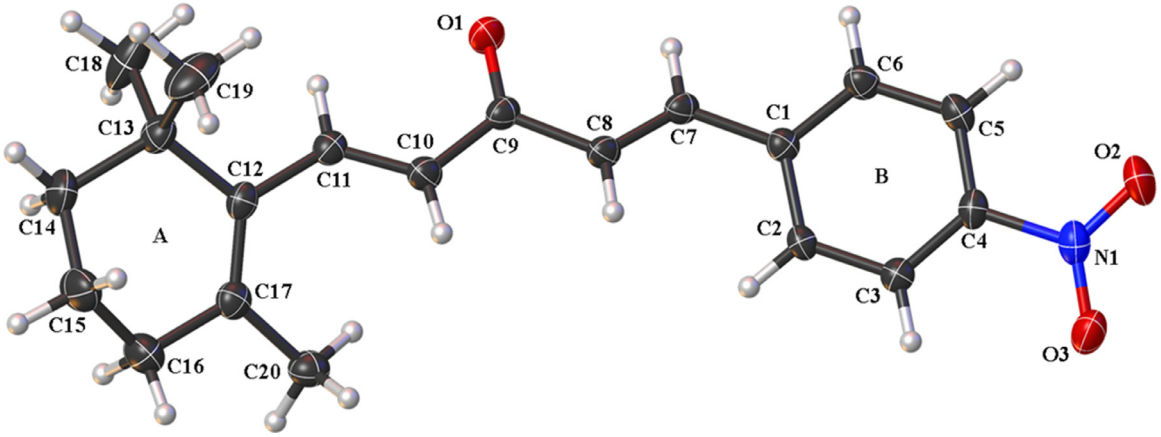

Fig. 1. Ortep representation with 50% probability ellipsoids, of the CHL-o crystal. Disorder at C14' and C15' omitted for clarity.

The shape index surface identifies hydrophobic donor and acceptor interactions, by red concave regions and blue convex regions, respectively. The 2D fingerprint is a map of all contacts present in the molecule that are unique to each compound. This map uses the chemical environment and is unique for each molecule [44]. Crystal Explorer [45] was used to calculate HS and 2D fingerprint plots.

2.4. Theoretical calculation

Theoretical calculations were performed for CHL-o, CHL-m_1, and CHL-m_2, from the experimental data (X-ray data). The geometry determined from the X-ray data were optimized in the gas phase using the Density Functional Theory (DFT) [46] by Gaussian09 [47] software applying the M06-2X [48] functional and 6-311++G(d,p) [49,50] basis set, because it has shown good results in the literature [49,51–54], is indicated for noncovalent interactions [48,55], and considers electronic correlation. Based on the results generated, we performed a comparative analysis between the structures (CHL-o, CHL-m_1, and CHL-m_2) through the FMO, with the highest occupied molecular orbital (HOMO) and lowest unoccupied molecular orbital (LUMO) [56,57].

3. Results and discussion

3.1. Solid-state characterization of CHL-o

Figure 1 shows the numbering scheme used for CHL-o, which crystallizes in the orthorhombic, centrosymmetric space group *P*bca. The Ring A (trimethylcyclohexene) is disordered with two independent sites for atoms C14, C15 (67.4%) and C14', C15' (32.6%). Ring B (nitrobenzene) has a *p*-nitro group (Figure 1). The crystallographic data of the structural refinement are described in Table 1.

Figure 2 shows the planes formed by rings A and B (Θ_1= 30.25°). CHL has a half-chair conformation evidenced by the dihedral angles C13-C14-C15-C16 [-65.1 (6)°] and C17-C16-C15-C14 [51.3 (5)°]. Ring A shows *syn-clinal* orientation due to the torsion angles around C10-C11-C12-C13-C17. Table 2 shows selected geometrical parameters for CHL-o.

The supramolecular arrangement of CHL-o has a C5–H5···O3 interaction [D···A = 3.449 Å; symmetry code: 3/2-x, -1/2+y, z] involving the nitro group that contributes to a zig-zag cross-repetition in the direction of the *b* axis (Figure 3a), and the C8–H8···O1 interaction [D···A = 3.305 Å; symmetry code: 1/2-x, 1/2+y, z] involving carbonyl group into a repetition along the *b* axis direction (Figure 3b).

Table 1
Crystal structure and refinement data of CHL-o.

Parameter	CHL-o	
Chemical formula	$C_{20}H_{23}NO_3$	
Formula weight	325.39	
Crystal system, space group	Orthorhombic, *P*bca	
Temperature (K)	120 (2)	
Unit cell dimensions	a = 13.9380 (6) Å	α = 90°
	b = 10.6202 (5) Å	β = 90°
	c = 23.4713 (14) Å	γ = 90°
Volume	3474.3 (3)	
Radiation type	Mo $K\alpha$	
Absorption coefficient (mm $^{-1}$)	0.083	
F (000)	1392	
Final *R* índices [$F^2 > 2\sigma$ (F^2)]	0.0457, wR_2 = 0.1026	
R indices (all data)	0.0813, wR_2 = 0.1181	
Goodness-of-fit on F^2	1.017	
No. of reflections	3419	
No. of parameters	239	
$\Delta\rangle_{max}$, $\Delta\rangle_{min}$ (e Å^{-3})	0.20, -0.23	

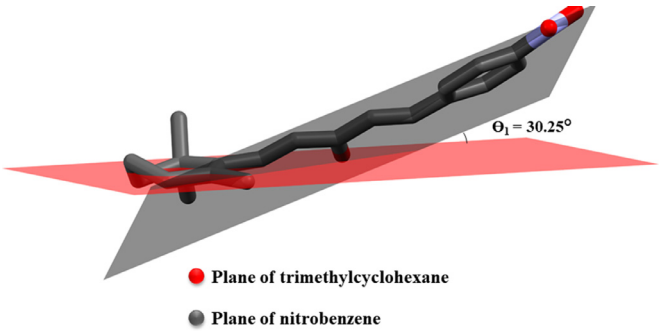

Fig. 2. Dihedral angle of CHL-o formed by planes of A (red) and B (gray) rings. H atoms have been omitted.

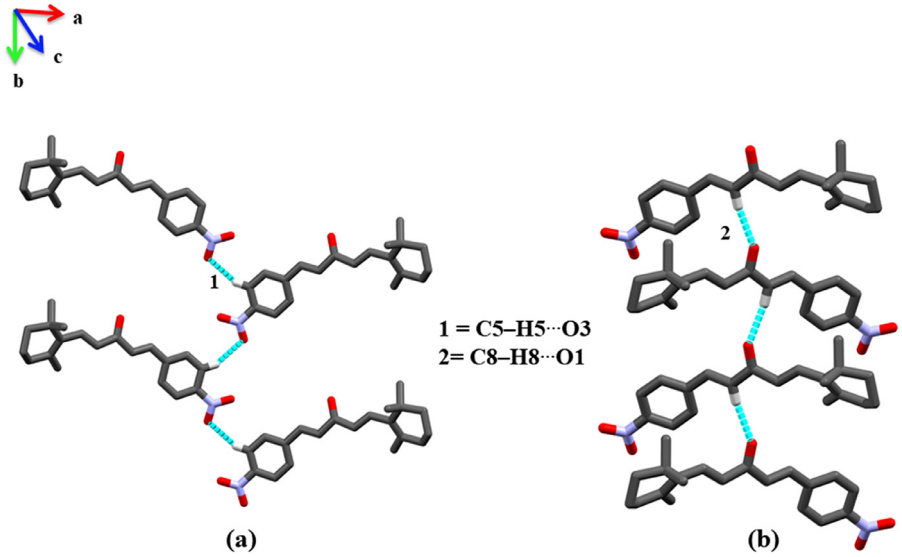

Fig. 3. Interactions of CHL-o formed by C5–H5···O3 (a), and C8–H8···O1 (b). H atoms not involved in interactions have been omitted.

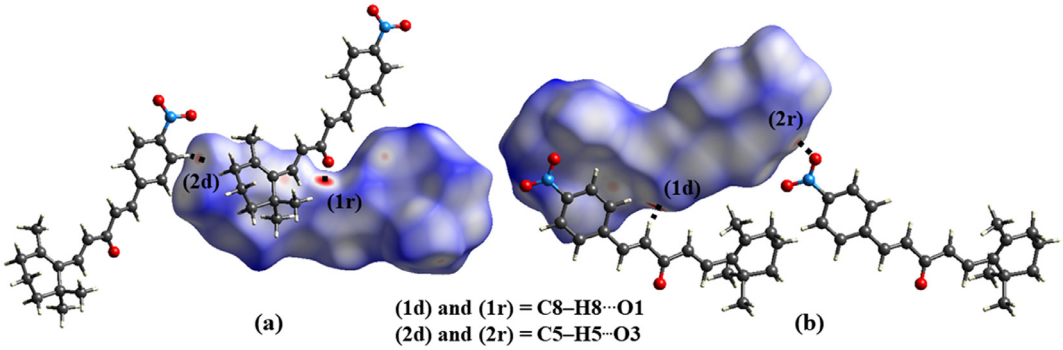

Fig. 4. HS *dnorm* mapped for CHL-o indicates intermolecular contacts. Dotted black lines represent hydrogen bonds.

Table 2
Selected geometrical parameters for CHL-o.

CHL-o	**Bond lengths**	
	C13-C14	1.548 (7) Å
	C14-C15	1.515 (9) Å
	C15-C16	1.541 (4) Å
	Bond angle	
	C14-C15-C16	107.3 (4) °
	Dihedral angle	
	C10-C11-C12-C17	-35.8 (3) °

The contacts C8–H8···O1 and C5–H5···O3 are observed through the HS topological analysis by conventional *dnorm* mapping (ranging from -0.511 to 1.470 Å) (Figure 4a and Figure 4b) and can be described from the intensity of the *di* and *de* contacts. The red dots (1d) and (2d) correspond to *di* contacts, indicating that they act as donors for the interactions C8–H8···O1 and C5–H5···O3, respectively, and the red dots (1r) and (2r) correspond to the *de* contacts, indicating the acceptor regions of the interactions C8 – H8··· O1 and C5 – H5···O3, respectively.

HS shape index is a tool used to recognize hydrophobic interactions ($\pi\cdots\pi$ and C-H$\cdots\pi$), indicated by red concavities over aromatic rings. Compound CHL-o has a C-H$\cdots\pi$ interaction involving Cg1 (center of gravity of the aromatic ring formed by the atoms C1, C2, C3, C4, C5, and C6) with the C18-H18B···Cg1 (D–H = 0.98 Å, H···Cg1 2.88 Å, D···Cg1 = 3.66 Å, D – H···Cg1 = 138° and symmetry code: 1/2-x,-1/2+y,z), shown in Figure 5.

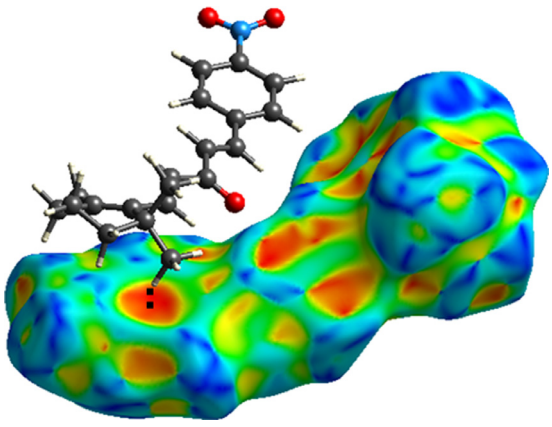

Fig. 5. HS shape index evidencing the interaction C-H$\cdots\pi$ of CHL-o.

Furthermore, the contacts were analyzed from fingerprints (Figure 6) based on the major disorder component of the molecule through a 2D graph with *di* against *de*. The H···H contacts have a higher percentage (50.10%), the O···H contacts have 25.90% and C···H contacts have 18.60%. The absence of C···C interactions indicates that the arrangement is not stabilized by $\pi\cdots\pi$ interactions.

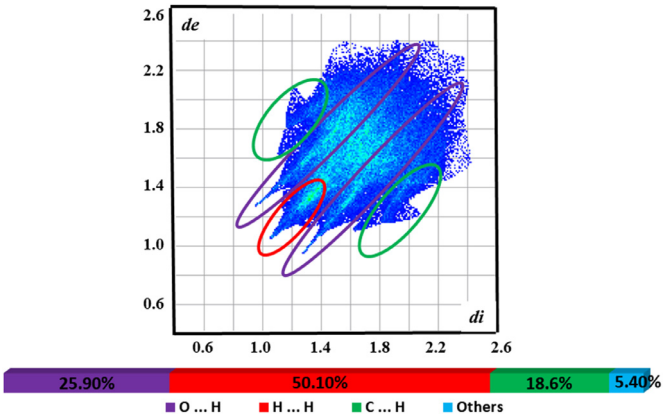

Fig. 6. Fingerprint and quantification of total interactions in CHL-o.

Table 3
The experimental (X-ray) parameters for CHL-m_1 and CHL-m_2.

CHL-m_1	**Bond lengths**	
	C13-C14	1.510 (9) Å
	C14-C15	1.458 (14) Å
	C15-C16	1.437 (16) Å
	Bond angle	
	C14-C15-C16	114.5 (9) °
	Dihedral angle	
	C10-C11-C12-C17	116.9 (5) °
CHL-m_2	**Bond lengths**	
	C13-C14	1.529 (11) Å
	C14-C15	1.550 (3) Å
	C15-C16	1.434 (3) Å
	Bond angle	
	C14-C15-C16	117.4 (12) °
	Dihedral angle	
	C10-C11-C12-C17	-42.4 (3) °

3.2. Comparative polymorphic analysis

The crystallization of polymorphic compounds CHL-m_1 and CHL-m_2 occurred in the monoclinic, centrosymmetric space group $P2_1/c$. CHL-m_1 has an occupational disorder involving the ring A. For CHL-m_1, the classical harmonic model was used. In this model, the atomic displacement is represented with only one site instead of the split-position model (without convergence), obtaining elongated ellipsoids at the site of the disorder (Figure 7a). CHL-m_2 also has an occupational disorder in ring A, which was refined through the split-position model. Figure 7b is presented with the disorder omitted, for better visualization.

Examining the two mean planes for rings A (trimethylcyclohexene) and B (nitrobenzene) resulted in angles of $\Theta_2 = 86.64°$ and $\Theta_3 = 64.41°$ for CHL-m_1 (Figure 8a) and CHL-m_2 (Figure 8b), respectively. The conformational differences are associated with ring A orientation (torsion angles about C10-C11-C12-C17). The trimethylcyclohexene rings in CHL-m_1 and CHL-m_2 have an *anti-clinal* and a *syn-clinal* orientation, respectively. The overlay of CHL-m_1 and CHL-m_2 with CHL-o shows their conformational differences (Figure 8). In addition, the half-chair conformation is observed in the compounds CHL-m_1 and CHL-m_2 (Table 3).

The supramolecular arrangement of CHL-m_1 and CHL-m_2 is stabilized by semi-classical C–H···O interactions, whose geometric parameters are shown in Table 4. The CHL-m_1 presents regular interactions (involving C6–H6···O2 atoms) running parallel to the *c*-direction, and a bifurcated hydrogen bond (involving C8–H8···O1 and C11–H11···O1 atoms) (Figure 9a). In comparison, CHL-m_2 has interactions involving C16–H16A···O1, and C8–H8···O3 also running parallel to the *c*-direction (Figure 9b). The only interaction that is common to CHL-o and its polymorphs is the C8-H8···O1 hydrogen bond. However, their values are divergent. The packing of CHL-m_1 (Figure 10a) and CHL-m_2 (Figure 10b) consists of a *zigzag* form in the *a*-direction, and ribbons in *c* direction. The centrosymmetric crystal packing of CHL-o (Figure 10c) consists of a ribbon motif.

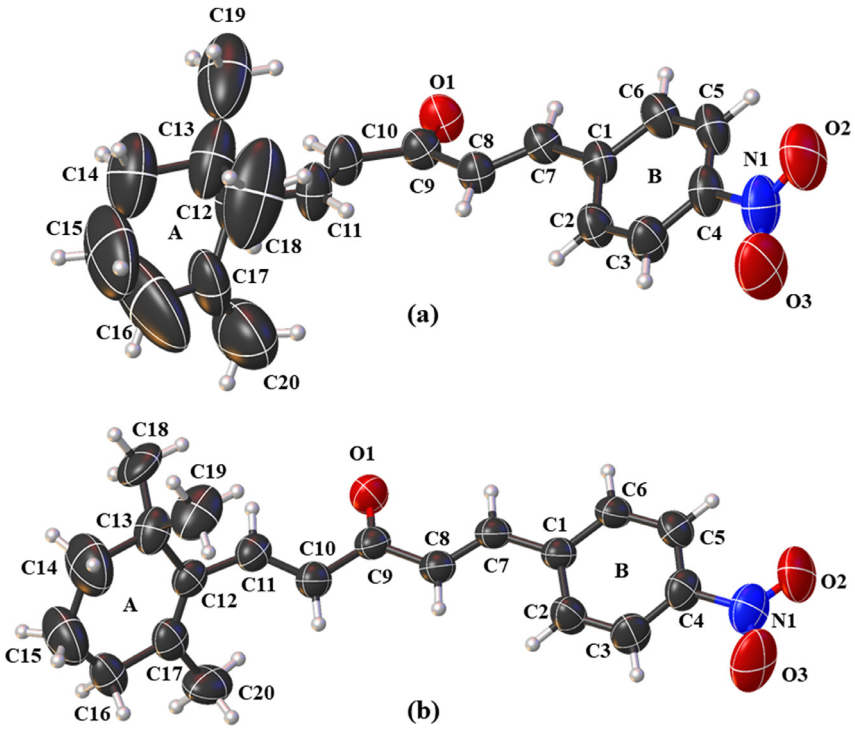

Fig. 7. Ortep representation with 50% displacement ellipsoids of the (a) CHL-m_1 and (b) CHL-m_2 crystal.

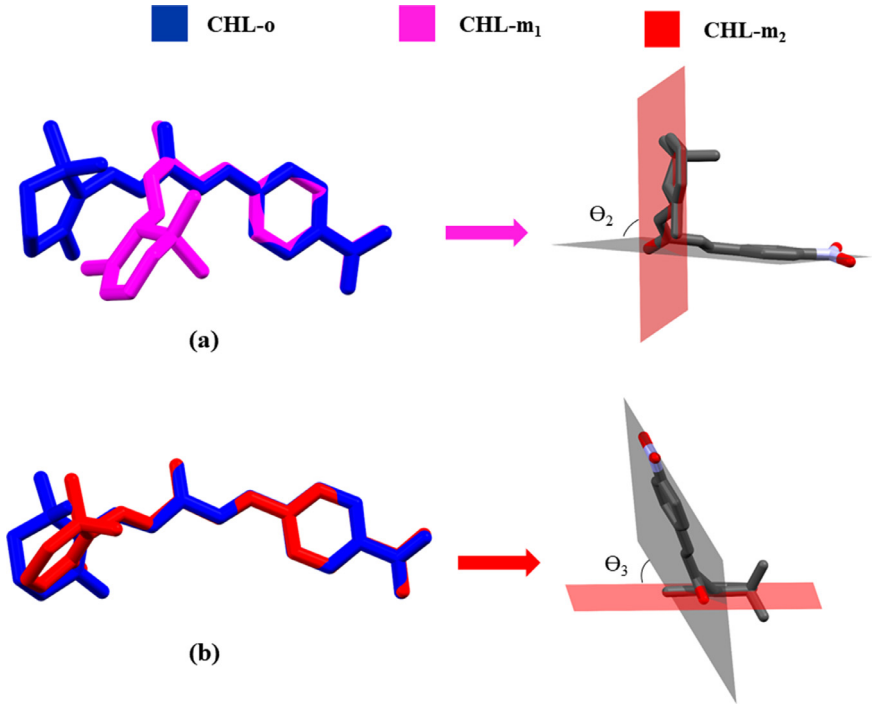

Fig. 8. Overlapping of CHL-o/CHL-m_1 (a) and CHL-o/CHL-m_2 (b), showing CHL-m_1 (Θ_2) and CHL-m_2 (Θ_3) formed by planes of A (red) and B (gray) rings. H atoms have been omitted.

Table 4
Geometric parameters of intermolecular interactions of CHL-m_1 and CHL-m_2.

	D – H···A	D – H	H···A	D···A	D – H···A	Symmetry code
CHL-m_1	C8–H8···O1	0.92	2.60	3.531	175	x,1/2-y,-1/2+z
	C11–H11···O1	0.93	2.62	3.493	155	x,1/2-y,-1/2+z
	C6–H6···O2	0.92	2.67	3.418	137	x,1+y,z
CHL-m_2	C16–H16A···O1	0.96	2.62	3.378	134	x,1/2-y,-1/2+z
	C8–H8···O3	0.93	2.55	3.394	150	x,-1/2-y,-1/2+z

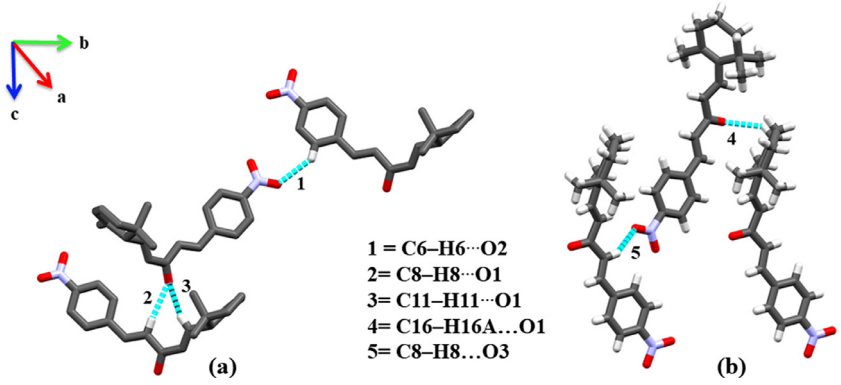

Fig. 9. Intermolecular interactions of CHL-m_1 (a) and CHL-m_2 (b). H atoms not involved in interactions have been omitted.

The intermolecular interactions of the CHL-m_1 and CHL-m_2 compounds are observed and interpreted through the topological analysis of HS by *dnorm* mapping, where donor and acceptor regions of contacts are represented. Interactions of CHL-m_1 are shown in Figure 11a, while interactions of CHL-m_2 are presented in Figure 11b. For CHL-m_1 compound, *di* contacts (donor) and *de* contacts (receptor) are represented by (1d/r), (2d/r)/ and (3d/r) indicating the C8–H8···O1, C11–H11···O1 and C6–H6···O2 interactions, respectively. The C8–H8···O1 and C11–H11···O1 are bifurcated interactions and are more intense, contributing to the stabilization supramolecular arrangement. For CHL-m_2, the (4d/r) and (5d/r) regions indicate the C16–H16A···O1 and C8–H8···O3 interactions, respectively.

CHL-m_1 and CHL-m_2 present a hydrophobic interaction C-H···π, represented by the red concave curvature on the shape index surface. CHL-m_1 has an interaction involving Cg1 (gravity center of the aromatic ring formed by the atoms C1 - C6) with C14–H14A···Cg1 (D–H= 0.97 Å, H···Cg1 2.92 Å, D···Cg1= 3.77 Å and D–

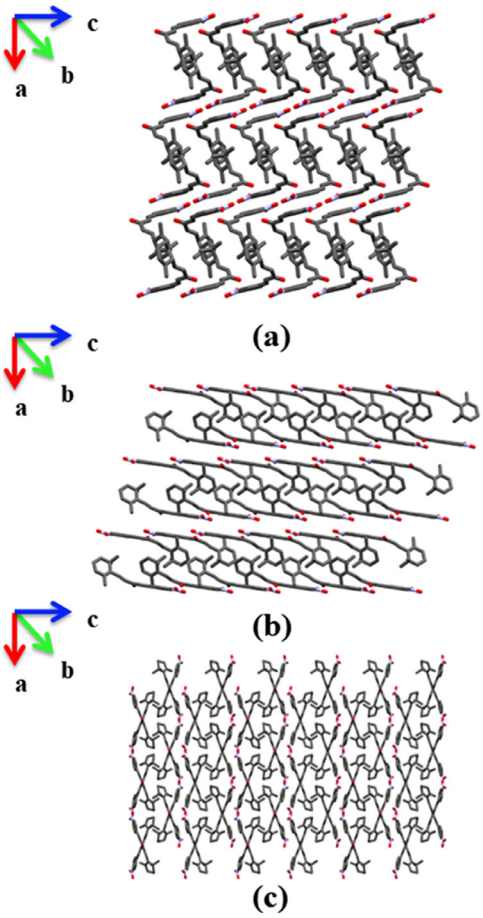

Fig. 10. The crystal packing of CHL-m_1 (a), CHL-m_2 (b), and CHL-o (c). H atoms have been omitted.

H···Cg1= 147°) (Figure 12a). The compound CHL-m_2 has an interaction involving Cg1 (C1 - C6) with the C18-H18A···Cg1 (D–H= 0.96 Å, H···Cg1 3.73 Å, D···Cg1= 4.57 Å and D – H···Cg1= 148°) (Figure 12b).

The fingerprint plot represents the contact percentages of CHL-m_1 (Figure 13a) and CHL-m_2 (Figure 13b) polymorphs with an unique patterns. The O···H contacts are represented by the C–H···O interactions, and the percentage of O···H contact in CHL-m_1 (26.70%) is greater than CHL-m_2 (25.00%) because there is one more semi-classic interaction. This difference can be noticed in the *di* / *de* region around 1.4 with a greater intensity for the CHL-m_1 compound (Figure 13a).

The HOMO orbital is similar for all three terpenoid-like chalcones. The HOMO of all three compounds is spread over aromatic ring B and the LUMO is associated with the trimethylcyclohexene ring A (Figure 14). The bonding orbital and the antibonding orbital are characterized by electronic levels HOMO and LUMO, respectively [57], and the difference between the energies orbitals is called GAP energy ($E_{LUMO} - E_{HOMO} = E_{GAP}$). The GAP for CHL-o is 531.8 kJ/mol, for CHL-m_1 is 581.3 kJ/mol while for CHL-m_2 is 520.7 kJ/mol.

The energy GAP has been used as a simple indicator of kinetic stability [58,59,68–70,60–67], this kinetic stability can be understood as stability related to the activated complex of any further chemical reaction [69,71]. According Manolopoulos *et al.* (1991), [69] large GAP values are associated with high kinetic stability because it is energetically unfavorable to add electrons to a high-lying LUMO, and to extract electrons from a low-lying HOMO, and so to form the activated complex of any potential reaction. Due to the immense number of chemical reactions, it is very complicated estimate the degree of kinetic stability. In this sense, the compound CHL-m_1 is the most stable among the three (581.3 kJ/mol) when compared to CHL-o and CHL-m_2 (regarding gas phase values). When comparing structures CHL-o and CHL-m_2, the GAP value of CHL-o (531.8 kJ/mol) indicates that this structure is more stable than CHL-m_2 (520.7 kJ/mol). Summarizing this, we have an order of stability in the gas phase of CHL-m_1 > CHL-o > CHL-m_2.

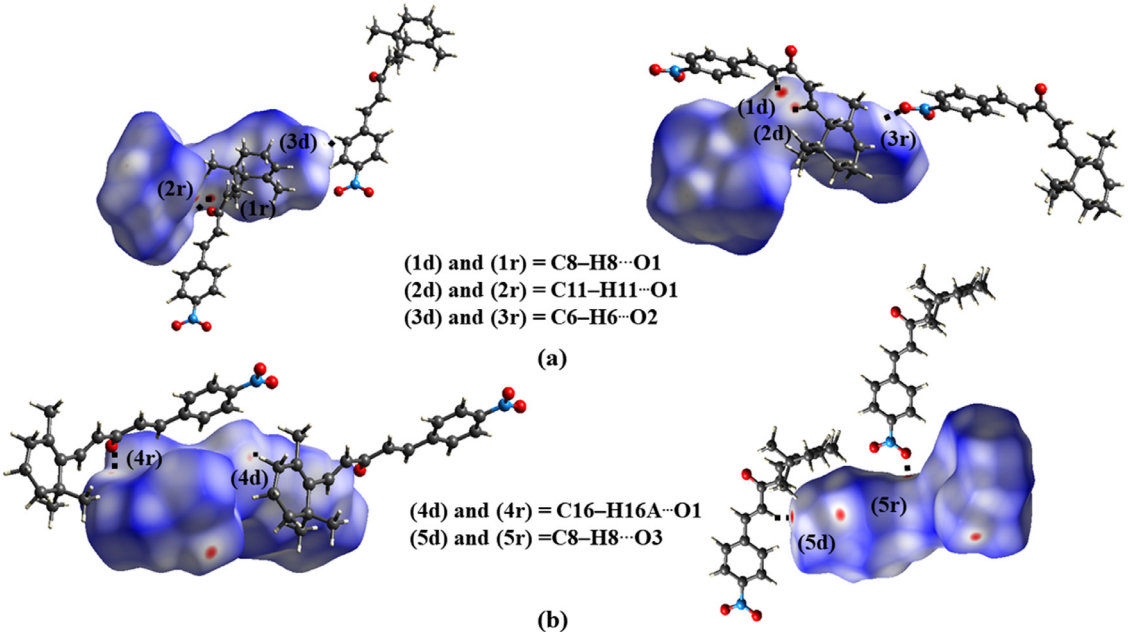

Fig. 11. HS *dnorm* mapped indicates intermolecular contacts for CHL-m_1 (a) and CHL-m_2 (b). Dotted black lines represent hydrogen bonds.

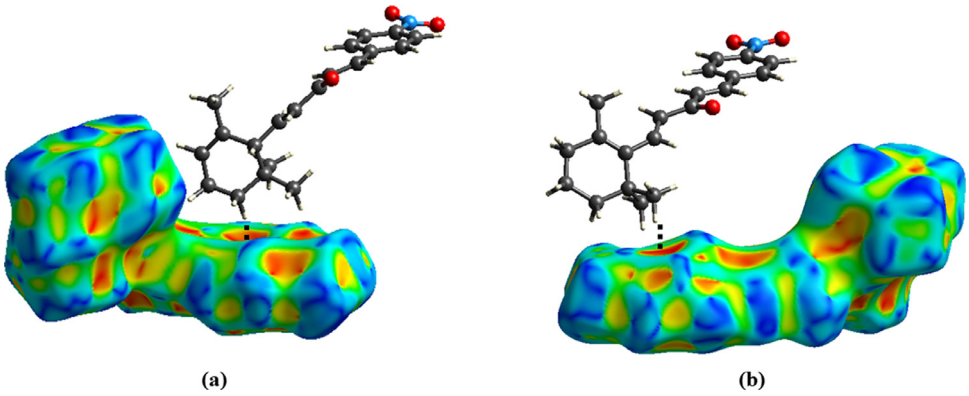

Fig. 12. Hirshfeld surface shape index evidencing the interaction C-H···π of CHL-m_1 (a) and CHL-m_2 (b).

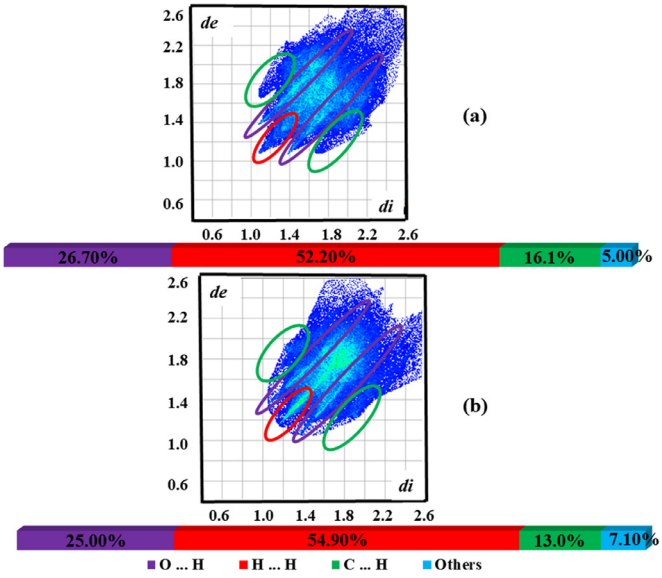

Fig. 13. Fingerprint and quantification of total interactions in CHL-m_1 (a) and CHL-m_2 (b).

4. Conclusions

CHL-o crystallizes in the orthorhombic space group *P*bca while CHL-m_1 and CHL-m_2 crystallized in the monoclinic space group $P2_1/c$. The CHL-o is more planar than CHL-m_1 and CHL-m_2, measured by the angles formed by rings A and B. Ring A for CHL-o, CHL-m_1, and CHL-m_2 has a half chair conformation. The supramolecular arrangement for all three CHL compounds is stabilized by C–H···O and C– H•••π interactions and CHL-m_1 presented one additional C–H···O interaction. According to the GAP energy calculated for the three molecules in the gas phase, the order of stability is CHL-m_1 > CHL-o > CHL-m_2, indicating the structure with no disorder instead of the split-position model as the most stable. All parameters presented indicate the importance of the comparative study of polymorphs for future pharmacological applications. This is due to the ability of physical-chemical properties to be altered by small differences in the crystalline arrangement and stability of the CHL.

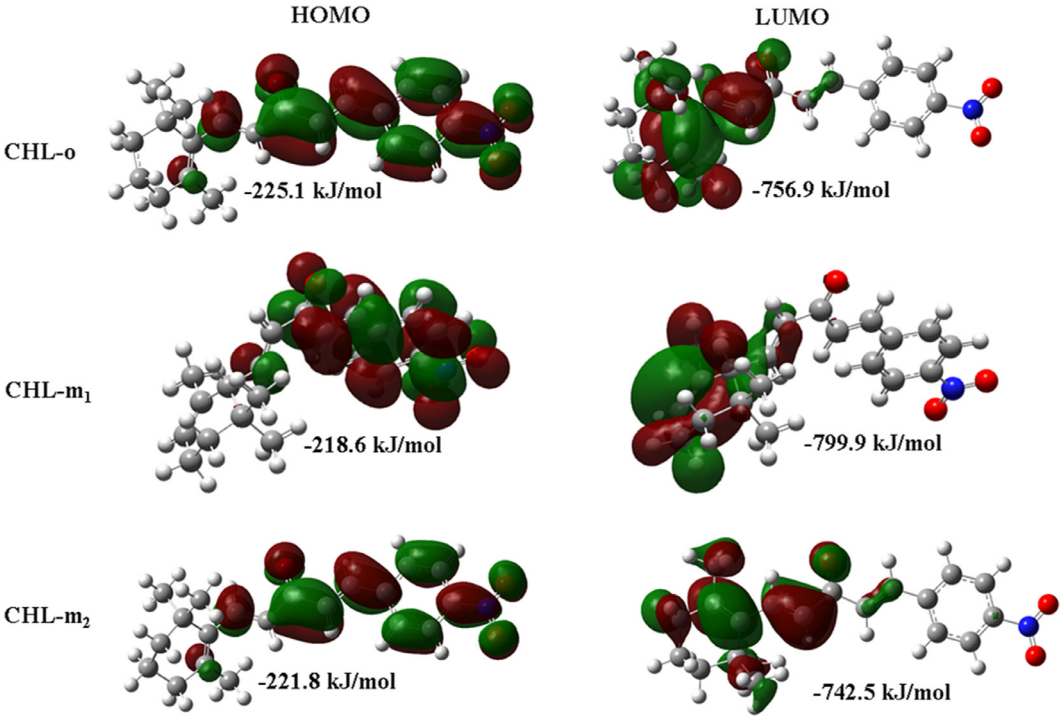

Fig. 14. Molecular orbital distributions (HOMO- LUMO) for CHL-o, CHL-m_1 and CHL-m_2.

Declaration of Competing Interest

The authors declare that they have no known competing financial interests or personal relationships that could have appeared to influence the work reported in this paper.

Acknowledgments

The authors are grateful to Conselho Nacional de Desenvolvimento Científico e Tecnológico, Fundação de Amparo à Pesquisa de Goiás and Coordenação de Aperfeiçoamento de Pessoal de Nível Superior for financial support. Theoretical calculations were performed in the High Performance Computing Center of the Universidade Estadual de Goiás.

References

[1] Z. Rozmer, P. Perjési, Naturally occurring chalcones and their biological activities, Phytochem. Rev 15 (2016) 87–120 https://doi.org/10.1007/s11101-014-9387-8.
[2] A. Rammohan, J.S. Reddy, G. Sravya, C.N. Rao, G.V. Zyryanov, Chalcone synthesis, properties and medicinal applications: a review, Environ. Chem. Lett. 18 (2020) 433–458 https://doi.org/10.1007/s10311-019-00959-w.
[3] A. Özdemir, M.D. Altintop, B. Sever, H.K. Gençer, H.A. Kapkaç, Ö. Atli, M. Baysal, A new series of pyrrole-based chalcones: Synthesis and evaluation of antimicrobial activity, cytotoxicity, and genotoxicity, Molecules 22 (2017) 1–16 https://doi.org/10.3390/molecules22122112.
[4] M.K.A. Ferreira, R.O.dos S. Fontenelle, F.E.A. Magalhães, P.N. Bandeira, J.E.S.A. de Menezes, H.S. dos Santos, Artigo Potencial Farmacológico de Chalconas : Uma Breve Revisão, Rev. Virtual Quim. 10 (2018) 1455–1473 https://doi.org/10.21577/1984-6835.20180099.
[5] S.L. Gaonkar, U.N. Vignesh, Synthesis and pharmacological properties of chalcones: a review, Res. Chem. Intermed 43 (2017) 6043–6077 https://doi.org/10.1007/s11164-017-2977-5.
[6] M. Funakoshi-Tago, K. Okamoto, R. Izumi, K. Tago, K. Yanagisawa, Y. Narukawa, F. Kiuchi, T. Kasahara, H. Tamura, Anti-inflammatory activity of flavonoids in Nepalese propolis is attributed to inhibition of the IL-33 signaling pathway, Int. Immunopharmacol 25 (2015) 189–198 https://doi.org/10.1016/j.intimp.2015.01.012.
[7] S. Hirai, Y.I. Kim, T. Goto, M.S. Kang, M. Yoshimura, A. Obata, R. Yu, T. Kawada, Inhibitory effect of naringenin chalcone on inflammatory changes in the interaction between adipocytes and macrophages, Life Sci 81 (2007) 1272–1279 https://doi.org/10.1016/j.lfs.2007.09.001.
[8] Z. Nowakowska, A review of anti-infective and anti-inflammatory chalcones, Eur. J. Med. Chem 42 (2007) 125–137 https://doi.org/10.1016/j.ejmech.2006.09.019.
[9] G. Cioffi, L.M. Escobar, A. Braca, N. De Tommasi, Antioxidant chalcone glycosides and flavanones from Maclura (Chlorophora) tinctoria, J. Nat. Prod. 66 (2003) 1061–1064 https://doi.org/10.1021/np030127c.
[10] T.N. Doan, D.T. Tran, Synthesis, Antioxidant and Antimicrobial Activities of a Novel Series of Chalcones, Pyrazolic Chalcones, and Allylic Chalcones, Pharmacol. & Pharm 02 (2011) 282–288 https://doi.org/10.4236/pp.2011.24036.
[11] A. Hermoso, I.A. Jiménez, Z.A. Mamani, I.L. Bazzocchi, J.E. Piñero, A.G. Ravelo, B. Valladares, Antileishmanial activities of dihydrochalcones from piper elongatum and synthetic related compounds. Structural requirements for activity, Bioorganic Med. Chem. 11 (2003) 3975–3980 https://doi.org/10.1016/S0968-0896(03)00406-1.
[12] U. Rashid, R. Sultana, N. Shaheen, S.F. Hassan, F. Yaqoob, M.J. Ahmad, F. Iftikhar, N. Sultana, S. Asghar, M. Yasinzai, F.L. Ansari, N.A. Qureshi, Structure based medicinal chemistry-driven strategy to design substituted dihydropyrimidines as potential antileishmanial agents, Eur. J. Med. Chem 115 (2016) 230–244 https://doi.org/10.1016/j.ejmech.2016.03.022.
[13] E.M. Guantai, K. Ncokazi, T.J. Egan, J. Gut, P.J. Rosenthal, R. Bhampidipati, A. Kopinathan, P.J. Smith, K. Chibale, Enone- and chalcone-chloroquinoline hybrid analogues: In silico guided design, synthesis, antiplasmodial activity, in vitro metabolism, and mechanistic studies, J. Med. Chem. 54 (2011) 3637–3649 https://doi.org/10.1021/jm200149e.
[14] W. Wu, H. Ye, L. Wan, X. Han, G. Wang, J. Hu, M. Tang, X. Duan, Y. Fan, S. He, L. Huang, H. Pei, X. Wang, X. Li, C. Xie, R. Zhang, Z. Yuan, Y. Mao, Y. Wei, L. Chen, Millepachine, a novel chalcone, induces G2/M arrest by inhibiting CDK1 activity and causing apoptosis via ROS-mitochondrial apoptotic pathway in human hepatocarcinoma cells in vitro and in vivo, Carcinogenesis 34 (2013) 1636–1643 https://doi.org/10.1093/carcin/bgt087.
[15] P.S. Bhale, H.V. Chavan, S.B. Dongare, S.N. Shringare, Y.B. Mule, S.S. Nagane, B.P. Bandgar, Synthesis of extended conjugated indolyl chalcones as potent anti-breast cancer, anti-inflammatory and antioxidant agents, Bioorganic Med. Chem. Let 27 (2017) 1502–1507 https://doi.org/10.1016/j.bmcl.2017.02.052.
[16] D. Coskun, M. Erkisa, E. Ulukaya, M.F. Coskun, F. Ari, Novel 1-(7-ethoxy-1-benzofuran-2-yl) substituted chalcone derivatives: Synthesis, characterization and anticancer activity, Eur. J. Med. Chem 136 (2017) 212–222 https://doi.org/10.1016/j.ejmech.2017.05.017.
[17] M. Go, X. Wu, X. Liu, Chalcones: An Update on Cytotoxic and Chemoprotective Properties, Curr. Med. Chem 12 (2005) 483–499 https://doi.org/10.2174/0929867053363153.
[18] K.Y. Oh, J.H. Lee, M.J. Curtis-Long, J.K. Cho, J.Y. Kim, W.S. Lee, K.H. Park, Glycosidase inhibitory phenolic compounds from the seed of Psoralea corylifolia, Food Chem 121 (2010) 940–945 https://doi.org/10.1016/j.foodchem.2010.01.022.
[19] M. Xu, P. Wu, F. Shen, J. Ji, K.P. Rakesh, Chalcone derivatives and their antibacterial activities: Current development, Bioorg. Chem. 91 (2019) 1–17 https://doi.org/10.1016/j.bioorg.2019.103133.
[20] J. Zhou, G. Geng, J.H. Wu, Synthesis and in vitro characterization of ionone-based chalcones as novel antiandrogens effective against multiple clinically relevant androgen receptor mutants, Invest. New Drugs 28 (2010) 291–298 https://doi.org/10.1007/s10637-009-9251-7.
[21] M. Ansari, S. Emami, β-Ionone and its analogs as promising anticancer agents, Eur. J. Med. Chem 123 (2016) 141–154 https://doi.org/10.1016/j.ejmech.2016.07.037.
[22] R.S. Lima, C.N. Perez, C.C. Silva, M.J. Santana, H.K.Q. Júnior, S. Barreto, M.O. De Moraes, F.T. Martins, Structure and cytotoxic activity of terpenoid-like chalcones, Arab. J. Chem 12 (2016) 3890–3901 https://doi.org/10.1016/j.arabjc.2016.02.013.
[23] V. Sharma, A. Chaudhary, S. Arora, A.K. Saxena, M.P.S. Ishar, β-Ionone derived chalcones as potent antiproliferative agents, Eur. J. Med. Chem 69 (2013) 310–315 https://doi.org/10.1016/j.ejmech.2013.08.017.
[24] V. Sharma, G. Singh, H. Kaur, A.K. Saxena, M.P.S. Ishar, Synthesis of β-ionone derived chalcones as potent antimicrobial agents, Bioorganic Med. Chem. Lett 22 (2012) 6343–6346 https://doi.org/10.1016/j.bmcl.2012.08.084.
[25] A.J. Pai, B.K. Sarojini, K.R. Harshitha, B. Shivarama Holla, A.G. Lobo, Spectral, morphological and optical studies on bischalcone doped polylactic acid (PLA) thin films as luminescent and UV radiation blocking materials, Opt. Mater. (Amst) 90 (2019) 145–151 https://doi.org/10.1016/j.optmat.2019.02.028.
[26] L. Shen, Z. Li, X. Wu, W. Zhou, J. Yang, Y. Song, Ultrafast broadband nonlinear optical properties and excited-state dynamics of two bis-chalcone derivatives, R. Soc. Chem. 10 (2020) 15199–15205 https://doi.org/10.1039/d0ra01592j.
[27] M. Li, A.H. Balawi, P.J. Leenaers, L. Ning, G.H.L. Heintges, T. Marszalek, W. Pisula, M.M. Wienk, S.C.J. Meskers, Y. Yi, F. Laquai, R.A.J. Janssen, Impact of polymorphism on the optoelectronic properties of a low-bandgap semiconducting polymer, Nat. Commun 10 (2019) 1–11 https://doi.org/10.1038/s41467-019-10519-z.
[28] B. Sengupta, P.K. Sengupta, R. Grant, M. Beasley, B. Mason, T.L. Love, Conformational Polymorphism in Organic Crystals : Structural and Functional aspects -A Review Article Details, Acc. Chem. Res 41 (2019) 595–604 https://doi.org/10.33790/crmc1100104.
[29] M.A. Spackman, D. Jayatilaka, Hirshfeld surface analysis, CrystEngComm 11 (2009) 19–32 https://doi.org/10.1039/B818330A.
[30] J.J. McKinnon, M.A. Spackman, A.S. Mitchell, Novel tools for visualizing and exploring intermolecular interactions in molecular crystals, Acta Crystallogr. Sect. B Struct. Sci. 60 (2004) 627–668 https://doi.org/10.1107/S0108768104020300.
[31] J.J. McKinnon, D. Jayatilaka, M.A. Spackman, Towards quantitative analysis of intermolecular interactions with Hirshfeld surfaces, Chem. Commun (2007) 3814 https://doi.org/10.1039/B704980C.
[32] D.H. Pereira, F.A. La Porta, R.T. Santiago, D.R. Garcia, T.C. Ramalho, New Perspectives on the Role of Frontier Molecular Orbitals in the Study of Chemical Reactivity: A Review, Rev. Virtual Química 8 (2016) 425–453 https://doi.org/10.5935/1984-6835.20160032.
[33] G.M. Sheldrick, A short history of SHELX, (2008) 112–122. https://doi.org/10.1107/S0108767307043930.
[34] G.M. Sheldrick, Crystal structure refinement with SHELXL, Acta Crystallogr. Sect. C Struct. Chem 71 (2015) 3–8 https://doi.org/10.1107/S2053229614024218.
[35] O.V. Dolomanov, L.J. Bourhis, R.J. Gildea, J.A.K. Howard, H. Puschmann, OLEX2 : a complete structure solution, refinement and analysis program, J. Appl. Crystallogr. 42 (2009) 339–341 https://doi.org/10.1107/S0021889808042726.
[36] L.J. Farrugia, WinGX and ORTEP for Windows: an update, J. Appl. Crystallogr. 45 (2012) 849–854 https://doi.org/10.1107/S0021889812029111.
[37] C.F. Macrae, I.J. Bruno, J.A. Chisholm, P.R. Edgington, P. Mccabe, E. Pidcock, L. Rodriguez-monge, R. Taylor, J. Van De Streek, P.A. Wood, Mercury CSD 2 . 0 – new features for the visualization and investigation of crystal structures, (2008) 466–470. https://doi.org/10.1107/S0021889807067908.
[38] A.L. Spek, research papers Single-crystal structure validation with the program PLATON research papers, (2003) 7–13.
[39] C.R. Groom, I.J. Bruno, M.P. Lightfoot, S.C. Ward, The Cambridge structural database, Acta Crystallogr. Sect. B Struct. Sci. Cryst. Eng. Mater. 72 (2016) 171–179 https://doi.org/10.1107/S2052520616003954.
[40] W.B. Fernandes, L.A. Malaspina, F.T. Martins, L.M. Lião, A.J. Camargo, C. Lariucci, C. Noda-Perez, H.B. Napolitano, Conformational variability in a new terpenoid-like bischalcone: Structure and theoretical studies, J. Struct. Chem. 54 (2013) 1112–1121 https://doi.org/10.1134/S0022476613060164.
[41] J.J. Mckinnon, M.A. Spackman, A.S. Mitchell, Novel tools for visualizing and exploring intermol- ecular interactions in molecular crystals, Acta Crystallogr. Sect. B Struct. Sci. Cryst. Eng. Mater B60 (2004) 627–668 https://doi.org/10.1107/S0108768104020300.
[42] F.L. Hirshfeld, Bonded-Atom Fragments for Describing Molecular Charge Densities, 138 (1977) 129–138.
[43] C. Jelsch, K. Ejsmont, The enrichment ratio of atomic contacts in crystals, an indicator derived from the Hirshfeld surface analysis, (2014) 119–128. https://doi.org/10.1107/S2052252514003327.

[44] M.A. Spackman, J.J. Mckinnon, Fingerprinting intermolecular interactions in molecular crystals, CrystEngComm 4 (2002) 378–392 https://doi.org/10.1039/b203191b.
[45] M.A. Wolff, S.K., Grimwood, D.J., McKinnon, J.J., Turner, M.J., Jayatilaka, and D. Spackman, Crystal Explorer 3.0., (2012).
[46] K. Burke, Perspective on density functional theory, J. Chem. Phys. 136 (2012) 150901 https://doi.org/10.1063/1.4704546.
[47] M.J. Frisch, G.W. Trucks, H.B. Schlegel, G.E. Scuseria, M.A. Robb, J.R. Cheeseman, G. Scalmani, V. Barone, B. Mennucci, G.A. Petersson, E. Al., Gaussian 09, Revision A.02, (2009).
[48] Y. Zhao, D.G. Truhlar, The M06 suite of density functionals for main group thermochemistry, thermochemical kinetics, noncovalent interactions, excited states, and transition elements: Two new functionals and systematic testing of four M06-class functionals and 12 other function, Theor. Chem. Acc 120 (2008) 215–241 https://doi.org/10.1007/s00214-007-0310-x.
[49] R. Krishnan, J.S. Binkley, R. Seeger, J.A. Pople, Self-consistent molecular orbital methods. XX. A basis set for correlated wave functions, J. Chem. Phys. 72 (1980) 650–654 https://doi.org/10.1063/1.438955.
[50] A.D. McLean, G.S. Chandler, Contracted Gaussian basis sets for molecular calculations. I. Second row atoms, Z=11-18, J. Chem. Phys. 72 (1980) 5639–5648 https://doi.org/10.1063/1.438980.
[51] L.G. Santin, E.M. Toledo, V.H. Carvalho-Silva, A.J. Camargo, R. Gargano, S.S. Oliveira, Methanol Solvation Effect on the Proton Rearrangement of Curcumin's Enol Forms: An Ab Initio Molecular Dynamics and Electronic Structure Viewpoint,, J. Phys. Chem. C. 120 (2016) 19923–19931 https://doi.org/10.1021/acs.jpcc.6b02393.
[52] C. Valverde, F.A.P. Osório, T.L. Fonseca, B. Baseia, DFT study of third-order nonlinear susceptibility of a chalcone crystal, Chem. Phys. Lett 706 (2018) 170–174 https://doi.org/10.1016/j.cplett.2018.06.001.
[53] R.R. Ternavisk, A.J. Camargo, F.B.C. Machado, J.A.F.F. Rocco, G.L.B. Aquino, V.H.C. Silva, H.B. Napolitano, Synthesis, characterization, and computational study of a new dimethoxy-chalcone, J. Mol. Model (2014) 20 https://doi.org/10.1007/s00894-014-2526-8.
[54] E.C.M. Faria, V.S. Duarte, A.M. da Silva, F.S. Fernandes, R.L.G. de Paula, C.G. Alonso, G.R. Oliveira, H.B. Napolitano, New Halogen Chalcone with Potential for Application in Biofuels, Energy & Fuels 34 (2020) 5958–5968 https://doi.org/10.1021/acs.energyfuels.0c00322.
[55] E.G. Hohenstein, S.T. Chill, C.D. Sherrill, Assessment of the performance of the M05#2X and M06#2X exchange correlation functionals for noncovalent interactions in biomolecules, J. Chem. Theory Comput. 4 (2008) 1996–2000 https://doi.org/10.1021/ct800308k.
[56] D.H. Pereira, F.A. La Porta, R.T. Santiago, D.R. Garcia, T.C. Ramalho, New Perspectives on the Role of Frontier Molecular Orbitals in the Study of Chemical Reactivity: A Review, Rev. Virtual Quim 8 (2016) 425–453 10.5935/1984-6835.20160032.
[57] G.H. Grant, W.G. Richards, Computational Chemistry, Oxford Science Publications, Oxford, 1996.
[58] C.B.R. Santos, C.C. Lobato, F.S. Braga, S.S.S. Morais, C.F. Santos, C.P. Fernandes, D.S.B. Brasil, L.I.S. Hage-Melim, W.J.C. Macêdo, J.C.T. Carvalho, Application of Hartree-Fock Method for Modeling of Bioactive Molecules Using SAR and QSPR, Comput. Mol. Biosci 04 (2014) 1–24 https://doi.org/10.4236/cmb.2014.41001.
[59] R.G. Parr, Z. Zhou, Absolute hardness: unifying concept for identifying shells and subshells in nuclei, atoms, molecules, and metallic clusters, Acc. Chem. Res. 26 (1993) 256–258 https://doi.org/10.1021/ar00029a005.
[60] X. Liu, T.G. Schmalz, D.J. Klein, Favorable structures for higher fullerenes, Chem. Phys. Lett. 188 (1992) 550–554 https://doi.org/10.1016/0009-2614(92)80864-8.
[61] Z. Zhou, R.G. Parr, Activation hardness: new index for describing the orientation of electrophilic aromatic substitution, J. Am. Chem. Soc. 112 (1990) 5720–5724 https://doi.org/10.1021/ja00171a007.
[62] S.R. Maidur, J.R. Jahagirdar, P.S. Patil, T.S. Chia, C.K. Quah, Structural characterizations, Hirshfeld surface analyses, and third-order nonlinear optical properties of two novel chalcone derivatives, Opt. Mater. (Amst) 75 (2018) 580–594 https://doi.org/10.1016/j.optmat.2017.11.008.
[63] J.L. Gázquez, Hardness and softness in density functional theory, in: Chem. Hardness, Springer-Verlag, Berlin/Heidelberg, n.d.: pp. 27–43. https://doi.org/10.1007/BFb0036798.
[64] A. Irfan, A.G. Al-Sehemi, A.R. Chaudhry, S. Muhammad, First principles study of the n-channel thiophene based heterocyclic chalcones, Optik (Stuttg) 138 (2017) 349–358 https://doi.org/10.1016/j.ijleo.2017.03.070.
[65] A. Aditya Prasad, K. Muthu, V. Meenatchi, M. Rajasekar, R. Agilandeshwari, K. Meena, J. Vijila Manonmoni, S.P. Meenakshisundaram, Optical, vibrational, NBO, first-order molecular hyperpolarizability and Hirshfeld surface analysis of a nonlinear optical chalcone, Spectrochim. Acta Part A Mol. Biomol. Spectrosc 140 (2015) 311–327 https://doi.org/10.1016/j.saa.2014.12.011.
[66] S. Omar, M. Shkir, M. Ajmal Khan, Z. Ahmad, S. AlFaify, A comprehensive study on molecular geometry, optical, HOMO-LUMO, and nonlinear properties of 1,3-diphenyl-2-propen-1-ones chalcone and its derivatives for optoelectronic applications: A computational approach, Optik (Stuttg) 204 (2020) 164172 https://doi.org/10.1016/j.ijleo.2020.164172.
[67] M. Yoshida, J. Aihara, Validity of the weighted HOMO–LUMO energy separation as an index of kinetic stability for fullerenes with up to 120 carbon atoms, Phys. Chem. Chem. Phys 1 (1999) 227–230 https://doi.org/10.1039/a807917j.
[68] R.G. Pearson, Hard and soft acids and bases—the evolution of a chemical concept, Coord. Chem. Rev 100 (1990) 403–425 https://doi.org/10.1016/0010-8545(90)85016-L.
[69] D.E. Manolopoulos, J.C. May, S.E. Down, Theoretical studies of the fullerenes: C34 to C70, Chem. Phys. Lett. 181 (1991) 105–111 https://doi.org/10.1016/0009-2614(91)90340-F.
[70] S. Liu, C.K. Schauer, Origin of molecular conformational stability: Perspectives from molecular orbital interactions and density functional reactivity theory, J. Chem. Phys. 142 (2015) 054107 https://doi.org/10.1063/1.4907365.
[71] J. Aihara, Reduced HOMO−LUMO Gap as an Index of Kinetic Stability for Polycyclic Aromatic Hydrocarbons, J. Phys. Chem. A. 103 (1999) 7487–7495 https://doi.org/10.1021/jp990092i.